5-2020

Effect of Alkali-Silica Reaction on Confined Reinforced Concrete

Nolan Wesley Hayes
University of Tennessee, nhayes3@vols.utk.edu

To the Graduate Council:

I am submitting herewith a dissertation written by Nolan Wesley Hayes entitled "Effect of Alkali-Silica Reaction on Confined Reinforced Concrete." I have examined the final electronic copy of this dissertation for form and content and recommend that it be accepted in partial fulfillment of the requirements for the degree of Doctor of Philosophy, with a major in Civil Engineering.

Z. John Ma, Major Professor

We have read this dissertation and recommend its acceptance:

Richard M. Bennett, Timothy Truster, Yann Le Pape

Accepted for the Council:

Dixie L. Thompson

Vice Provost and Dean of the Graduate School

(Original signatures are on file with official student records.)

Effect of Alkali-Silica Reaction on Confined Reinforced Concrete

A Dissertation Presented for the

Doctor of Philosophy

Degree

The University of Tennessee, Knoxville

Nolan Wesley Hayes

May 2020

To God Be the Glory

To my wife

and

To my parents

Acknowledgments

This research was made possible by the support of the US Department of Energy's Office of Nuclear Energy, Light Water Reactor Sustainability Program, under contract number DE-AC05-00OR22725.

I would like to thank my advisor, Dr. John Ma, who instilled in me a passion for the progression of knowledge. His expertise, understanding, guidance, and support have encouraged me to achieve more than I could have imagined. I am grateful to Dr. Yann Le Pape whose passion for research was a major driver in developing my own devotion for research. His mentoring and deep understanding of material related to my topic has immensely helped in my own studies. I am thankful to Dr. Farid Benboudjema who hosted my stay in France at the École normale supériere Paris-Saclay. Through his patience in teaching and mentoring, the inclusion of the concrete models presented in this research was possible. I am also thankful to Dr. Timothy Truster and Dr. Richard Bennett for serving on my committee.

I would also like to thank Dr. Sihem Le Pape whose assistance and support in the management of the research project established my work for success. I am grateful to Dr. Alain Giorla whose mentoring and guidance strengthened my analysis of the research data. I am thankful to Larry Roberts and Andy Baker for all their assistance in helping with all the aspects of performing lab-work in structural engineering research. Because of their attention to safety, I still have all my fingers and toes. I am also grateful to Nancy Roberts who through her unending list of contacts was able to help in the procurement of many materials necessary for the research.

Abstract

Alkali-silica reaction (ASR), which was recently discovered in nuclear power plant structures commonly without shear reinforcement, has previously been shown to induce anisotropic expansion in confined concrete. A large-scale testing program on alkali silica reaction (ASR)-affected concrete structural members without shear reinforcement representative of structural members found in nuclear power plants is presented. Three large concrete specimens with ASR and varying levels of confinement were monitored in accelerated testing conditions. Strong anisotropic expansion and oriented ASR-induced cracking resulting from the confinement effect caused by the reinforcement layout and additional structural boundary conditions were observed. Surface cracking is not indicative of internal ASR-induced damage/expansion.

The fracture properties (strength, stiffness, and specific fracture energy) of ASR-induced anisotropically-damaged concrete specimens were quantified by varying both the damage level and relative direction of the ASR-induced cracking orientation against the loading direction corresponding to the fracture propagation. The effect of different orientations (0, 45, and 90 degrees relative to the notch of the specimen) of expected ASR-induced cracks on the fracture properties was investigated using a wedge-splitting test (WST). Specimens without ASR expansion generally showed the highest fracture properties; however, the specific fracture energy was highest for ASR-affected specimens in which the expected orientation of ASR-induced cracks was perpendicular to the WST specimen notch. Specimens in which the ASR-induced cracks were parallel to the notch exhibited the lowest strength and fracture energy.

A new model was developed for predicting the expansion of concrete structures affected by alkali-silica reaction. The model includes a novel combination of existing models as a

alkali-silica reaction advancement model, a novel casting direction anisotropic expansion model, a novel stress-dependent anisotropic expansion model, and a novel material property evolution model dependent on the degree of ASR expansion. The calibrated model was validated in predicting the ASR-expansion of the large-scale reinforced concrete specimens with confinement of this study. The results of this study highlight the need for additional research to be conducted to investigate a possible size effect for very-large concrete specimens affected by ASR and the need for additional research on multi-axially loaded concrete specimens with ASR.

Table of Contents

List of Tables

List of Figures

Chapter 1

Introduction

1.1 Background

1.1.1 Alkali-Silica Reaction

Alkali-aggregate reaction (AAR) is a widespread concrete deterioration issue. Alkali-silica reaction (ASR) is the most common type of AAR. ASR was first identified by Stanton (1940). The reaction has been extensively studied since. ASR is a chemical reaction between alkali hydroxides in the concrete pore solution and reactive silica in certain types of aggregates. ASR requires three components: (1) a sufficient concentration of alkali hydroxides, (2) a sufficient quantity of reactive silica, and (3) a sufficient supply of moisture (Thomas et al., 2011). The reaction produces a gel that imbibes water leading to expansion and creating internal stresses in the concrete. The expansion of the gel initiates cracking originating from the reactive silica in aggregate particles. As the expansion of the gel continues, the cracking propagates into the cement matrix leading to volumetric expansion of the concrete. The expansion generates stresses due to the expansive pressure of the gel. The cracking causes degradation of material properties.

1.1.2 ASR in Nuclear Power Plants

ASR was discovered in concrete structures at a nuclear power plant (NPP) in the United States (United States Nuclear Regulatory Commission, 2011). ASR was also discovered in

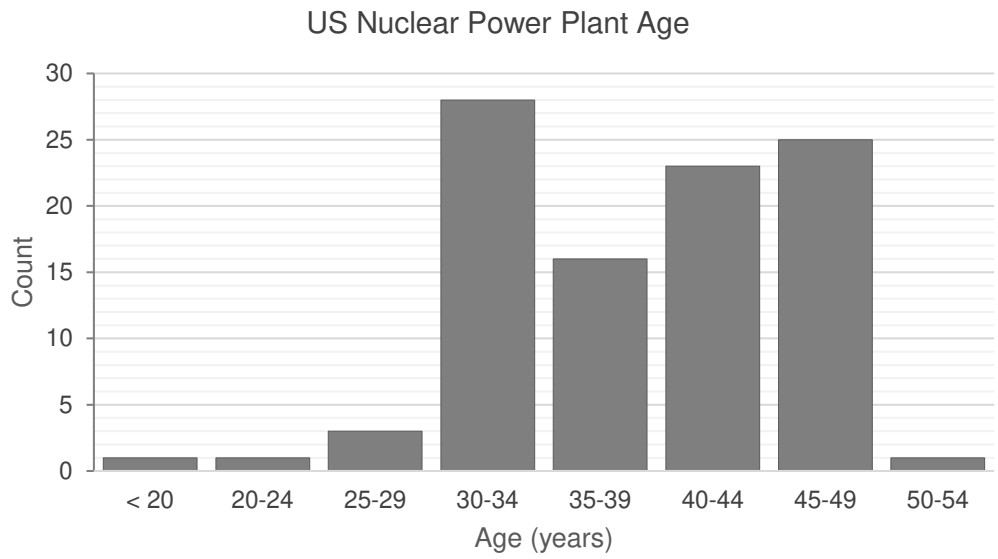

Figure 1.1: Age of operating reactors (United States Nuclear Regulatory Commission, 2018)

other NPPs in Canada and Japan (Takatura et al., 2005; Shimizu et al., 2005; Tcherner and Aziz, 2009). NPPs differ from other infrastructure in that the critical concrete structures, such as the containment building, often have larger than normal thicknesses. Because most in-service NPPs were designed some time ago, design codes did not require steel reinforcement oriented along the thickness to resist shear forces. The shear force applied to the structure is resisted by concrete alone. This unique structural detail presents a case in which ASR has not been previously studied. The presence of steel reinforcement in the directions of the plane of the wall and the lack of shear reinforcement present a state in which ASR expansion may develop anisotropically. Additionally, because the containment structure is a continuous wall, the in-plane directions of the wall are also confined by surrounding concrete. The combined effect of differing reinforcement ratios and levels of confinement in each primary direction of a structure on the development of ASR has not been researched. It is important to study the effects that ASR may have on NPP concrete structures.

In the United States, the Nuclear Regulatory Commission (NRC) issues licenses for operation of nuclear reactors. The first issuance of operating license is valid for 40 years, after which, the owner of the reactor may apply to renew the operating license for another 20 years. The NRC has no available data to perform license renewal decisions for NPPs with ASR. Figure 1.1 shows the age of currently operating reactors. Many reactors are

approaching an operating age of 40 years. Additional research on the effects of ASR on NPP concrete structures is necessary for the NRC to make informed decisions regarding the renewal of operating licenses of reactors with concrete structures affected by ASR.

1.2 State-of-the-Art

1.2.1 Reaction

ASR is a slow reaction with visible signs of effects often not evident for several years after construction. The reaction depends upon three reactants: alkali-hydroxides, reactive silica, and moisture (Thomas et al., 2011). The majority of the alkali-content in concrete comes from the cement. However, external sources of alkalis are possible from de-icing salts and the natural environment. For existing concrete structures, the amount of alkali content from cement alone is generally enough to start the reaction. The water of the pore solution is generally a sufficient amount to cause significant expansion unless the concrete is exceptionally dry (Blight and Alexander, 2011).

The reaction is dependent on temperature (Ulm et al., 2000). Higher temperatures accelerate the dissolution of silica in aggregates. The earlier dissolution of aggregates allows the reaction to initiate sooner. Higher temperatures also increase the rate at which reaction products are produced. A higher concentration of reaction products (gel) leads to accelerated expansion due to a higher degree of swelling if water is in sufficient supply.

The reaction is also dependent on internal relative humidity of the concrete. Considerable expansions only occur in concrete with an internal relative humidity exceeding 75% (The Institution of Structural Engineers, 1992). The water-to-cement ratio is a key factor that influences the free-water within the concrete pores (Fournier and Bérubé, 2000). Increased free water within the pores increases the rate of reaction and corresponding expansion.

1.2.2 Expansion

Expansion due to ASR has been shown to be dependent on the stress-state of the concrete (Larive, 1997; Multon and Toutlemonde, 2006). Expansion was observed to be highest in the

direction least stressed. Confinement of concrete by passive restraint (surrounding steel) was shown to reduce expansion in the directions of confinement and increase expansion in the unconfined direction. Additionally, research has determined that steel reinforcement induces a restraining effect and reduces expansion in the direction of reinforcement with higher reinforcement ratios causing the most significant reduction (Inoue et al., 1989; Koyangi et al., 1992; Jones and Clark, 1996).

A casting direction anisotropy has been observed for concrete affected by ASR (Jones and Clark, 1996; Larive, 1997; Smaoui et al., 2004). The expansion in the direction parallel to the line of action of gravity is generally largest among expansions in all directions. Smaoui et al. (2004), using observations noted by Larive (1997), attributed this anisotropy to the preferred alignment of aggregate particles perpendicular to gravity. The alignment of aggregate particles generates a location at which bleeding water can be trapped and form a porous, weaker paste/aggregate interface. The alignment may also trap concentrated areas of reactive particles producing a concentration of gel in the plane perpendicular to gravity. Flat or elongated aggregate particles most commonly aligned along the casting plane causing higher degrees of casting direction anisotropy.

A size effect has been observed for concrete affected by ASR (Lindgård et al., 2013). Smaller specimens (higher surface-to-volume ratio) are more susceptible to alkali-leaching when in contact with water (both direct contact and condensate). The alkali-leaching removes available alkalis from the pore solution of the concrete which reduces the observed maximum value of expansion. No studies have investigated a size effect for very large concrete structures.

1.2.3 Material Property Deterioration

ASR expansion has been shown to reduce material properties of concrete (Swamy and Al-Asali, 1988a; Giannini and Folliard, 2012). Compressive strength and tensile strength have been shown to decrease at high values of ASR-expansion (Esposito et al., 2016). Elastic modulus is the most affected property with ASR-expansion typically causing a reduction of 50% or more at large expansions. Two competing mechanisms, the ongoing hydration of cement and ASR damage, have been shown to cause differences in experimental testing

during the early stage of expansion and after expansion is exhausted. In some cases, the increase in compressive strength due to cement hydration seems to overcome the loss of strength due to ASR (Multon et al., 2005; Na et al., 2016).

The slight recovery of the mechanical properties at a late stage of ASR expansion was reported in the literature (Swamy and Al-Asali, 1988b; Ahmed et al., 2003; Gautam, 2016). This recovery can be attributed to the continuation of cement hydration process (Swamy and Al-Asali, 1988b), or to the transformation of ASR gel in cracks into a more calcium-rich gel (eventually resembling C-S-H gel) which can contribute to the concrete regaining strength and stiffness (Gautam, 2016).

1.2.4 Modeling of ASR

ASR in critical concrete structures such as nuclear power plants, bridges, dams has been addressed as a significant issue. Many researchers have developed models to simulate the expansion of concrete structures with ASR and determine the residual behavior of such affected structures (Léger et al., 1996; Capra and Sellier, 2003; Saouma and Perotti, 2006; Grimal et al., 2010). Some models account for a decrease in elastic modulus and tensile strength due to ASR damage. Most models assume that compressive strength are not affected by ASR-expansion. Most models consider the influence of stress and confinement on ASR expansion. However, the coupling of stress and expansion is different between each model. The calibration of models is difficult due to the lack of experimental data on the relationship between multi-axial stresses and ASR-expansion. However, recent research studies have generated experimental data on which stress-coupled-expansion models can be better calibrated (Gautam, 2016; Gautam et al., 2017).

1.3 Research Scope and Objectives

The behavior of large-scale reinforced concrete undergoing ASR under confinement was investigated. Expansion, cracking, and material property degradation were investigated using destructive testing and tools to measure expansion. Models were developed and validated for use in predicting the expansion of large-scale reinforced concrete specimens

undergoing ASR under confinement. The results of this study can be used to assess reinforced concrete structures with ASR.

The objectives of this study were to monitor, characterize, and model confined large-scale reinforced concrete affected by ASR. To achieve these objectives, the following sub-objectives were prioritized:

1. Monitor the expansion and cracking of a large-scale reinforced concrete mockup of a nuclear power plant containement structure affected by ASR

2. Characterize the effect of anisotropic ASR-expansion on the material properties of confined concrete

3. Develop a model to predict the expansion of reinforced concrete affected by ASR under confinement

1.4 Dissertation Organization

Chapter 1 provides an introduction to the thesis content and structure. Chapter 2 describes the experimental testing program to determine the effects of ASR on a typical nuclear power plant structure and reports results. Chapter 3 focuses on the testing program to determine the effect of anisotropic ASR-expansion on the fracture properties of concrete. Chapter 4 explains the models created and validated by simulating the experiment in Chapter 1. Chapter 5 concludes the dissertation noting the novel scientific contributions and suggests future potential areas of research to further advance knowledge.

The chapters of this dissertation are organized such that each chapter forms a single manuscript that has been or will be submitted to peer-reviewed journals. The list of manuscripts is shown below:

1. Hayes, N. W., Gui, Q., Abd-Elssamd, A., Le Pape, Y., Giorla, A. B., Le Pape, S., Giannini,E. R., and Ma, Z. J. (2018). Monitoring alkali-silica reaction significance in nuclear concrete structural members. *Journal of Advanced Concrete Technology*, 16(4):179190

2. Hayes, N. W., Giorla, A. B., Trent, W., Cong, D., Le Pape, Y., and Ma, Z. J. (2020). Effect of alkali-silica reaction on the fracture properties of confined concrete. *Construction and Building Materials*, 238, 117641.

3. Hayes, N. W., Benboudjema, F., Le Pape, Y., and Ma, Z. J. (2020). Modeling alkali-silica reaction expansion in large-scale reinforced concrete specimens with confinement. (To be submitted).

Chapter 2

Monitoring of Alkali-Silica Reaction in Confined Reinforced Concrete

2.1 Introduction and Research Significance

Alkali-silica reaction (ASR) is a widely recognized degradation mechanism affecting numerous transportation and hydroelectric concrete infrastructures. However, recent disclosures in the nuclear industry in Canada, in Japan, and in the U.S. (Takatura et al., 2005; Shimizu et al., 2005; Tcherner and Aziz, 2009; U.S. Nuclear Regulatory Commission, 2011; NextEra Energy Seabrook, 2013) raised concern about the structural significance of ASR on concrete nuclear structures in light water reators (LWR), such as the containment building, the biological shield or the spent fuel handling building. Demand for a better understanding of the mechanisms and effects of ASR in nuclear power plant structures has increased. While lessons-learned from the available operating experience and aging management programs can be valuably shared between the different industries confronted with this distress mechanism, typical reinforced concrete structural members in LWR present specific challenges resulting from their geometry (thickness ranging from approximately 0.60 m to 1.5 m) and their reinforcement ratios and layout. In particular, shear reinforcement (i.e., transverse through thickness) is not required by ACI 318 (2014) and ACI 349 (2013) codes for structural strength due to the significant depth of concrete contributing to the shear resistance of the structural element. The absence of shear reinforcement in structural members subjected

to ASR does not result unambiguously in either a gain or a reduction of shear capacity (Bach et al., 1993; den Uijl and Kaptijn, 2003; Nakamura et al., 2008; Saouma et al., 2016). Several additional factors seem to contribute to the modification of the shear capacity: in particular, the reinforcement ratio, the ASR-induced expansion, and the structural boundary conditions (Saouma et al., 2016). ASR-induced expansion occurs primarily in the unloaded direction (Larive, 1997), i.e., applied mechanical compression stresses result in the volumetric expansion transfer or redistribution in the direction of lower loading (Multon and Toutlemonde, 2006). Applied mechanical stresses are caused not only by in-service external loading, but can also be induced by retrained ASR-expansion due to the presence of reinforcement (Multon et al., 2005), and unfavorable rigid structural boundary conditions (Saouma et al., 2016). Hence, it can be hypothesized that two competing mechanisms notably influence the residual shear capacity: (1) The ASR-induced self-prestressing in the direction of the reinforcement, and (2) the formation of anisotropic ASR-induced damage in the bulk of the reinforced concrete members.

Acknowledging the lack of experimental data on ASR-affected reinforced concrete structural members without shear reinforcement and subjected to different structural boundary conditions, and their relevance for the nuclear industry, a novel set of highly-instrumented large-scale experiments were designed and fabricated. This work includes two phases: (1) The monitoring of expansions and damage development in all directions inside the massive concrete and on the surface, and (2) The destructive testing of the specimens to assess the post-ASR residual shear capacity. This article specifically reports on the first phase of this program.

2.2 Materials and Methods

2.2.1 Specimen Design

The structural specimen detail was designed to closely resemble a typical nuclear power plant containment structure, that is, a thick-walled concrete structure with no shear reinforcement. Specimens were designed with a thickness of 1.0 m (3.28 ft) and reinforced only in the plane

of the wall with two elevations of intersecting large steel reinforcement leaving the thickness of the wall entirely unreinforced.

Three concrete specimens were conceptualized and constructed. The first specimen, referred to as CASR, was confined in a relatively rigid steel frame to simulate the additional confinement by surrounding concrete that would be present in a NPP containment structure. This steel frame confines against expansion in the plane of the wall, forcing a preferred direction for expansion as the thickness direction of the specimen.

The second specimen, referred to as UASR, with identical mix design and steel reinforcement detail was designed and constructed with no surrounding steel frame. Thus, this specimen is unrestrained by exterior boundary conditions but still partially restrained against expansion in the plane of the wall by the steel reinforcing bars.

The third specimen, referred to as CTRL, with identical steel reinforcement was designed and constructed with two changes to the mixture design to minimize the potential for expansion from ASR. Sodium hydroxide (NaOH), used to promote the development of ASR in the CASR and UASR specimens, was not used in the mix design for the CTRL specimen. Instead, lithium nitrate ($LiNO_3$) was added to mitigate against the alkalis contributed by the cement. No ASR expansion was observed in this specimen.

For the sake of practicality, the specimens were cast horizontally. Hence, the actual through-wall thickness corresponds to the vertical direction (Z).

2.2.2 Dimensions and Reinforcing Details

Specimen dimensions were selected to best represent the scale of an NPP containment structure. The through-thickness dimension (Z-direction) is 1.0 m (3.3 ft). The dimensions within the plane of the wall were selected accordingly at 3.5m (11.5 ft) and 3.0m (9.8 ft) for the X-direction and Y-direction respectively. These dimensions are shown in Figure 2.1.

The reinforcement layout for the specimens was also selected to most closely resemble that of a NPP structure. The reinforcement layout consists of US #11 Gr. 60 reinforcing steel bars with a nominal diameter of 35.81 mm (1.41 in) spaced at 25.4 cm (10 in) on-center resulting in two elevations of reinforcing bars embedded in the concrete specimens with 7.62 cm (3 in) of concrete cover. The reinforcement layout results in reinforcement

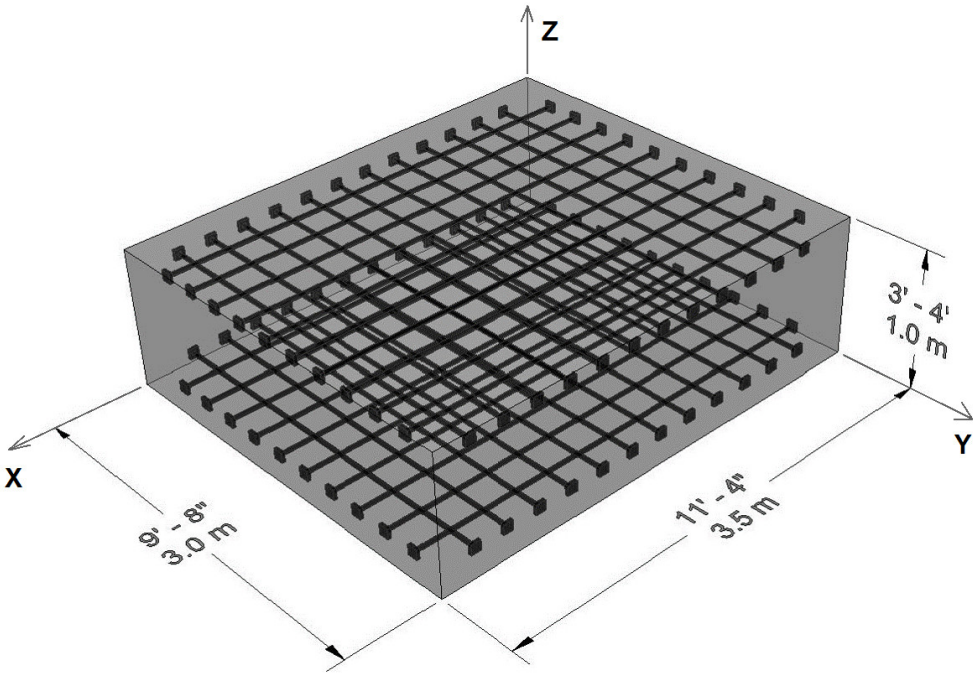

Figure 2.1: Dimensions and coordinate axes of concrete specimens (Hayes et al., 2018)

Table 2.1: Reinforcement ratio of specimens in each direction (Hayes et al., 2018).

Direction	Reinf. ratio
X-direction	0.67%
Y-direction	0.68%
Z-direction	0.00%

Note: Reinforcement ratio reported is total longitudinal reinforcement area divided by gross cross-sectional concrete area.

ratios for each direction are noted in Table 2.1. Additionally, the reinforcing steel bars were installed with square heads (10.16 cm × 10.16 cm × 2.54 cm) (4 in × 4 in × 1 in) made of steel plate to achieve full development length within a relatively short distance inside the specimen. Each specimen was cast-in-place, elevated 76 cm (30 in) above the floor supported by four steel columns capped with 45.7 cm (18 in) square steel plates.

2.2.3 Steel Confinement Frame

In order to simulate the range of structural boundary conditions present in a large structure such as a NPP containment building, two cases are considered: (1) a reinforced concrete specimen unconstrained laterally, and (2) a similar specimen encased in a rigid steel frame, restraining lateral deformation in the plane of the reinforcement and allowing unrestrained

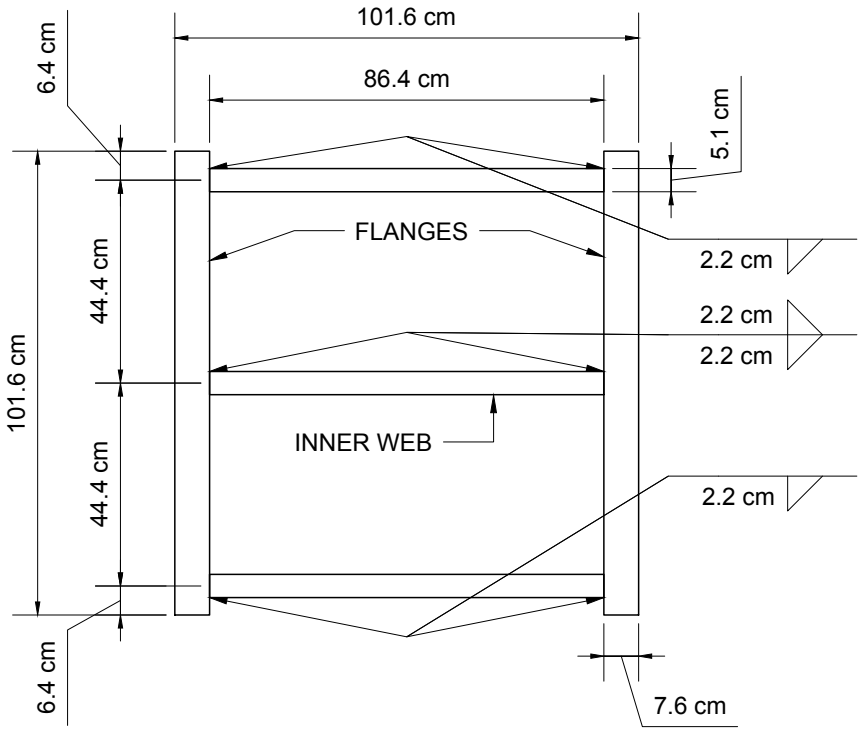

Figure 2.2: Cross-section of steel confinement frame (Hayes et al., 2018).

expansion through the specimen thickness. In order to reduce frictional effects between the steel frame and the concrete specimen, a single 1.5 mm-thick layer of high density polyethylene (HDPE) was placed at the concrete-steel interface.

To provide sufficient rigidity, the confinement frame was designed for maximum stiffness. A steel plate girder cross-section was designed consisting of two 76 mm (3 in) flanges and three 51 mm (2 in) webs as shown in Figure 2.2. Because of limited lifting capabilities, the frame was designed as four sections joined by slip-critical bolted connections, each consisting of twelve splice plates and 144 bolts. An illustration of the connected elements of the steel confinement frame is shown in Figure 2.3.

The cross-section and connections were designed for a maximum pressure of 8 MPa (1160 psi) at the steel frame-concrete interface and a corresponding maximum deflection of 2.5 mm (3/32 in).

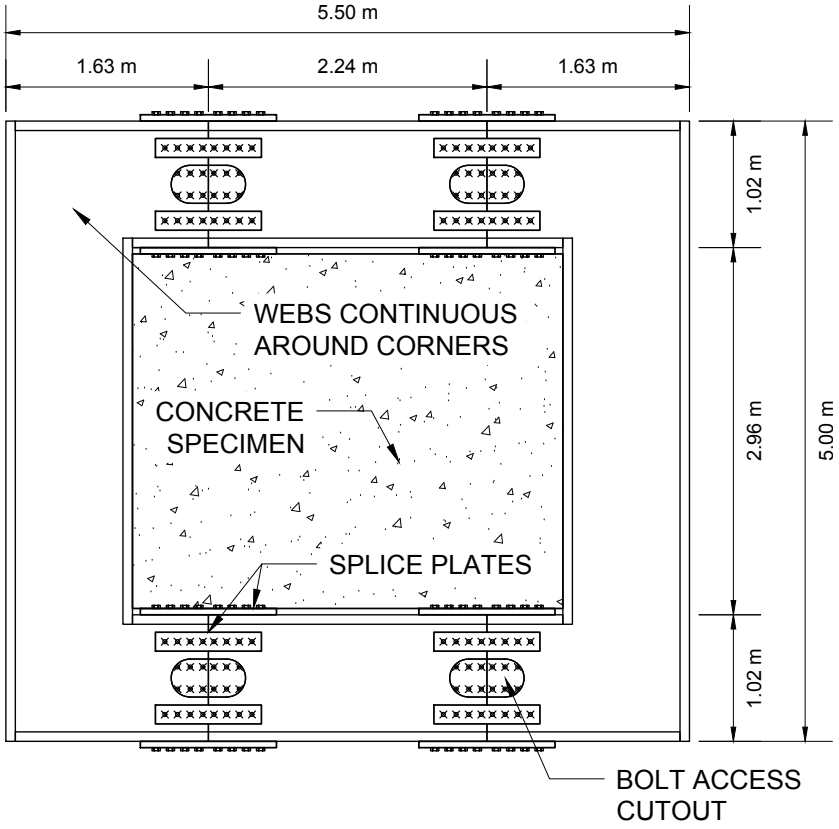

Figure 2.3: Plan view of assembled steel confinement frame (Hayes et al., 2018).

2.2.4 Concrete Formulation

For this study, two mixtures were developed: (1) a reactive mixture capable of rapid free expansion at a rate of approximately 0.15% linear expansion per year, and (2) a mitigated control mixture containing lithium nitrate which inhibits the expansive properties of the ASR gel. Both mixtures contain the same coarse aggregate, fine aggregate, cement, water-cement ratio, and admixtures. The only differences in the two mixtures were the use of sodium hydroxide (NaOH) solution in the reactive mixture and lithium nitrate ($LiNO_3$) solution in the control mixture.

The mixture proportions are shown in Table 2.2. The coarse aggregate used was a highly-reactive greenschist from North Carolina. The fine aggregate used was a non-reactive manufactured sand from the Knoxville, Tennessee area. The cement used was a low-alkali Type II Portland cement with an equivalent alkali content of 0.41% Na_2O_{eq}. A 50% w/w

Table 2.2: Design proportions of concrete mixtures (Hayes et al., 2018)

Materials	Quantity, ($\mathrm{kg\,m^{-3}}$) ($\mathrm{lb\,yd^{-3}}$)	
	Reactive	Control
Coarse Aggregate	1180 (1989)	1180 (1989)
Fine Aggregate	728 (1227)	728 (1227)
Cement	350 (590)	350 (590)
Water*	175 (295)	175 (295)
50% NaOH solution	9.8 (17)	-
30% $LiNO_3$ solution	-	11.9 (20.0)
Water reducing admixture	2.0 oz/cwt	2.0 oz/cwt
Stabilizer admixture	2.0 oz/cwt	2.0 oz/cwt

Note: Aggregate quantities are given for oven-dry materials. Water quantities assume aggregates in saturated-surface dry (SSD) condition. (*) indicates that 70% of the mass of mixing water was replaced by ice, and the actual w/c ranged between 0.46 to 0.52.

sodium hydroxide (NaOH) solution was added to the reactive specimens to increase the alkali content to 5.25 $\mathrm{kg\,m^{-3}}$ (1.50% Na_2O_{eq} by mass of cement). A 30% w/w lithium nitrate ($LiNO_3$) solution admixture was added to the control specimen at 150% of the manufacturer's recommended dosage (sometimes referred to in the literature as the "standard dose" of a molar ratio of [Li]/[Na+K] = 0.74 in the mixture) to mitigate the potential for ASR (McCoy and Caldwell, 1951; Folliard et al., 2006; Thomas et al., 2007; Kim and Olek, 2012). In addition, a high-range water-reducing admixture (meets requirements for ASTM C494 Type F) and hydration stabilizer admixture (meets requirements for a ASTM C494 Type D retarder) were added to maintain a slump value between 15 to 20 cm (6 to 8 in.) and offset the effects of warm ambient temperatures that would otherwise accelerate setting of the concrete during placement. The design water-to-cement ratio, w/c, was 0.50 for the both mixtures.

2.2.5 Casting and Curing Conditions

Casting took place on July 23rd, 2016. In an attempt to mitigate potential damage sources other than ASR (e.g. thermal cracking), the formworks were insulated prior to the concrete placement by placing rigid foam sheathing insulation with an R-value of 3 around the sides. Additional sheathing was installed on top of the specimens, shortly after initial set and final finishing of the top surface. The insulation was placed with edges overlapping and secured in place with tape and plastic wrap.

To avoid any additional detrimental DEF-induced expansion, the temperature within the concrete specimens during early-age curing was kept below 70 °C by substituting 70% of the mixing water with ice. The use of ice also permitted placement temperatures of 20 °C or less, which complemented the hydration stabilizing admixture in terms of extending the time to set, ensuring sufficient time to place and finish the concrete in the laboratory.

All formworks were removed on August 4, 2016. After final finishing and setting of the concrete, each exposed specimen surface was sprayed with curing compound and then covered with a layer of wet burlap and plastic sheeting to minimize any moisture loss and mitigate early-drying-induced cracking. The burlap was periodically moistened until full operation of the environmental chamber.

The specimens were stored in an environmental chamber designed for temperature and humidity control of 38 ± 1 °C (100 ± 2°F) and $95\% \pm 5\%$ relative humidity (RH). In order to maintain the temperature and RH during operation, a heating system consisting of both heating evaporators and heating units accommodated by air circulators was designed.

The environmental chamber was delivered as panels consisting of embossed steel filled with foam insulation. Each panel has a set of locks to secure adjacent panels to each other. The floor connection is sealed by a vinyl sealer placed underneath the wall panels to the concrete floor of the high bay laboratory. To allow the construction of the three concrete specimens, the environmental chamber was built around the specimens a few weeks after casting.

A full power up of the heating system was completed August 17, 2016 to test the operation of the heating and misting system as well as the lighting system. After confirmation of the systems working order, the system was powered down to finalize all connections and prepare the chamber for full-time operation. All concrete specimens were uncovered at this time. The completed chamber measures approximately 16.2 m (53 ft) long, 7.3 m (24 ft) wide, and 3.7 m (12 ft) high. This area allows for all three reinforced concrete specimens and all concrete cylinders for material testing to be contained within the same environment.

The chamber was initialized for full operation on August 19, 2016 (concrete age of 26 days). The chamber was operated uninterrupted, except for periodic inspections, at the specified environmental conditions. The relatively high temperature and moisture content

constitute a working safety hazard. Hence, the chamber is periodically shutdown for inspection on a average frequency of two days per month. During shutdowns, the average temperature and RH are about 25°C (≈77°F) and 60% (transient of about 4 hours). After the shutdown period, the chamber is restarted; the temperature and humidity return to the original set points within 6 hours. The time period of chamber shutdowns is small (less than 5% of overall monitoring time). The change in temperature during chamber shutdowns is accompanied by thermal strains of the concrete; however, because continuity is observed in the measured strains before and after temperature changes, the chamber shutdowns have no effect on concrete confinement provided by the steel frame.

2.2.6 Material Testing

Three groups of companion cylinders (150 cylinders total) made of the same concrete batches of the CASR, UASR, and CTRL specimens were prepared to measure the evolution of the elastic modulus, compressive strength and splitting tensile strength with the ASR.

While the UASR and CTRL cylinder specimens were removed from molds 48 hours after casting, each CASR cylinder specimen was kept in a relatively rigid cylindrical steel mold with a wall thickness of 6.4 mm (1/4 in) until the time of testing. The cylindrical steel molds were used to promote ASR-induced expansion primarily in the vertical direction, i.e. parallel to the casting direction, while the unrestrained cylinders were allowed to expand in all directions.

All cylinders were stored in the environmental chamber containing the large specimens. Mechanical testing was performed at 7, 28 days, and then at 3, 5, 6, 9, and 12 months. The elastic modulus, compressive strength and splitting tensile strength were measured using ASTM C469, ASTM C39 and ASTM C496, respectively.

2.3 Monitoring and Sensing Techniques

The concrete specimens were heavily instrumented to monitor local strain and temperature within the bulk of the specimens as well as structural deformations as the ASR progressed. In total, three different types of sensors are being utilized, as illustrated in Table 2.3.

Table 2.3: Types and quantities of sensors for all specimens (Hayes et al., 2018).

Sensor	Quantity
Temperature:	
Thermocouple	12
Deformation/Strain:	
Strain transducer	64
Long-gauge FO extensometer	12

2.3.1 Embedded Strain Sensors

A total of 64 100 mm-gauge strain transducers (KM-100B from Tokyo Sokki Kenkyujo) were embedded in the concrete specimens. The transducers were installed using nylon cable ties to a support structure of 3 mm (1/8 in)-diameter smooth steel bars installed between the two layers of steel reinforcement prior to concrete placement. These sensors have shown remarkable durability in previous research including ASR studies (Herrmann et al., 2008; Bracci et al., 2012).

These strain transducers sense the change in distance between two circular disks mounted on the ends of a tube which is wrapped with a protective coating and tape. The strain transducers were arranged within the specimens as shown in Figure 2.4. The placement of the strain transducers was designed to (1) measure strains in all directions, (2) evaluate strains spatial variability by increasing the density of sensors in a single quadrant, and (3) limit possible interactions with nondestructive evaluation (NDE) based on acoustic wave propagation techniques by reducing the density of sensors in the opposite quadrant. With strain transducers oriented to measure strain in both the restrained (X and Y) and unrestrained (Z) directions for the confined specimen, the effect of confinement on the orientation, frequency, and degree of microcracking within the bulk due to ASR can be evaluated.

Because the strain transducer layout being the same for both the confined and unconfined ASR specimens, a thorough comparison of the data from strain transducers for both the restrained concrete specimen and unrestrained concrete specimen can be conducted in order to characterize the effects of confinement on the development of ASR.

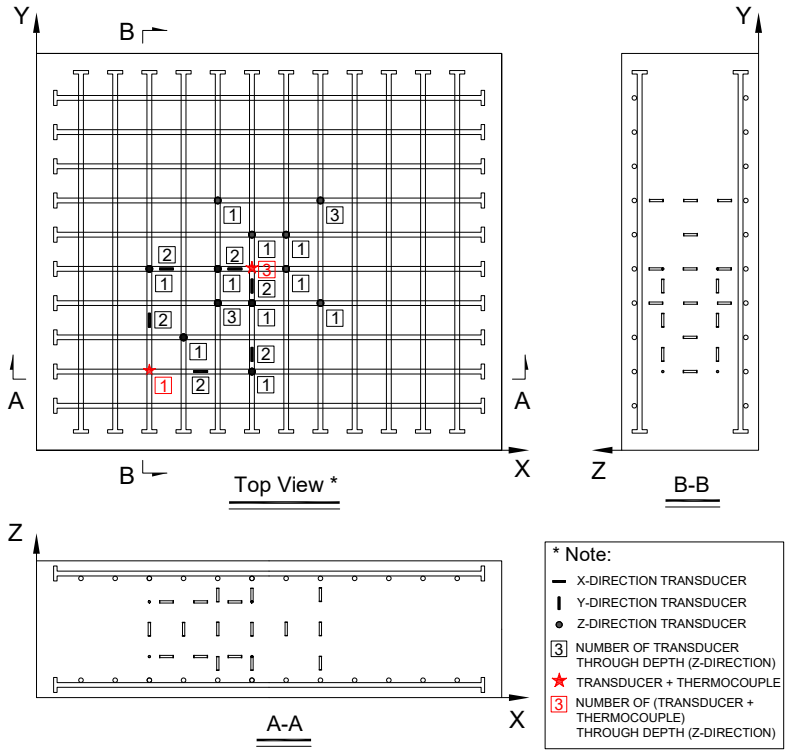

Figure 2.4: Layout for embedded strain transducers with specimen coordinate axes and specimen dimensions as described in Figure 2.1 (Hayes et al., 2018).

2.3.2 Long-Gauge Fiber-Optic Deformation Sensors

In addition to the local strain measurement, the overall structural expansion was also monitored for each principal direction. High precision (≈2 µm) and accuracy fiber optic (FO) extensometers (SOFO standard deformation sensor from SMARTEC/Roctest) (Inaudi, 1997; Glišić et al., 2013) were placed at the bottom surface of the specimens and inside the concrete, for the horizontal and vertical deformations measurements, respectively. The vertical FO extensometers, of 0.8 m-gauge length, measure the deformation between the top and bottom reinforcement layers and were attached to a 3 mm (1/8 in)-diameter steel smooth bar with nylon cable ties before concrete placement. The 1.5 m-gauge length horizontal FO extensometers were placed at the bottom surface of the specimens to allow access to the top surface for NDE. The sensors ends are supported by angle-plates, anchored 7.6 cm (3 in) deep in concrete, i.e., reaching the plane of reinforcement. The layout of extensometers is similar for both the restrained and unrestrained specimens as shown in Figure 2.5.

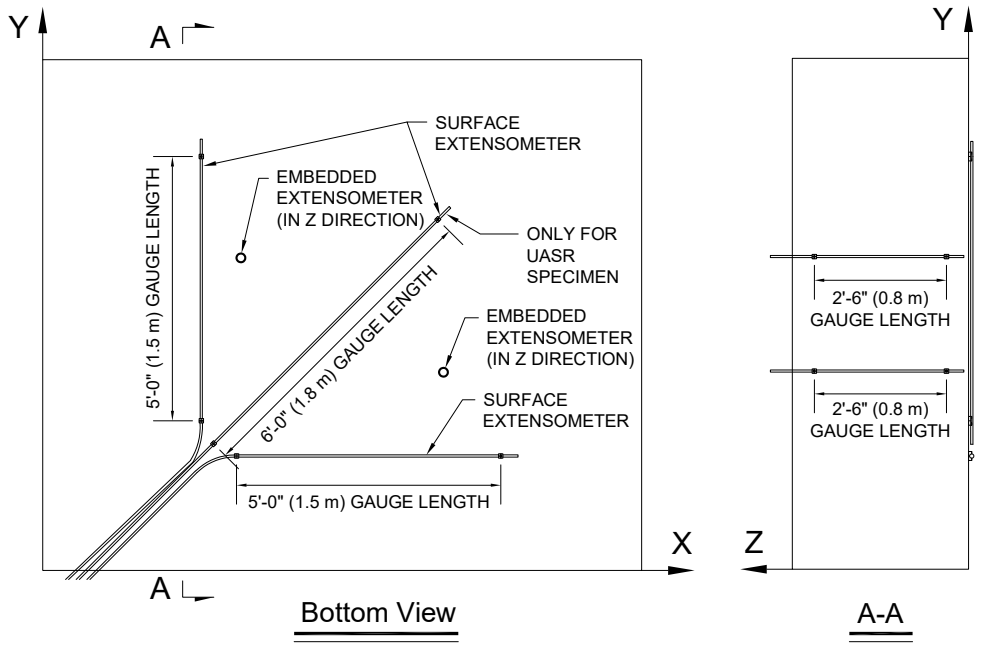

Figure 2.5: Layout for fiber optic extensometers with specimen coordinate axes and specimen dimensions as described in Figure 2.1 (Hayes et al., 2018).

2.4 Results

2.4.1 Early-Age

The internal temperature history of each specimen is shown in Figure 2.6. The reported temperature for each specimen is the recorded maximum of the four thermocouples embedded in that specimen. The CASR and UASR specimens were cast first in the early morning, and the CTRL specimen was cast after midday when the temperature within the lab was higher. For all specimens, the internal temperature remained below 70 C, which prevents the occurrence of DEF in the specimens. The temperature of each specimen slowly decreased from the peak of hydration heat stabilizing to room temperature of the laboratory over a period of nearly 20 days, thus minimizing the risk of thermal cracking.

2.4.2 Monitoring Data Correlation

Despite the differences in the two sensor systems (gauge length in particular), the expansion results between the two types of sensors are very agreeable. Figure 2.7 and Figure 2.8

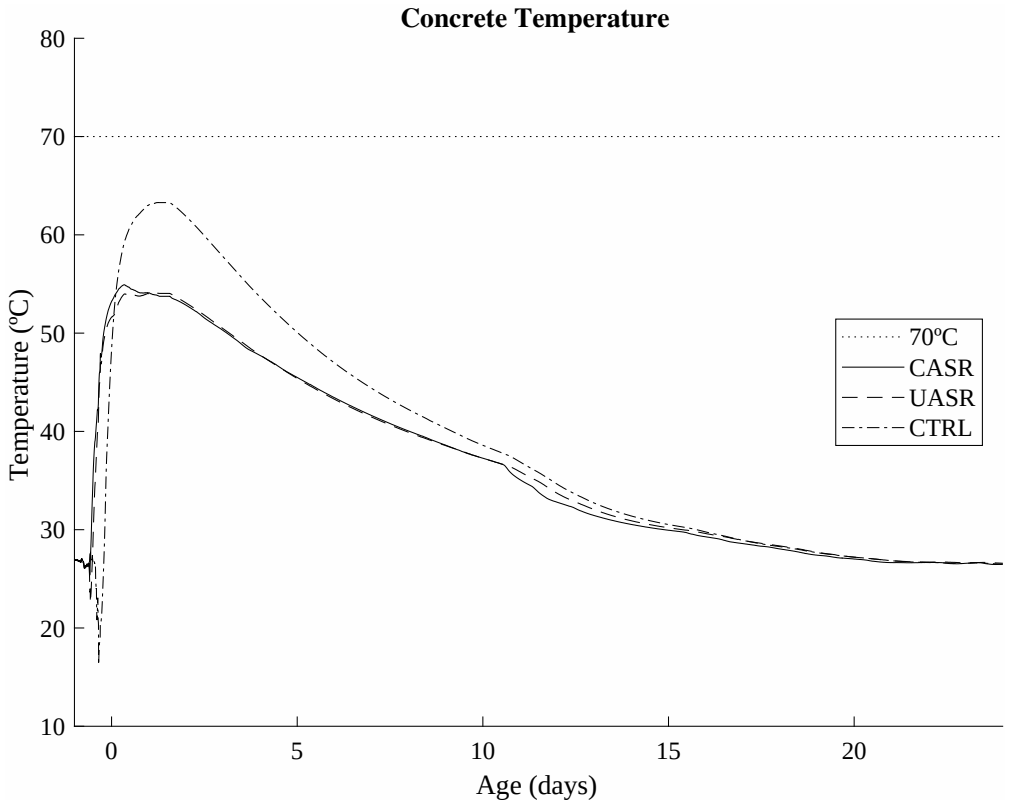

Figure 2.6: Early age concrete temperature (Hayes et al., 2018)

show the correlation between the local strain transducers and structural deformation sensors oriented to measure strain and deformation in the through-thickness (Z) direction for the CASR and UASR specimens. The mean of the transducer strain data is plotted against the structural deformation. The standard deviation (SD) lines indicate one standard deviation above and below the mean strain collected from the local strain sensors. The identity line designates perfect correlation. The linearity of the correlation plots indicates a good correlation between the short and long gauge lengths sensors in collecting expansion data. Hence, in the following sections, only the local strains collected by the embedded strain sensors will be reported and analyzed.

2.4.3 ASR-Induced Expansion

The expansion collected by the embedded strain sensors for each specimen in each direction is shown in Figure 2.9. For the sake of readability, only the average expansions are plotted. The CTRL specimen exhibits relatively low shrinkage and no trend toward expansion even

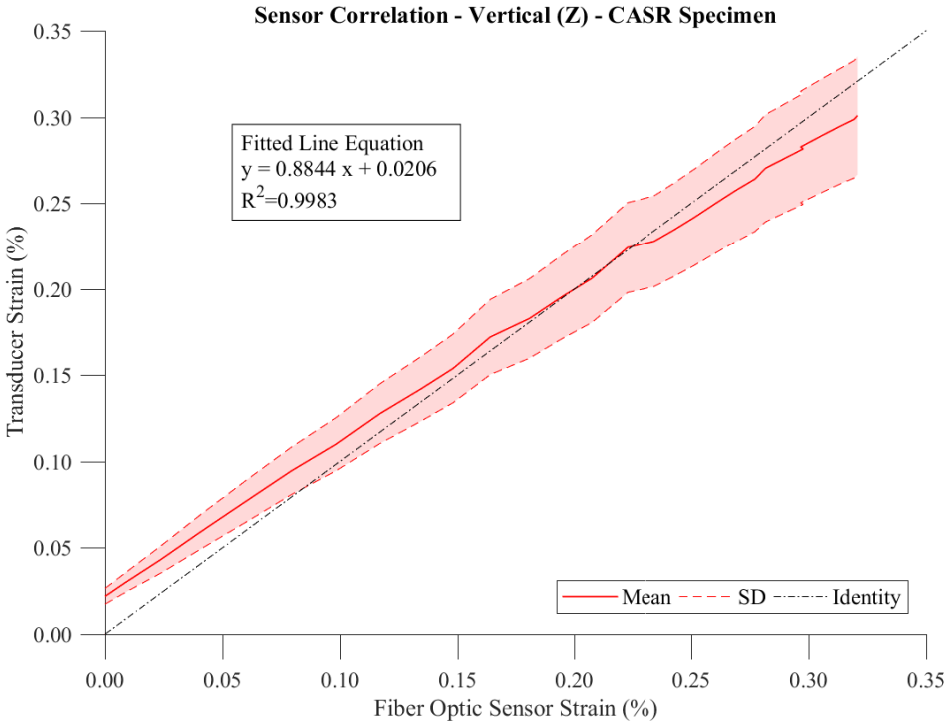

Figure 2.7: Correlation of Z-direction sensors of CASR specimen (Hayes et al., 2018).

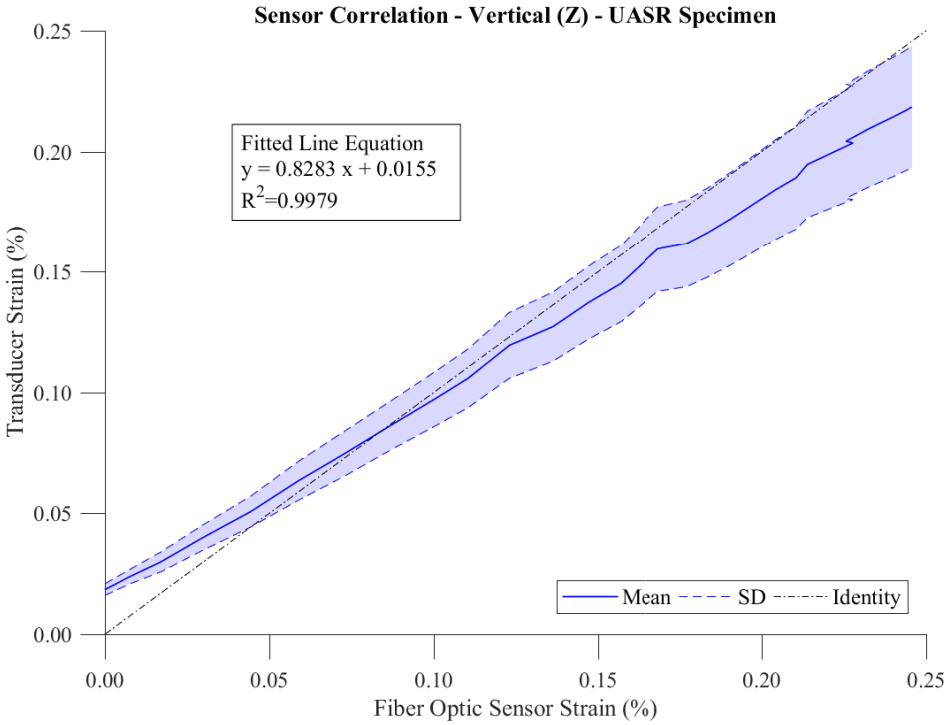

Figure 2.8: Correlation of Z-direction sensors of UASR specimen (Hayes et al., 2018).

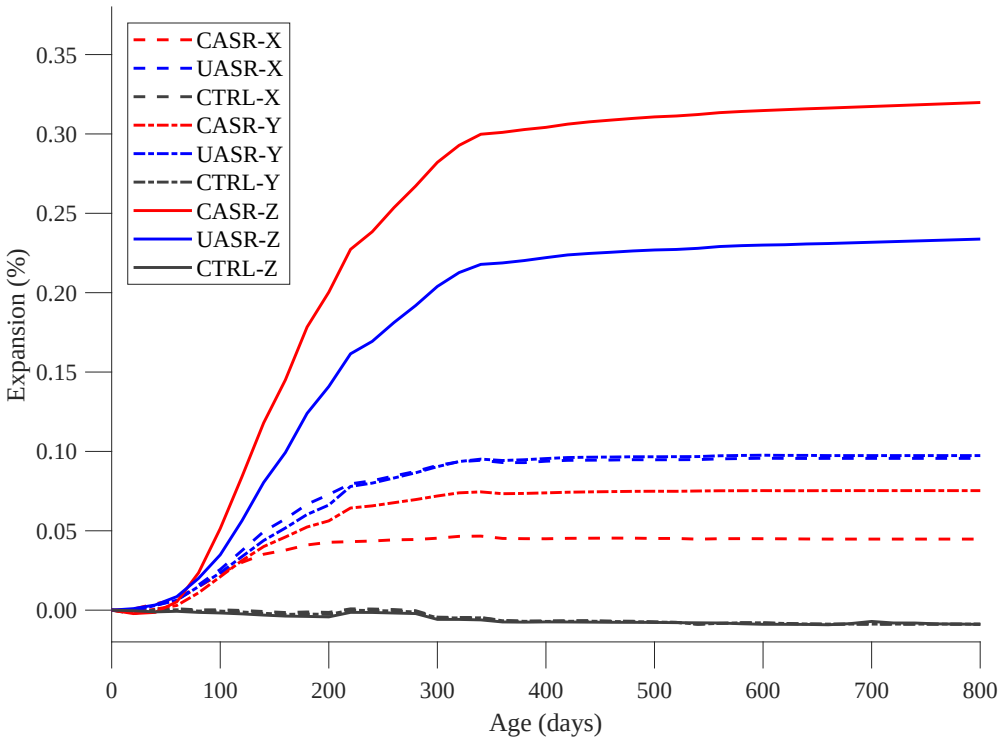

Figure 2.9: Expansion of each specimen in each direction

at a late stage of the experiment. The CASR specimen shows more vertical expansion and less lateral expansion than the UASR specimen. Because of the longer span of the steel confinement frame resisting Y-direction expansion, more deflection would be expected in this direction when compared to the X-direction if the pressure exerted by the ASR-induced expansion is relatively uniform; this reasoning would explain the differences in the Y-direction and X-direction expansions of the CASR specimen.

The volumetric expansion of the two reactive specimens is shown in Figure 2.10. Other studies have concluded that ASR-induced volumetric expansion is independent of stress state or boundary conditions when at least one direction is unloaded or unconfined (Multon and Toutlemonde, 2006; Gautam et al., 2017). The volumetric expansion of the two reactive specimens is nearly equivalent after one year of accelerated testing confirming these conclusions even for large-scale specimens.

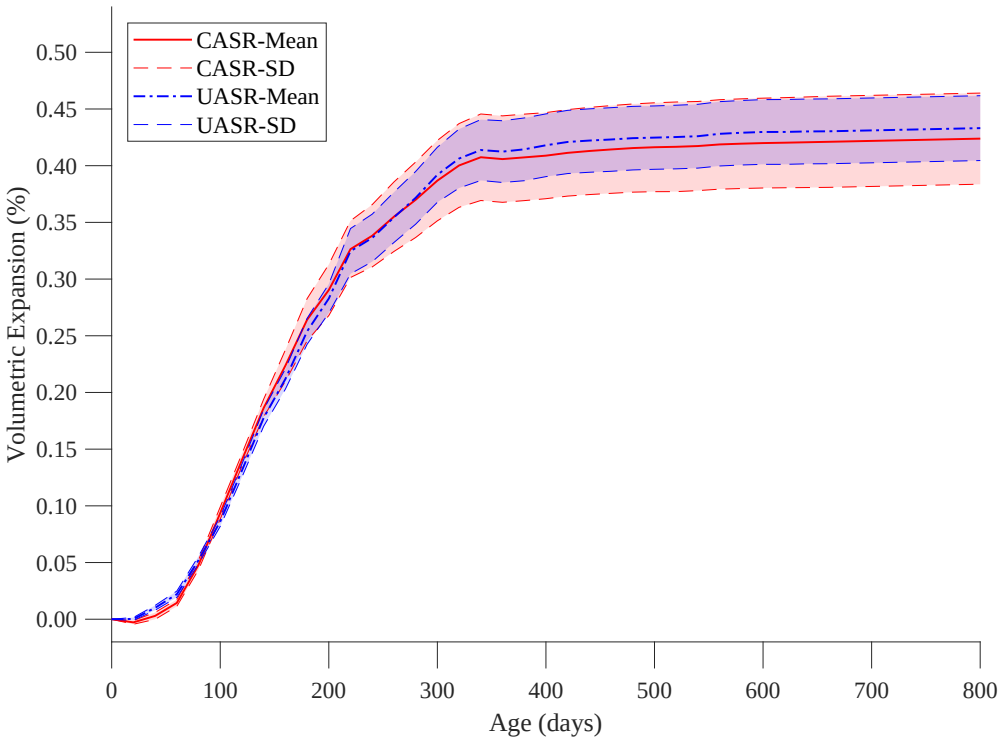

Figure 2.10: Volumetric expansion of reactive specimens

2.4.4 Material Properties

Figure 2.11 and Figure 2.12 present the respective evolution of the compressive strength and elastic modulus with time, collected on cylinders made of the non-reactive concrete (CTRL) and reactive concrete allowed free-expansion (UASR) or confined in metallic mold (CASR) While the elastic moduli show similar evolution for all specimens until 28 days, the CTRL present a much higher gain in strength at a lower age. The difference in compressive strengths between the reactive (CASR and UASR) and unreactive (CTRL) concrete specimens can be attributed to the addition of sodium hydroxide to the reactive concrete mix. Research has found that the addition of sodium hydroxide to concrete causes a significant reduction in compressive strength due to the formation of porous cement paste; however, the modulus of elasticity is not affected by the addition of sodium hydroxide (Smaoui et al., 2005). Following a hardening until about 200 days, the compressive strength measured on the CASR and UASR specimens exhibit a decrease apparently independent of the confinement. The elastic moduli collected on the reactive sample specimens show a rapid decrease at a relatively

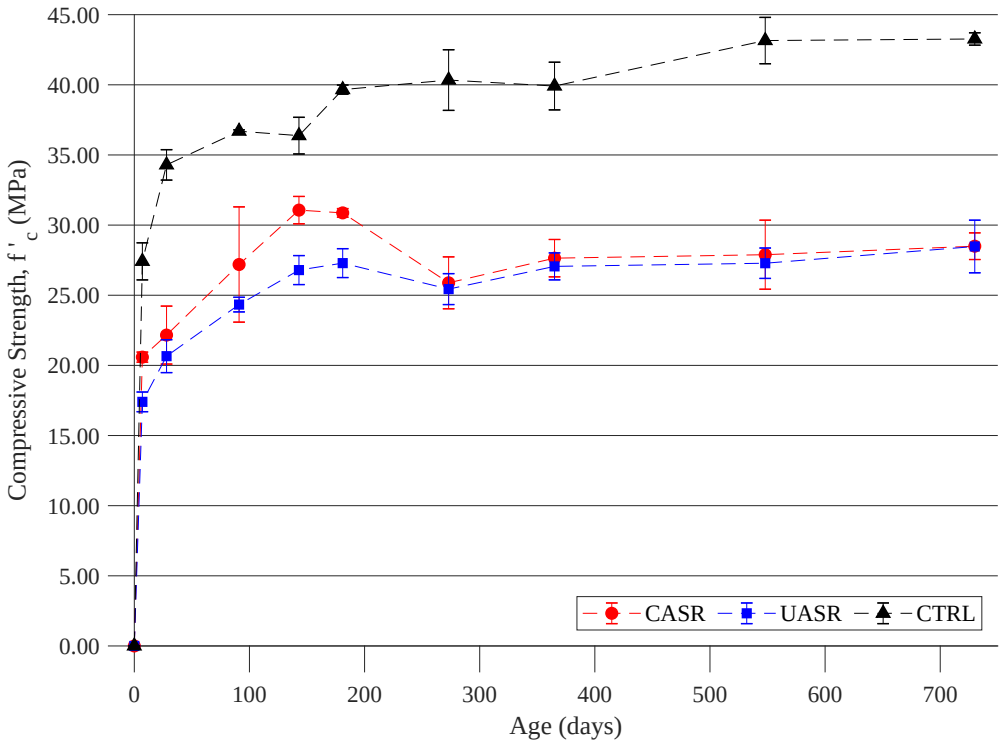

Figure 2.11: Change in compressive strength with time.

young age. The UASR specimens exhibit higher loss of elastic moduli (>50% loss at > 250 days) than the confined specimens (≈25% at > 250 days).

2.5 Discussions

2.5.1 Visual Inspection

The CASR and UASR specimens were periodically inspected for surface cracking. After the first surface cracking was observed, inspection was conducted monthly for new surface cracks. Visible surface cracks were marked with different colors at each inspection to capture the periodic time history of surface cracking. The side surfaces (X-Z and Y-Z planes) and top surface (X-Y plane) of the UASR specimen and the top surface of the CASR were periodically inspected. The side surfaces of the CASR specimen could not be inspected because of the steel confinement frame.

Visible cracking first occurred on the lateral sides of the UASR specimen with an early (≈ 150 days) primary crack orientation indicating a preferred direction of expansion

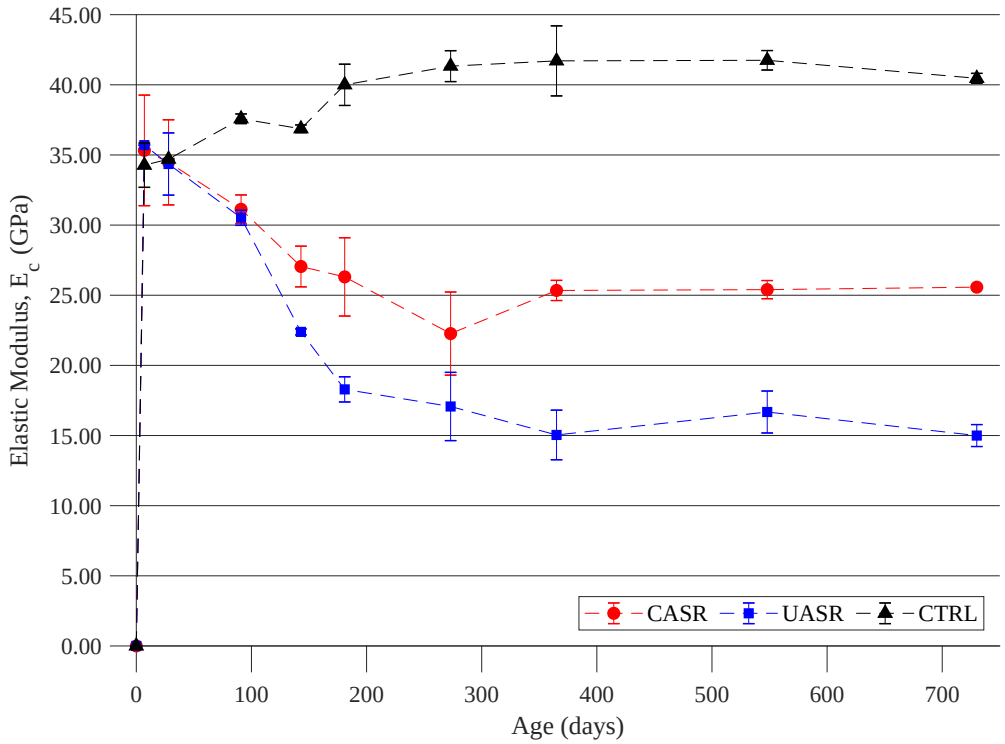

Figure 2.12: Change in elastic modulus with time.

through the thickness, in agreement with the measured strains. At a later stage, branching and pattern-cracks developed on the sides as shown in Figure 2.13. Limited and hardly discernible cracking could be observed on the top surface of the UASR specimen after ≈ 300 days. Figure 2.14 shows observations of first visible cracking on the UASR specimen and corresponding levels of expansion. However, no cracking was observed on the top surface of the CASR specimen at one year of accelerated testing. Minor cracking was noticed on the top surface of the UASR specimen after two years.

In a NPP containment structure, the cracking that would occur generating through-thickness expansion would not be observable as containment structures are typically continuous walls, and hence, the thickness plane is not accessible similar to the CASR specimen in this research. As a result, assuming that the development of ASR-induced cracking follows a similar chronology in the field, visual inspection may not be a reliable approach to diagnose the formation of ASR in concrete structures without transverse reinforcement until an advanced stage of development.

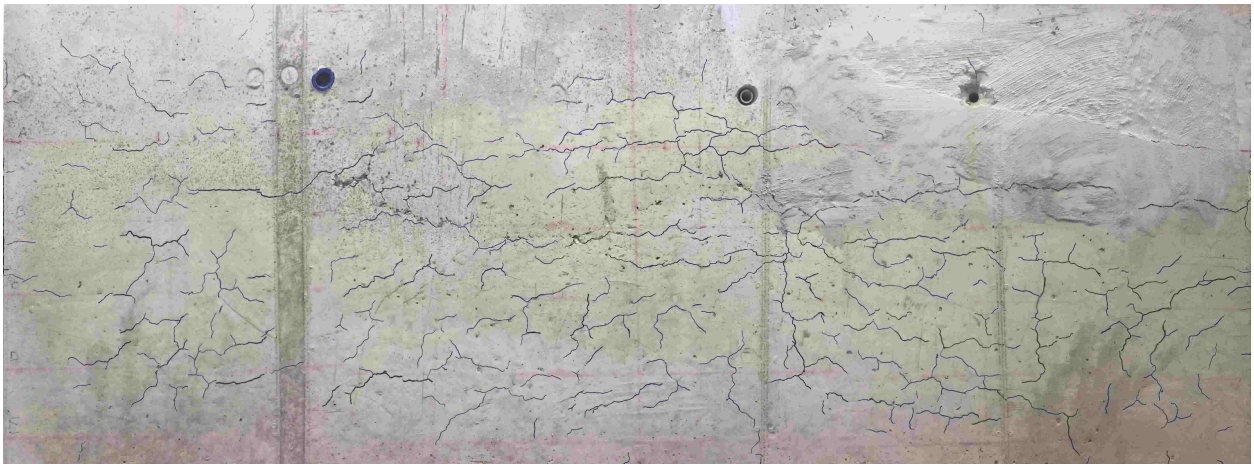

Figure 2.13: Cracking on a side of the UASR specimen
Note: Image shown is one side of specimen (3.5 m × 1.0 m)

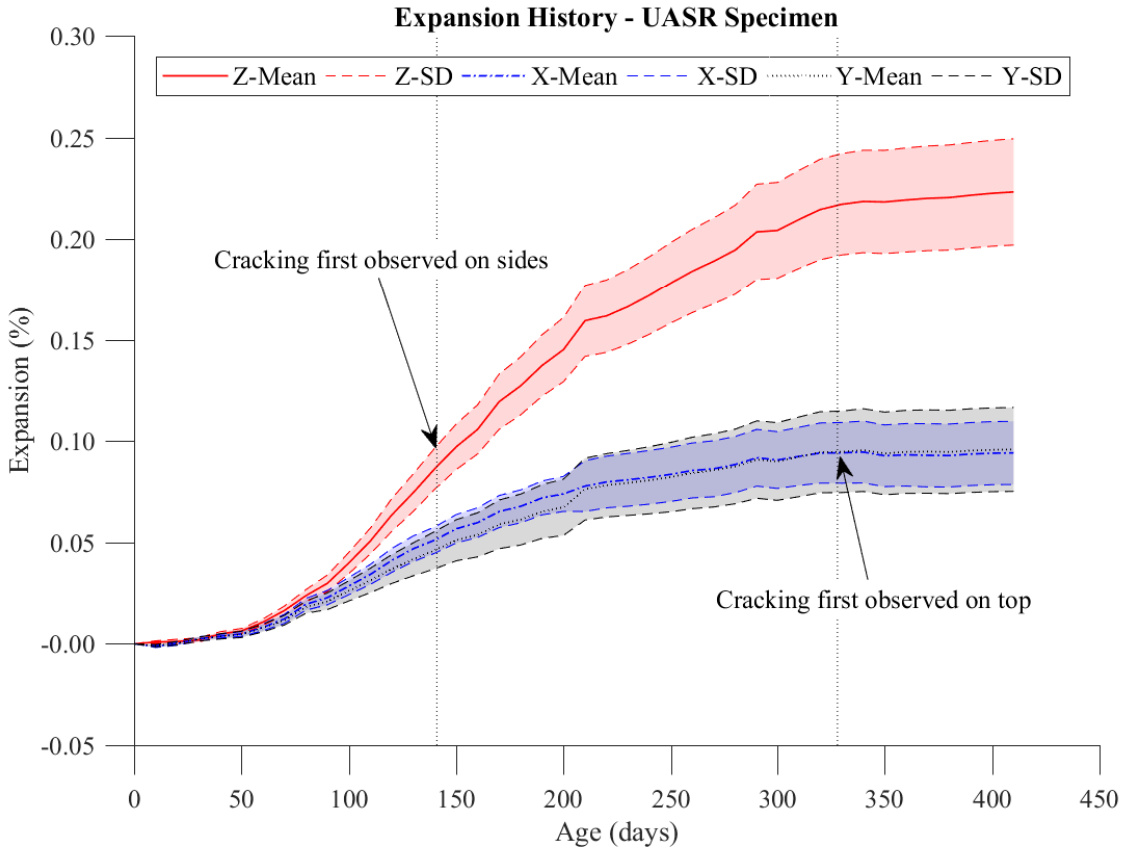

Figure 2.14: Expansion history of UASR specimen denoting times during accelerated testing when cracking was first observed (Hayes et al., 2018)

2.5.2 Sensor Resilience

The high moisture content, fairly high-temperature, and high-alkalinity of the operating environment poses a significant challenge to the the durability of the sensors. Of the 64 strain transducers and 12 long-gauge FO extensometers embedded in the specimen or attached to the surface of concrete, only one long-gauge FO sensor was lost as a result of unrelated construction works of the environmental chamber.

The long-gauge FO deformation sensors have proven to be a rugged and robust sensor. Three conclusions for these sensors can be made from the monitoring campaign: (1) the sensors are resilient to the harsh environment presented by the environmental chamber; (2) the sensors are easily affixed to concrete surfaces; (3) the sensor measuring device and software are reliable and simple to use. For these reasons, the long-gauge FO deformation sensors have strong potential for field implementation as an automated method to track residual expansion of ASR-affected structures.

2.5.3 Expansion Anisotropy

The macroscopic expansion measured on both reactive specimens is strongly anisotropic. While this can be attributed, to some degree, to the casting direction of the concrete specimens (Smaoui et al., 2004), most of the anisotropy of the macroscopic expansion measured in the present research stems from the boundary condition (steel confinement frame) and reinforcement layout. Figure 2.15 presents both CASR and UASR vertical (Z) expansions as a function of one-third volumetric expansion. Figure 2.16 shows the CASR and UASR expansion in the X direction as a function of one-third volumetric expansion. On both figures, the identity line represents a situation of perfectly isotropic expansion.

Both specimens exhibit anisotropic expansion with a preferred direction along the thickness of the specimens (Z). For the UASR specimen, this anisotropic expansion is caused by the difference in reinforcement ratio between the in-plane directions (X,Y) and through-thickness direction (Z) in addition to the preferred expansion attributed to casting direction. For the CASR specimen, the anisotropic expansion is caused by both the reinforcement and the passive restraint from the steel confinement frame, the latter accounting for a

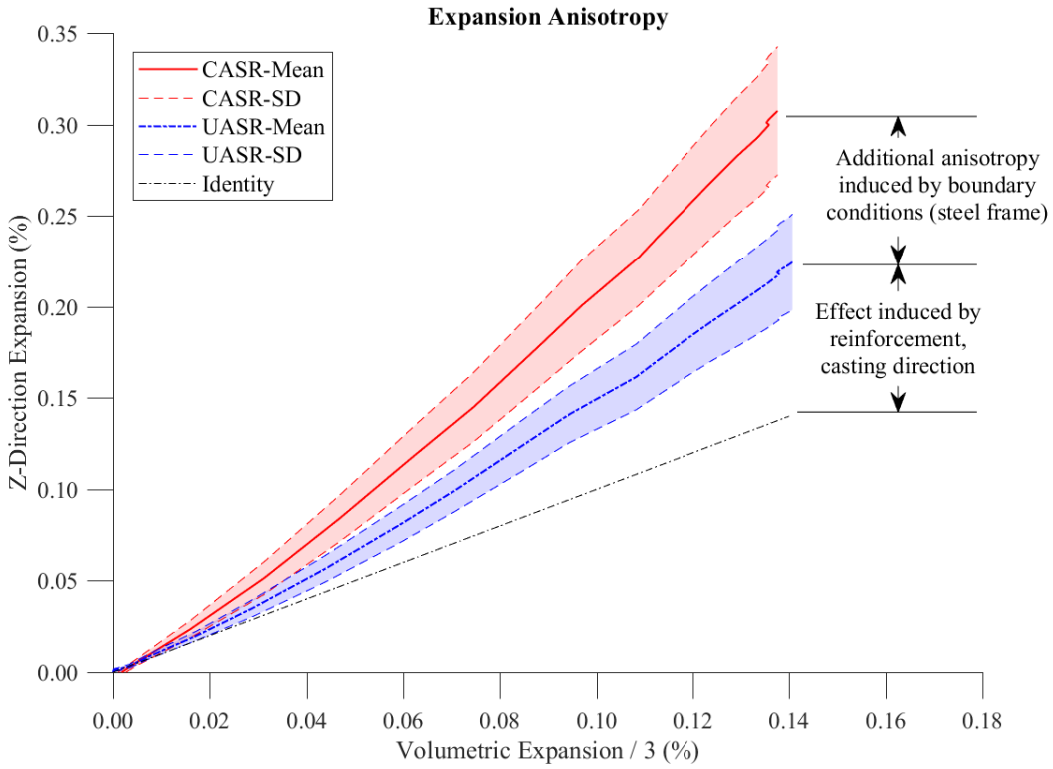

Figure 2.15: Z-direction expansion as a function of one-third volumetric expansion (Hayes et al., 2018)

33% increase in vertical (Z) expansion compared to the UASR specimen after one year of accelerated testing.

The effect of the boundary conditions is particularly noticeable in the in-plane directions. The expansion of the CASR specimen in the X-direction is notably lower after one year of accelerated testing when compared to the expansion of the UASR specimen in the same direction. The additional restraint of the boundary condition (steel confinement frame) accounts for a 50% reduction in X-direction expansion. The boundary condition produces a similar effect on the Y-direction expansion; however, the additional reduction of expansion due to the confinement is less than that of the X-direction reduction due to the longer span of the steel confinement frame resisting Y-direction expansion.

This anisotropy in the macroscopic expansion is likely to be related to a preferred orientation of the ASR-induced cracks under local stress. Due to the specific geometry of the reinforcements, the stress distribution is non-uniform across each specimen, making it

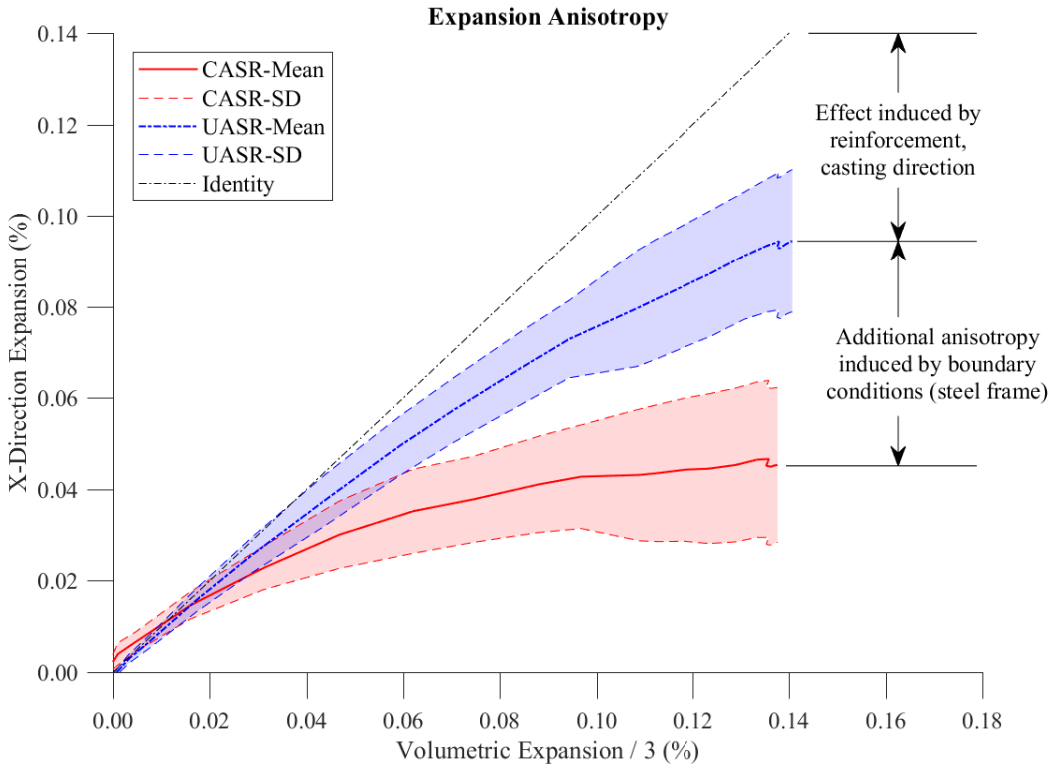

Figure 2.16: X-direction expansion as a function of one-third volumetric expansion (Hayes et al., 2018)

difficult to analyze the cracking distribution and therefore the anisotropy in macroscopic strain without relying on nonlinear numerical analysis. This experimental campaign represents a good opportunity to test and validate structural models for ASR, notably to check whether such a model can capture the anisotropy of the macroscopic strain.

2.5.4 Effect of Confinement on Materials Properties

Figure 2.17 and Figure 2.18 show the respective evolution of the relative modulus of elasticity, and compressive strength (normalized by the values of these properties at 28 days after casting) with the averaged expansion measured on the corresponding large specimens. It must be noted that the expansion of the large specimens is not necessarily representative of the expansion of cylinders. However,the measured expansion on the large specimens is used as a reference to compare the behavior of the CASR and UASR cylinders.

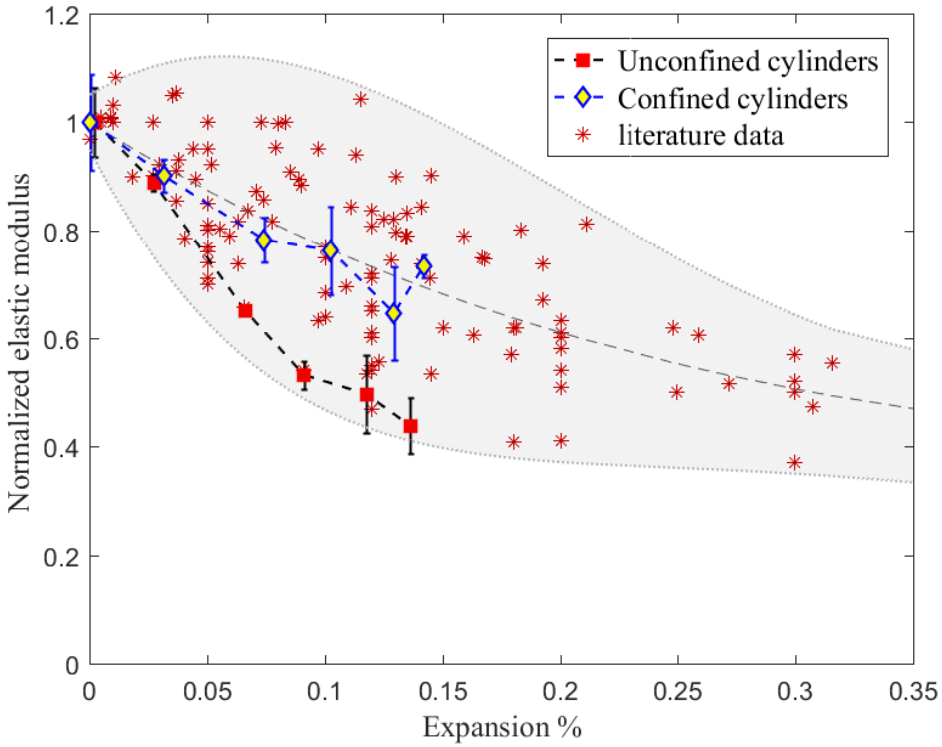

Figure 2.17: Change in relative elastic modulus with ASR expansion (Hayes et al., 2018). The values of elastic modulus from each data set are normalized to the corresponding value at 28 days. The gray area represents an envelope of the literature data collected from Jones and Clark (1996); Batic et al. (2004); Multon et al. (2005); Ben Haha (2006); Hafçi (2013); Sanchez (2014); Na et al. (2016); Sanchez et al. (2016); Gautam (2016); Esposito et al. (2016); Giannini and Folliard (2012).

Figure 2.17 compares the evolution of elastic modulus in the confined and unconfined cylinders. It can be seen that the stiffness degradation in the UASR cylinders was significantly higher than that in the CASR cylinders. While the relative modulus of elasticity of the UASR cylinders decreased to 43% at a linear expansion of 0.12%, the CASR relative modulus decreased to 63% of the relative modulus of elasticity at an estimated linear expansion of 0.13% and slight recovery was noticed afterward. This behaviour may be attributed to the contribution of the lateral confinement stress in reducing the loss of the elastic modulus (Gautam et al., 2017).

As shown in Figure 2.18, both the UASR and CASR cylinders showed a remarkable gain in compressive strength until an estimated expansion of about 0.10% and followed by noticeable reduction at an expansion of ≈0.12% before a partial gain was observed. As two

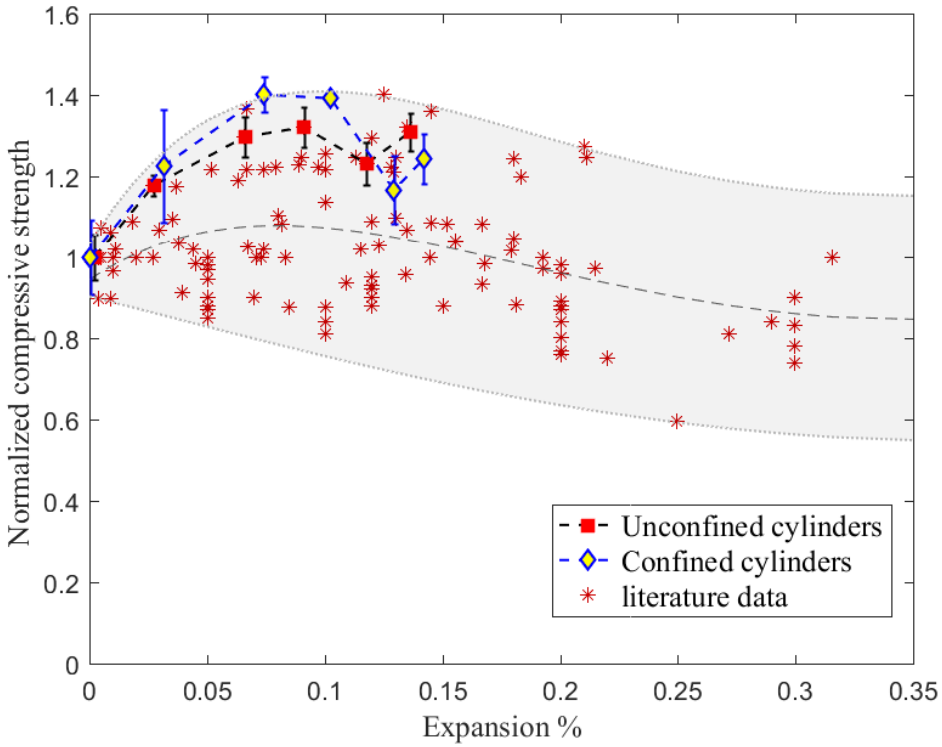

Figure 2.18: Change in relative compressive strength with ASR expansion (Hayes et al., 2018). The values of compressive strength from each data set are normalized to the corresponding value at 28 days. The literature data are collected from Swamy and Al-Asali (1988b); Batic et al. (2004); Jones and Clark (1996); Ben Haha (2006); Hafçi (2013); Na et al. (2016); Fan and Hanson (1998); Ahmed et al. (2003); Giaccio et al. (2008); Multon et al. (2005); Sanchez (2014); Sanchez et al. (2016); Gautam (2016); Esposito et al. (2016); Giannini and Folliard (2012).

competing mechanisms, the ongoing hydration of cement and ASR damage, were progressing during early stage of expansion, the increase in compressive strength due to cement hydration seemed to overcome the loss of strength due to ASR (Multon et al., 2005; Na et al., 2016). At later stage (i.e., for expansion $> 0.1\%$), the ASR damage effects seemed to be dominant. It must also be noted that the compressive strength was affected by the direction of ASR-induced damage, the CASR cylinders (where cracking is primarily oriented parallel to the loading direction) showed higher strength values than that of the UASR, except for the last measurements the UASR was higher.

The slight recovery of the mechanical properties at a late stage of ASR expansion was reported in the literature (Swamy and Al-Asali, 1988b; Ahmed et al., 2003; Gautam, 2016).

This recovery can be attributed to the continuation of cement hydration process (Swamy and Al-Asali, 1988b), or to the transformation of ASR gel in cracks into a more calcium-rich gel (eventually resembling C-S-H gel) which can contribute to the concrete regaining strength and stiffness (Gautam, 2016).

2.6 Conclusion

1. Three large-scale specimens, representative of concrete structural members thickness and reinforcement ratio without transverse reinforcement found in LWR NPP, were fabricated, heavily instrumented and monitored under controlled accelerated ASR conditions at 38 °C and ≈ 95% RH

2. The different types of deformation instrumentation, i.e., long-gauge fiber optics or embedded transducers, have yielded comparable and dependable expansion measurements despite the severity of the operating conditions, i.e., moderate temperature, high humidity and high alkalinity.

3. Casting direction anisotropy, reinforcement layout, and boundary conditions cause highly anisotropic expansion pointing to the need for advanced structural models capable of capturing expansion anisotropy for analysis of in-the-field behavior.

4. Surface cracking is not indicative of internal ASR-induced damage or expansion for concrete structures where reinforcement layout or confinement drives expansion primarily in an unobservable plane direction; This potentially allows ASR to cause significant distress to the structure without any visible evidence of its presence.

5. Visible surface cracking was not evident on the CASR specimen even with Z-direction expansion exceeding 0.3%. Given that acoustic NDE methods are most influenced by the onset of ASR damage (Giannini and Folliard, 2012; Giannini et al., 2016; Kim et al., 2017), the observations of the CASR specimen highlight the need to monitor critical NPP structures before visible evidence of damage appears at the surface, and support the concept that online monitoring of these structures using acoustic methods can provide information not available from visual inspection

Chapter 3

Effect of Alkali-Silica Reaction on the Fracture Properties of Confined Concrete

3.1 Introduction

Alkali-silica reaction (ASR) is an internal reaction-induced expansive mechanism that potentially causes cracking and large deformations in concrete structures. While this degradation mode has been quite commonly reported for transportation infrastructures and hydropower-generating stations, a few instances of ASR have been recently discovered in critical concrete structures in nuclear power plants (NPPs) in Canada, Japan, and the United States (Takatura et al., 2005; Shimizu et al., 2005; Tcherner and Aziz, 2009; U.S. Nuclear Regulatory Commission, 2011; NextEra Energy Seabrook, 2013). In NPPs, structural members with thickness ranging from 0.60 to 1.5 m are commonly found in buildings enclosing or adjacent to the reactor vessel. The absence of shear reinforcement (i.e., in the direction of the wall thickness) permitted by older versions of American Concrete Institute (ACI) 318, "Building Code Requirements for Reinforced Concrete," is common. The reinforcement layout and boundary conditions generate confinement that induces a preferred ASR expansion in the unreinforced direction (Hayes et al., 2018). During an accident design

scenario, the contribution of the reinforced areas and the residual shear capacity of ASR-affected structures (e.g., biological shield building, the containment building, and/or the fuel handling building) rely on the plain concrete shear resistance that is expected to depend on two competitive mechanisms pending the occurrence and extent of ASR: (i) the in-plane, confinement-induced compression in the direction of the reinforcement, potentially limiting the propagation of such fracturing, and (ii) the effects of the density and orientation of the micro-cracking on the propagation of a shear fracture, which is the focus of the research presented here.

While abundant literature can be found on the effects of ASR on the tensile strength of concrete (Nixon and Bollinghaus, 1985; Swamy and Al-Asali, 1988a; Siemes and Visser, 2000; Esposito et al., 2016), published data on the effects of ASR on the post-peak behavior of ASR-induced pre-damaged concrete in tension are scarce. "Testing three-point bending notched beams specimens," (Miki et al.) (Miki et al., 2013; Miki and Tsukahara, 2016) found that the fracture energy of the ASR-affected specimens tends to be higher than the nonreactive control specimens. These authors attributed the extended post-peak ductility to an increased and more convoluted fracture length caused by the pre-existing ASR-induced cracks obtained from the free expansion of the specimens. In contradiction, Rotter et al. (Rotter et al., 1998) compare the fracture properties of notched concrete cubes of different concrete compositions and storage conditions (20 °C and 38 °C). The specimens were all tested after 2 years. With increasing ASR-induced expansion, both peak load and fracture energy appear to decrease. Similar conclusions were generally reached by Giacco et al. (Giaccio et al., 2008), although the opposite was found with concrete specimens made of a relatively slow-reactive aggregate. Previous research on the effects of ASR on fracture properties suggests that the internally induced cracking pattern, density, and location greatly affect the propagation of the fracture path, length, and process zone.

In addition, ASR-induced cracking orientation and expansion directions are governed by the external principal stresses (Larive, 1997; Multon and Toutlemonde, 2006; Dunant and Scrivener, 2012; Morenon et al., 2017; Hayes et al., 2018). Under triaxial loading, the expansion vanishes beyond a certain isotropic pressure, which is estimated at around 7–10 MPa (Multon and Toutlemonde, 2006; Saouma and Perotti, 2006). Under uniaxial or

biaxial loading, the expansion appears to be redistributed in the unloaded directions. ASR-induced expansion resulting essentially from the formation of cracking was eventually filled with expansive gel. The damage in the unloaded direction—cracking opening primarily oriented perpendicularly to the loading direction–is more important than in the loading direction (Dunant and Scrivener, 2012; Morenon et al., 2017). Hence, under anisotropic loading, the distribution of ASR-induced crack orientations can be expected to exhibit a tendency to be highly oriented. Such loading anisotropy is common in the field as the result of structural restraints in service. However, during accident scenarios such as seismic events, impacts, or over-pressurization, the direction of the loading that potentially leads to failure may not be colinear with the in-service loading. This raises the question of the resulting fracture propagation within a pre-cracked, anisotropic medium.

The objective of the research presented here is to quantify the fracture properties (stiffness, strength, and fracture energy) of ASR-induced anisotropically damaged concrete specimens by varying the damage level and the relative direction of the ASR-induced cracking orientation against the loading direction corresponding to the fracture propagation. The ASR-induced anisotropic damage was obtained by restraining the lateral expansions of large concrete cylinders (66 cm diameter) from which WST specimens were extracted. The WST specimens were cut so that the direction of the notch varies with the expected preferential orientation of the ASR-induced cracks.

3.2 Materials and Methods

3.2.1 Materials

The specimens were prepared alongside large-scale reinforced concrete blocks and several standard size cylinders for standard material testing, all using the same mixes, as described by Hayes et al. (2018). In the research described by Hayes et al. (2018), three large-scale blocks (two expanded due to ASR and one served as control), all with dimensions of 3.5 by 3.0 by 1.0 m, were cast with an array of sensor systems to measure expansion in each primary direction. One of the specimens was confined with a manufactured steel frame to

Table 3.1: Design proportions of concrete mixtures (Hayes et al., 2018)

Materials	Quantity, kg/m^3	
	Reactive	Control
Coarse aggregate	1180	1180
Fine aggregate	728	728
Cement	350	350
Water*	175	175
50% NaOH solution	9.8	-
30% $LiNO_3$ solution	-	11.9
Water-reducer admixture	1.3 mL/kg	1.3 mL/kg
Stabilizer admixture	1.3 mL/kg	1.3 mL/kg

Note: Aggregate quantities are given for oven-dry materials. Water quantities assume aggregates in saturated-surface dry (SSD) condition. (*) indicates that 70% of the mass of mixing water was replaced by ice to mitigate early-age cracking, and the actual w/c ranged between 0.46 and 0.52.

force majority of the expansion in the shortest dimension. The WST concrete specimens used in this study were prepared at the same time as the large-scale blocks described by Hayes et al. (2018). Estimates for expansions of the specimens presented in this study were gathered from these large-scale blocks.

The concrete had a water-cement ratio of 0.5 and used a low-alkali Type-II Portland cement with an equivalent alkali content of 0.41% Na_2O_{eq}. The ASR was promoted in the reactive specimen by adding 50% w/w sodium hydroxide solution (NaOH) to the mix water. This raised the alkali content of the concrete to to 5.25 kg/m^3 (1.50% Na_2O_{eq} by mass of cement). The expansion of the ASR product was mitigated in the control specimens by adding 30% w/w lithium nitrate ($LiNO_3$). For both mixes, a high-range water-reducing admixture and hydration stabilizer were added to control the slump and to delay the setting time given the warm ambient temperatures during casting and placement. The mix proportions for both reactive and control mixtures are reported in Table 3.1.

The coarse aggregate was obtained from crushed siliceous rock that was composed of argillite, with no other discernible mineral or rock types. The argillite was found to be potentially highly reactive in concrete and susceptible to deleterious ASR due to the presence of abundant strained quartz, microcrystalline quartz, and possibly opal. The coarse aggregate is size gradation specification #57 according to AASHTO M43 with nominal size of 4.75 - 25.0 mm. The manufactured sand from the Midway, Tennessee, area was found to be nonreactive per ASTM C1260 testing.

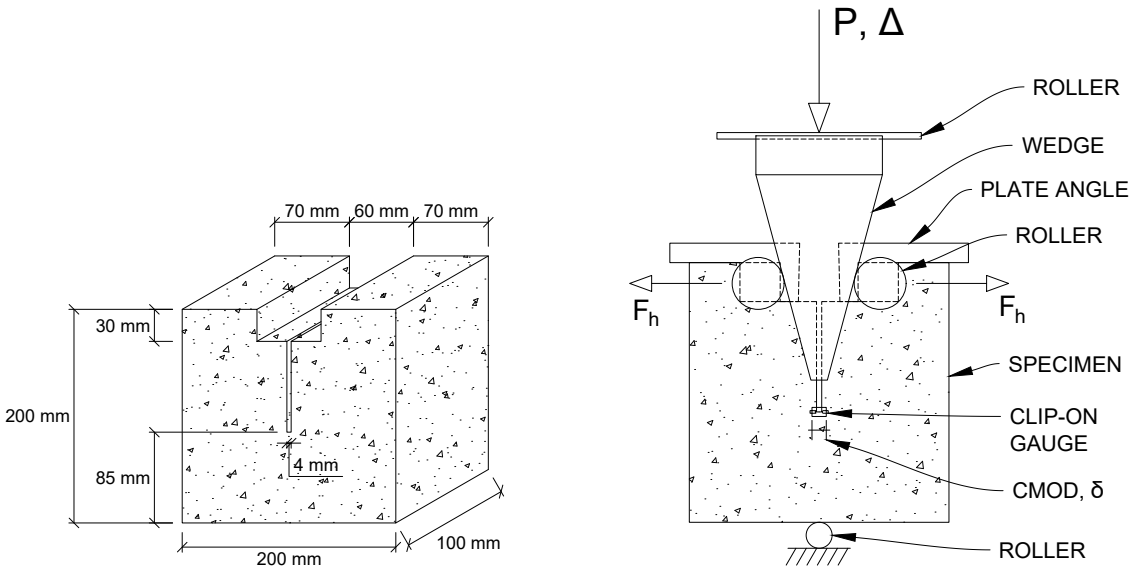

(a) Test specimen dimensions **(b)** Loading apparatus

Figure 3.1: Test specimen details

3.2.2 Specimens

The WST, first developed by Brühwiler (Brühwiler, 1988; Brühwiler and Wittmann, 1990), is used in the current study to measure the fracture energy of ASR-affected concrete. This specimen geometry is similar to that of a compact tension specimen commonly used to determine the fracture properties of metals. Tension is generated in the specimen by the splitting force induced by a wedge driven between the raised portions of the specimen with the crack mouth forming at the notch tip in the specimen's design, as shown in Figure 3.1b. The specimen dimensions are shown in Figure 3.1a. The design of the loading apparatus was adapted from works by Denarie (Denarié, 2000; Denarié et al., 2001, 2006).

Five different classifications of WST specimens were established: four specimen types that were subjected to ASR with varying constraints or orientation, and one specimen type to serve as the nonreactive control. The types of specimens are listed in Table 3.2. The first three types of specimens subjected to ASR consist of specimens with different primary crack orientation generated by ASR-induced expansion under passive confinement. The first type of specimen, labeled "00D" or 0°, was exposed to ASR under confinement and was cut to feature a primary crack orientation perpendicular to the notch of the specimen. The second type of specimen, labeled "45D" or 45°, was exposed to ASR under confinement and

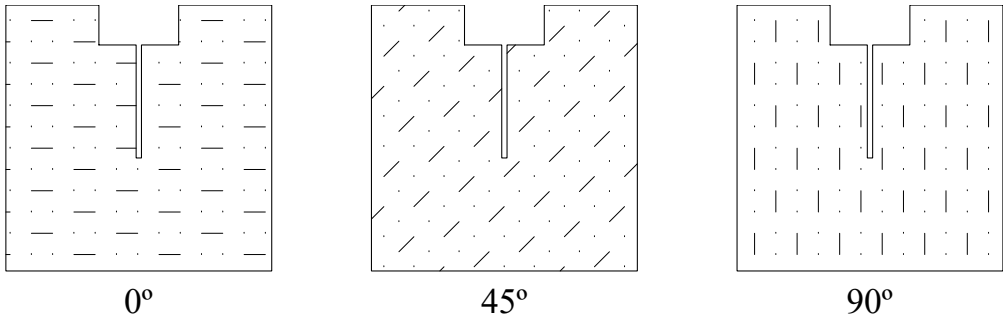

Figure 3.2: Test specimens' primary expected crack orientations

Table 3.2: Types of WST specimens

Label	Reactive	Primary crack orientation (°)
00D	Yes	0
45D	Yes	45
90D	Yes	90
UNC	Yes	None
CON	No	No cracking

cut to feature a primary crack orientation at 45 degrees to the line formed by the notch. The third type of specimen, labeled "90D" or 90°, was exposed to ASR under confinement and cut to feature a primary crack orientation parallel to the notch. These three types of specimens with varying primary crack orientation are illustrated in Figure 3.2. The fourth type of specimen, labeled "UNC", was exposed to ASR without confinement (unconfined). The fifth and last type of specimen, labeled "CON", served as the control classification and was not subjected to ASR expansion or confinement. In addition to the WST specimens, standard-size cylinders were prepared for materials characterization. The elastic modulus and compressive strength for these cylinders are reported by Hayes et al. (2018).

To achieve different ASR-induced crack orientations, the WST specimens were initially cast in 15.875 mm thick rolled ASTM A36 steel plate tubes of 66.0 cm outer diameter and either 20.3 or 40.6 cm in height, as shown in Figure 3.3. Concrete was poured into these steel tubes to induce passive confinement during expansion and to cause ASR-induced expansion to occur primarily through the thickness. The radial confinement, similar to the setup used by Multon and Toutlemonde (2006), induced ASR micro-cracking in planes perpendicular to the axis of the cylinder. A sheet of high-density polyethylene was placed on the inside diameter of the steel tube before pouring to reduce the friction as the concrete expanded

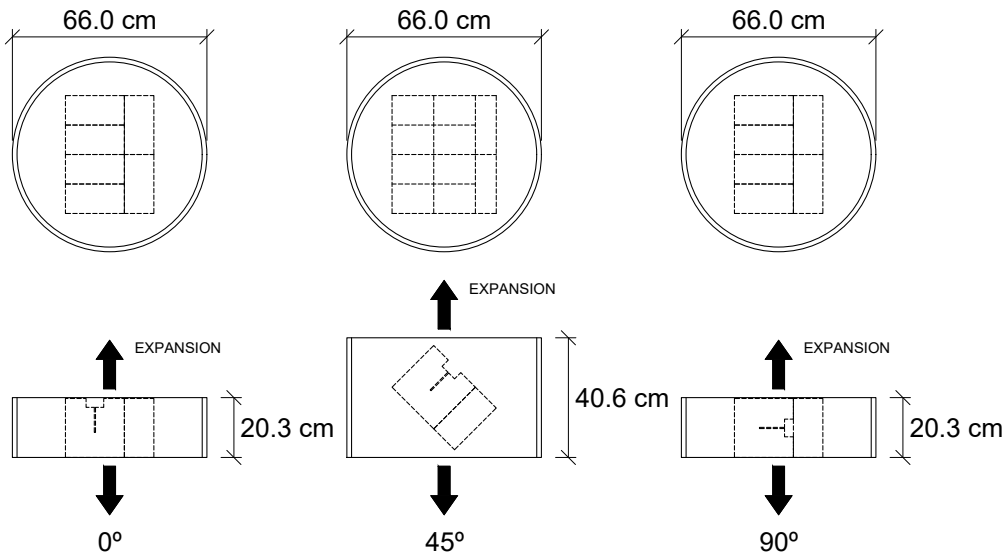

Figure 3.3: Cutting plan for different WST specimens

through the thickness. An example of a large concrete cylinder inside steel confinement is shown in Figure 3.4. Unrestrained specimens subjected to ASR and control specimens were cast in wooden forms and then were removed from these forms shortly after casting. These forms were made using lumber and plywood, and they included small steel plates to form the notches of the specimens. Dimensional differences between cut and cast specimens rarely exceeded 6 mm for the outer dimensions, and 1.5 mm for the depth of the notch. No significant difference was found in the widths of the notches in any of the specimens.

For a duration of approximately 26 days, all specimens were covered to prevent moisture loss and left in lab space at an average temperature of 24°C. At a concrete age of 26 days, the construction of an environmental chamber around the specimens had been completed, providing an accelerated curing condition of 38°C and 95% relative humidity. Specimens were left in the accelerated curing conditions until a few days before cutting and/or testing.

Shortly before each test time, each concrete cylinder was cut after being removed from the steel plate tube confinement, creating six (6) individual WST specimens. The different orientations were obtained by cutting the specimens in one direction or the other, as shown in Figure 3.3.

Immediately after being cut or removed from the curing conditions, specimens were wrapped in plastic wrap to prevent moisture loss and placed in standard room temperature of

Figure 3.4: Photo of concrete inside confinement prior to cutting.

23°C prior to testing. In this reduced temperature, the expansion occurring between times of extraction and testing is minimal as evidenced by the measured expansion in large companion blocks after temperature reduction described by Hayes et al. (2018). Approximately 16 hours prior to testing, specimens were removed from the plastic wrap. Devcon (DevTube No. 14250) epoxy was applied to each specimen on either side of the notch tip, and MTS knife edges were set in place to be used in the measurement of the crack mouth opening displacement (CMOD), δ. The epoxy was allowed to set overnight for at least 16 hours prior to testing, as recommended by the manufacturer.

3.2.3 Testing

WSTs were performed with a K25 loading machine system with 445 kN capacity and corresponding system load cell precision of 0.5% of full scale, equating to roughly 98 N. CMOD, δ, measurements were taken using an MTS 632-02B-20 clip-on strain gauge with a range of 5.08 $\pm$ 2.54 mm and precision of 25.4 µm. Load cell and clip-on gauge readings were collected and recorded by the system every tenth of a second for the duration of the test.

Testing was performed at three different time periods, as shown in Table 3.3, to capture the effect of ASR-induced expansion on the residual fracture properties. Six specimens of

Table 3.3: Concrete ages at significant times.

Test period	Age at removal* (days)	Age at testing (days)	Denomination
1	232	386	1Y
2	500	528	1.5Y
3	701	720	2Y

Note: (*) "Age at removal" refers to the age of concrete at the time when specimens were removed from curing conditions.

Table 3.4: Volumetric expansion of companion large concrete blocks.

Denomination	Confined (%)	Unconfined (%)
1Y	0.339	0.338
1.5Y	0.416	0.425
2Y	0.423	0.432

each type were tested at each time period, totaling 30 specimens per test period (except for the 45-degree specimens at 1 year which were not tested) for a total of 90 specimens across all testing periods. For reference, the volumetric expansion of the companion large blocks from Hayes et al. (2018) made of the same concrete at the time of removal from the climate chamber is reported in Table 3.4. The volumetric expansion curves of the large companion blocks are shown in Figure 3.5 with ages of removal marked. Reported values are lower boundary values of expected volumetric expansion, although minimal further expansion after removal is expected to have occurred based on the monitoring of the large-scale blocks expansions after temperature was decreased from 38 °C to 25°C.

Prior to loading, each specimen was equipped with steel plates and wedges, as shown in Figure 3.1b. Rollers were placed at the top of the wedge and on the bottom surface of the test specimen. Small steel fixtures were epoxied to the notch tip, and a clip-on strain gauge was placed on these fixtures in order to measure the δ. Each specimen was centered within the loading frame, and a very small load (< 100 N) was placed on the specimen to hold it in place while the clip-on strain gauge was attached. Each specimen was loaded during testing so that the loading head moved in compression at a rate of 1.67 $\mu m\,s^{-1}$. As load was applied, the wedge was driven between the rollers attached to the raised portions of the specimen, causing a splitting force (labelled F_h in Figure 3.1b) and generating crack(s) in the ligament area of the specimen.

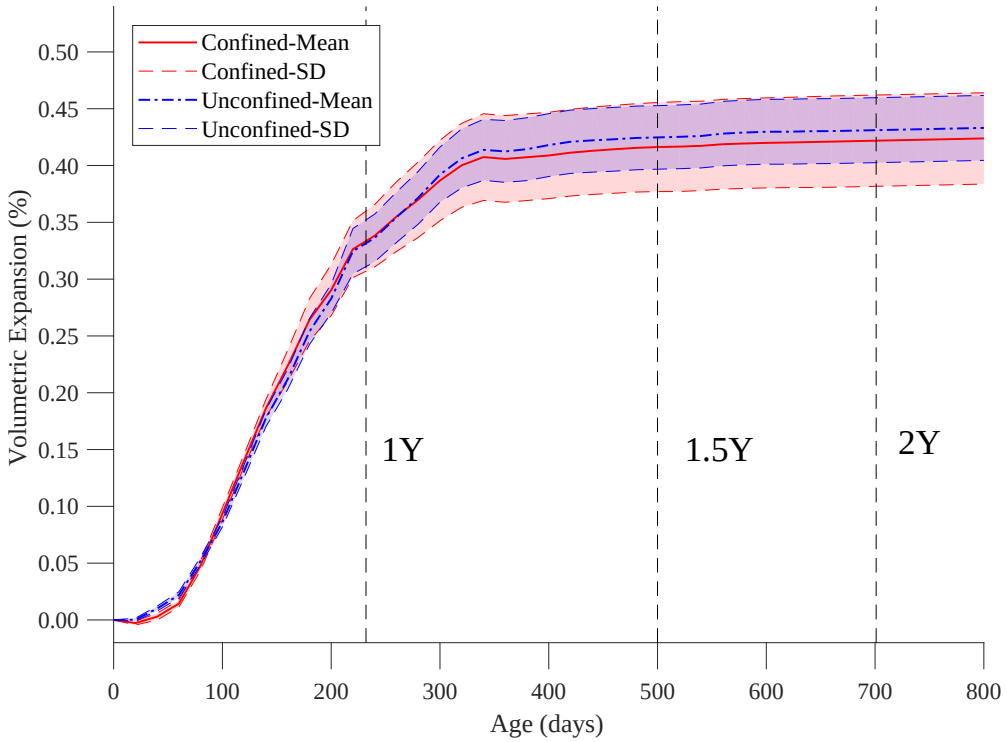

Figure 3.5: Volumetric expansion of companion large concrete blocks with ages of removal indicated.

Specimens were not tested to complete failure because safeguards were not in place to prevent damage to test equipment. Instead, testing of each specimen ended at a pre-selected value of δ in order to obtain a load-displacement curve that was as complete as possible. The value of δ was selected by performing trial tests. A value of δ located sufficiently larger than the value at peak load of these trial tests was selected for use on all specimens.

3.3 Results

3.3.1 Data analysis

Before performing data analysis, the measured peak loads of control specimens were adjusted. As shown in Figure 3.6, at a concrete age of 28 days, a time before ASR-expansion was present, a difference in tensile strength was present between the two mixes even with most mixture materials being the same. The difference in early age tensile strength is attributed

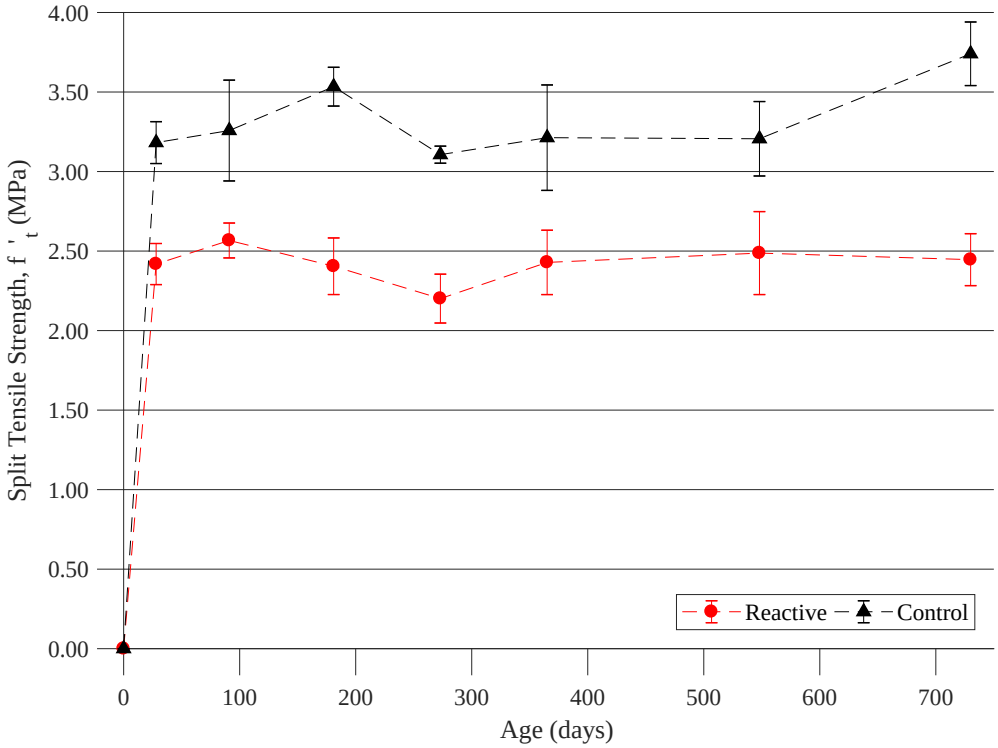

Figure 3.6: Splitting tensile strength of companion cylinders as determined by ASTM C496.

to the use of sodium hydroxide in the reactive mix which has been shown to reduce tensile strength (Smaoui et al., 2005). For the companion cylinders, the use of sodium hydroxide caused the tensile strength of the reactive mix to be approximately 3/4 of the strength of the control mix. It is also worth noting that splitting tensile strength was not reduced in the reactive companion cylinders with ASR-expansion over the course of 2 years. In order to account for the strength differences between the two mixes and provide better comparison between the reactive and control mixes, the measured sustained load of wedge-splitting control specimens was reduced by multiplying the load by a factor of 3/4.

The raw data for both the applied load, P as shown in Figure 3.1b, and measured δ were first zeroed. To conduct data analysis, the raw data were then smoothed by use of the MATLAB moving average method (`movmean`). The horizontal component of the applied load, F_h, was calculated using the angle of the splitting wedge $F_h = P/(2 * tan(15))$ Denarié

(2000). The smoothed data curve for each individual tested specimen was plotted as the splitting force, F_h, against the δ.

Typical force-displacement curves for each data set and curing time are shown in Figure 3.7. Each curve represents the specific load-displacement curve of an individual specimen selected to best represent each set. The control specimens present a sharp peak with a strong softening behavior, while the ASR-affected specimens generally demonstrate a lower rate of post-peak force degradation and frequently show a plateau of the load. The horizontal force is generally the lowest for the 90D specimens and the highest for the control specimens.

From each of these smoothed curves, the following parameters can be determined:

- The peak splitting force, F_{peak}, is measured as the maximum of the splitting force.
- The pseudo-elastic modulus E_{app} is taken as the initial slope of the force-displacement curve. It is determined as the slope of line passing through (F_h-δ) points where F_h equals 0% and 40% F_{peak}.
- The specific fracture energy, G_{fract}, was calculated by taking the quantity derived from trapezoidal integration of the smoothed force-displacement curve, up to a displacement of 0.2 mm, and then dividing by ligament area (85 x 100 mm) of the wedge-splitting specimen. Because the area under the $F_h - \delta$ curve was only calculated to a δ value of 0.2 mm, values for specific fracture energy reported in this study are likely lower than specific fracture energy of standard normal strength concrete reported in other studies.

3.3.2 Mechanical properties

The average peak force, pseudo-elastic modulus, and specific fracture energy for the different conditions and curing times are tabulated in Table 3.5 and plotted as histograms in Figure 3.8. The error bars in Figure 3.8 represent the standard deviation. For each specimen type and curing time, the average of up to 6 specimens was taken. Data from specimens presenting a very high number of visual defects (see Section 3.4.1 below) have been excluded from the data analysis. The error bars represent the standard deviation for each set.

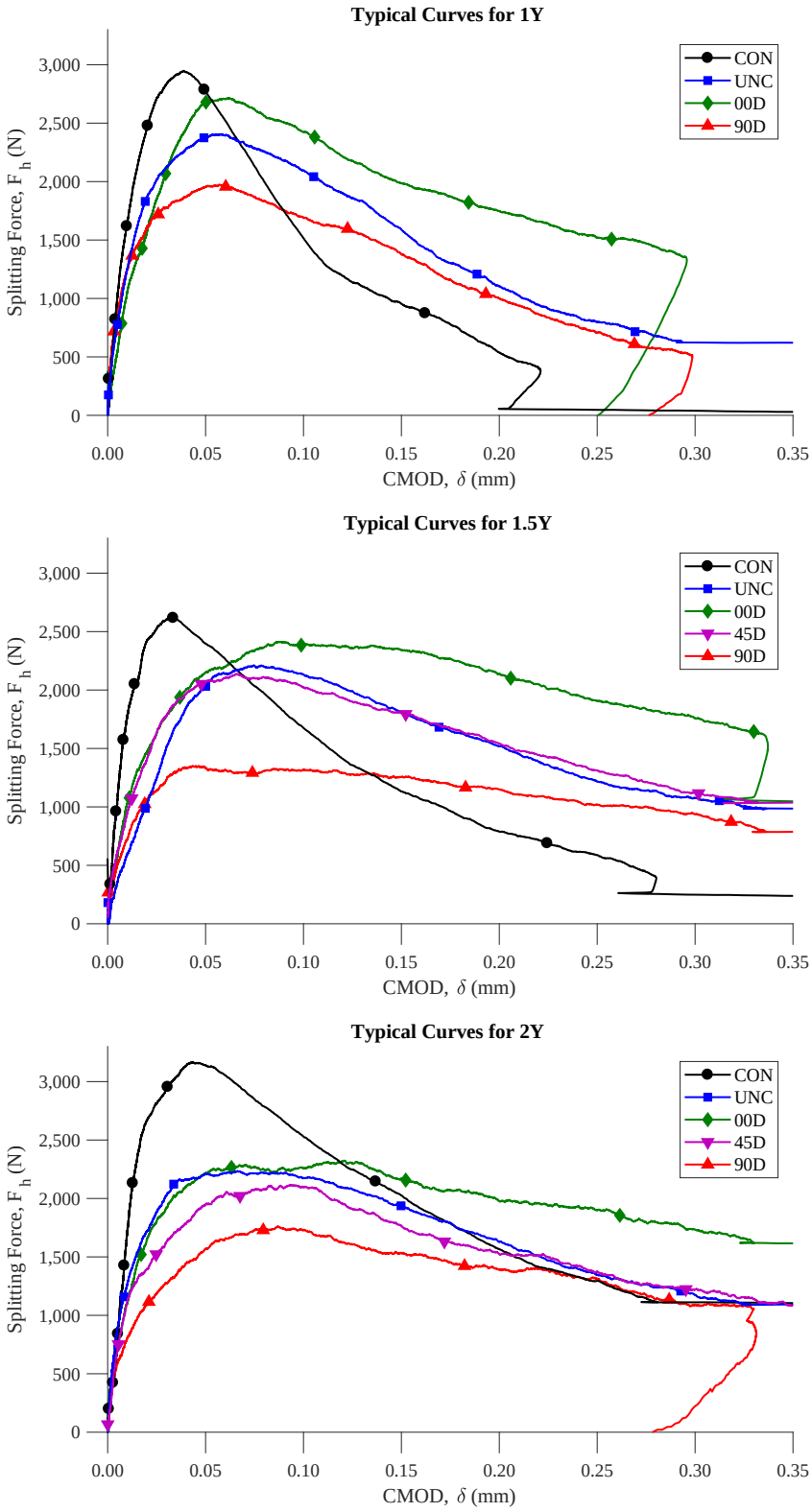

Figure 3.7: Typical smoothed force-displacement curve for each data set and curing time.

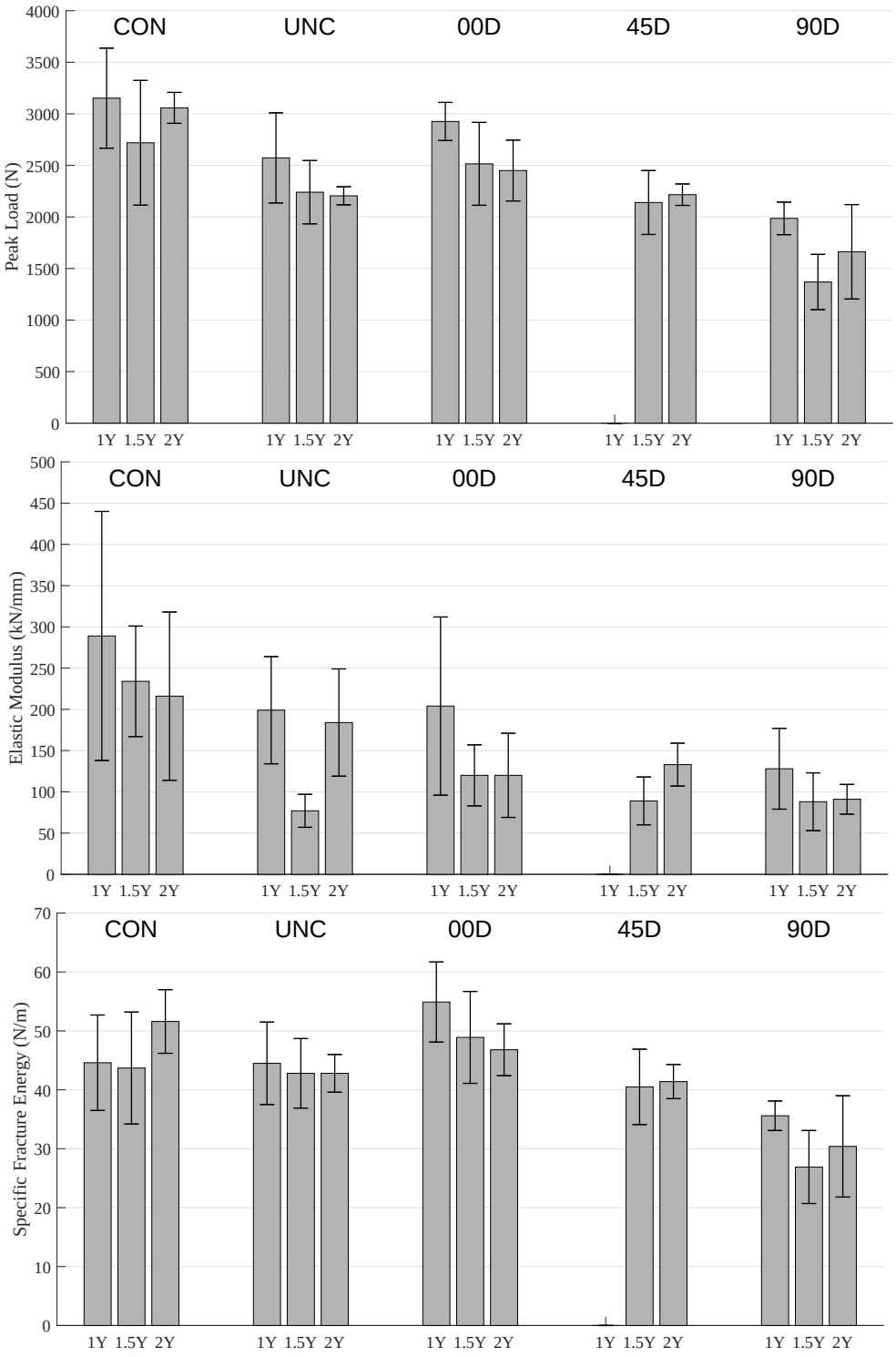

Figure 3.8: Average peak force (top), pseudo-elastic modulus (middle) and fracture energy (bottom) for all specimen types and all curing times. The error bars correspond to the standard deviation for each set. The 45D specimens were not tested at 1Y.

Table 3.5: Average peak force, pseudo-elastic modulus, and specific fracture energy for all specimen types and all curing times.

Property	**Age**	**Specimen Type**				
		CON	*UNC*	*00D*	*45D*	*90D*
Peak Load (N)	1Y	3152 (485)	2573 (437)	2926 (185)	-	1986 (158)
	1.5Y	2719 (605)	2240 (307)	2515 (402)	2140 (310)	1369 (268)
	2Y	3058 (150)	2205 (88)	2450 (295)	2216 (104)	1662 (458)
Elastic Modulus (kN/mm)	1Y	289 (151)	199 (65)	204 (108)	-	128 (49)
	1.5Y	234 (67)	77 (20)	120 (37)	89 (29)	88 (35)
	2Y	216 (102)	184 (65)	120 (51)	133 (26)	91 (18)
Specific Fracture Energy (N/m)	1Y	44.6 (8.1)	44.5 (7.0)	54.9 (6.8)	-	35.6 (2.5)
	1.5Y	43.7 (9.5)	42.8 (5.9)	48.9 (7.8)	40.5 (6.4)	26.9 (6.2)
	2Y	51.6 (5.4)	42.8 (3.2)	46.8 (4.4)	41.4 (2.9)	30.4 (8.6)

Note: The 45D specimens were not tested at 1Y. Average values of each property are listed with standard deviation in parentheses.

Figure 3.9: Evidence of horizontal crack propagation in the 00D1Y specimen with crack outlined below notch tip.

For all curing times, the control specimens had a higher peak load and pseudo-elastic modulus than the ASR-affected specimens. The control specimens had an equal or higher specific fracture energy than most of the ASR-affected specimens. However, for two age denominations, the 00D specimens had a higher average specific fracture energy than the control specimens. The 90D specimens had the lowest peak load, pseudo-elastic modulus, and fracture energy of all specimens.

3.3.3 Crack pattern

In almost all cases, the main crack opened below the notch and propagated almost vertically throughout the specimen, as expected for this type of experiment. The ASR-affected specimens exhibited through-aggregate cracking, particularly for the 90D specimens. The specimens at 2Y showed crack branching and joining along the primary crack path.

Some 00D specimens for the 1Y curing time showed a horizontal crack propagating shortly after the tip of the notch to one side of the specimen, which is in the same direction as the expected ASR-induced micro-cracking (see Figure 3.9). Results from these specimens were not included in the data analysis. This behavior was not observed for the subsequent curing times.

3.3.4 Petrographic analysis

The petrographic analysis was performed on four companion standard 15 cm × 30 cm concrete cylinders normally used for the characterization of engineering properties; the cylinders were cured and stored in exactly the same condition as the WST specimens. Analysis was performed one time on concrete cylinders that were confined and unconfined at a concrete age of approximately 1.5 years. Lapped sections and thin sections were prepared by cutting the cylinders horizontally and vertically. No significant difference was observed with the orientation of the cutting direction.

The evidence of ASR primarily manifested in the form of cracking in coarse aggregate particles with or without gel and in cement paste with or without gel. Reaction rims and gel-coated voids were also detected. The cracks in the coarse aggregate were typically along the edge of the aggregate particles, although instances of ASR-rim formation were found (Figs. 3.10a and 3.10d). Although these cracks were mostly empty with no in-filling of alkali-silica gel, and in many cases they terminated within the aggregate, theses cracks were due to ASR and were not from crushing of the aggregate. When the cracks extended into the paste, they typically branched out and were gel filled, but the majority of the cracks in the aggregate were still empty (Figs. 3.10b and 3.10e). The paste contained moderately abundant random microcracks, with or without gel (Fig. 3.10b). Some microcracks were developed along the aggregate/paste interface (Fig. 3.10f). Most cracks could be traced to reactive argillite particles or a section of the crack that was filled with gel (Fig. 3.10c). The microcracks in the samples were up to ≈76 mm long and ≈0.6 mm wide.

While the sand was initially characterized as nonreactive per ASTM C1260 testing, fine aggregate particles sporadically exhibited evidence of ASR, such as cracking and reaction rims.

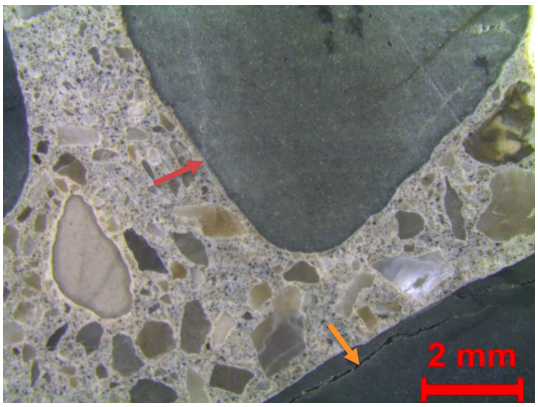

(a) Reaction rim and cracking

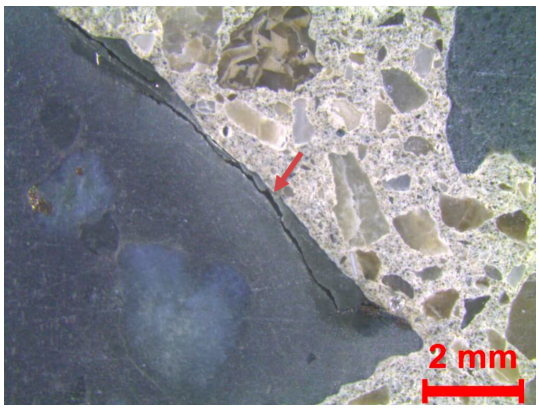

(d) Edge crack without gel.

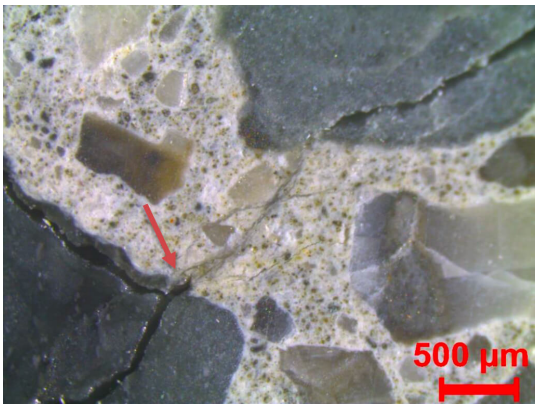

(b) Crack in aggregate and cement

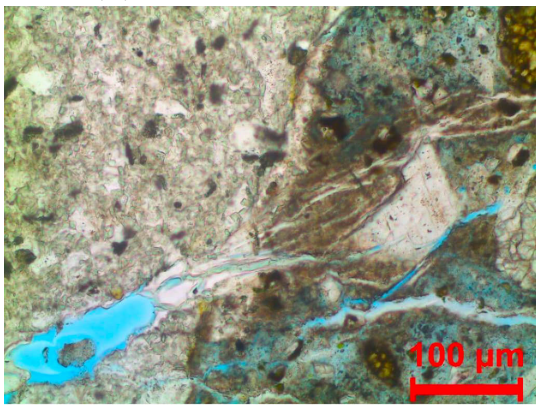

(e) Empty crack in aggregate.

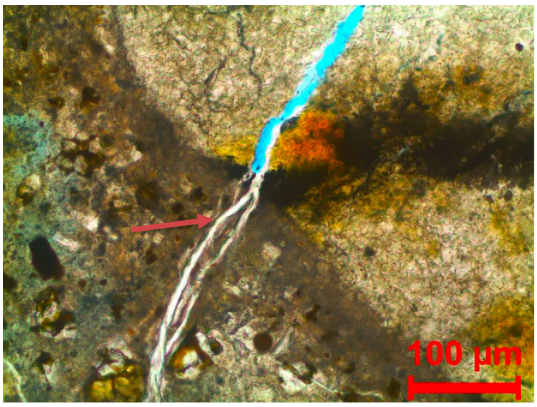

(c) Crack in aggregate and cement

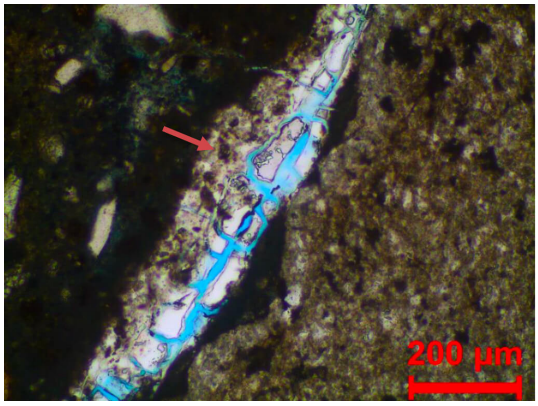

(f) Gel-filled crack at interface

Figure 3.10: Petrographic analysis. (a) Lapped section showing an argillite with reaction rim (red arrow) and another one with edge cracking (orange arrow). (b) Lapped section showing cracks branching out from aggregate to paste and filled with gel (arrow). (c) A thin section image showing cracks filled with gel (white) extending from a nearly empty crack in an argillite aggregate (arrow). (d) Lapped section showing an argillite coarse aggregate particle with an edge crack with no gel (arrow). (e) A thin section image showing a crack in an argillite that was mostly empty (blue on the left) branching into multiple fine cracks in the paste and filled with gel (white). (f) A thin section image showing a gel-filled crack between paste on the left and an aggregate particle on the right (arrow).

3.4 Discussion

3.4.1 Uncertainties

For a given set of specimens corresponding to a given test time and cut orientation, the WST properties derived from the $F_h - \delta$ curves exhibit relatively large variations compared to similar tests previously published in the open literature (e.g., 3-points bending tests on notched beams subjected to ASR (Giaccio et al., 2008; Miki and Tsukahara, 2016)).

Several sources of uncertainties have been identified. (1) With the cast concrete WST specimens being prepared alongside three large, structural blocks of about 10 m^3 each and hundreds of materials and testing cylinders, it was not possible to cast these specimens from the same concrete batch. Hence, possible variations of the water-to-cement ratio, estimated between 0.46 and 0.52, may have occurred. This variation of water-cement ratio likely increased the standard deviation of test results. (2) Visual observation of the cast specimens showed instances of poor concrete consolidation, although the specimens were limited in size. Test results from the small amount of specimens with clearly visible major defects were excluded from data analysis. (3) One instance of misalignment of the metal plate forming the notch in the cast specimens was observed. The removal of the metal plate may have resulted in the formation of pre-existing cracks. The few test specimens with far below average results and indications of pre-existing non-ASR damage were excluded from the data analysis. (4) Dimensional uncertainties resulting from the sawing process of the cut specimens are estimated to be around ± 5 mm. In one specimen, the bottom of the notch was not levelled. (5) Because of the cutting process, the tip of the notch can be located either inside or outside coarse aggregates which causes different modes of fracture initiations from one specimen to another. When the notch tip was located inside an aggregate on the surface, the visible failure path may not have been indicative of the true failure path within the interior. The few instances in which the failure path appeared as in Figure 3.9 occurred in the cement paste below the notch tip. (6) While the loading rate was kept constant for each test, the exact pre-loading value of the WST specimens (before starting data acquisition) was not monitored but was estimated at < 200 N, i.e., $<\approx 5\%$ of the peak load. (7) No sensor drift was observed.

3.4.2 Effect of Alkali-Silica Reaction

The mechanical properties (peak load, pseudo-elastic modulus, specific fracture energy) of most ASR-affected specimens were found to be lower than the properties of the control specimens. However, the fracture energy seemed to increase in the presence of ASR-induced micro-cracking perpendicular to the notch. The force-displacement curves for the ASR-affected specimens showed a much lower rate of post-peak force degradation than the control specimens, indicating a difference in failure mechanism, particularly during the crack initiation period. This is probably due to the existence of a pre-existing network of micro-cracks in the ASR-affected specimens. Indeed, in a control specimen, only the main crack at the tip of the notch is activated but in an ASR-affected specimen, multiple micro-cracks might be simultaneously activated, especially when the micro-cracks are randomly oriented or not aligned with the direction of the principal crack. This could increase the crack surface area and therefore the specific fracture energy as shown for the specimens with expected micro-cracking primarily perpendicular to the notch. This effect can be observed by comparing the CMOD, δ, measured at the tip of the notch to the vertical stroke, labelled Δ in Figure 3.1b, of the loading frame, as shown in Figure 3.11. In the post-peak regime, the δ seems to follow a linear relationship with the Δ, as previously observed by Denarie Denarié (2000). The slope of the linear branch is much steeper for the control specimens than for the ASR-affected specimen, which could indicate that cracking is more distributed in the ASR-affected specimens than in the control specimens. Instrumenting a WST specimen with acoustic sensors such as in Denarie Denarié et al. (2001) could indicate the influence of ASR on the width of the fracture process zone.

The petrographic analysis showed the formation of substantially wide cracks localized either at the edge of the coarse reactive argillite aggregate or through the aggregate extending into the cement paste. This type of crack pattern appears to be characteristic of a fast reaction–induced expansion, with localized cracks likely to cause external loading-induced fracture propagation meandering through the material as observed or inferred by other research works (Miki and Tsukahara, 2016; Giaccio et al., 2008).

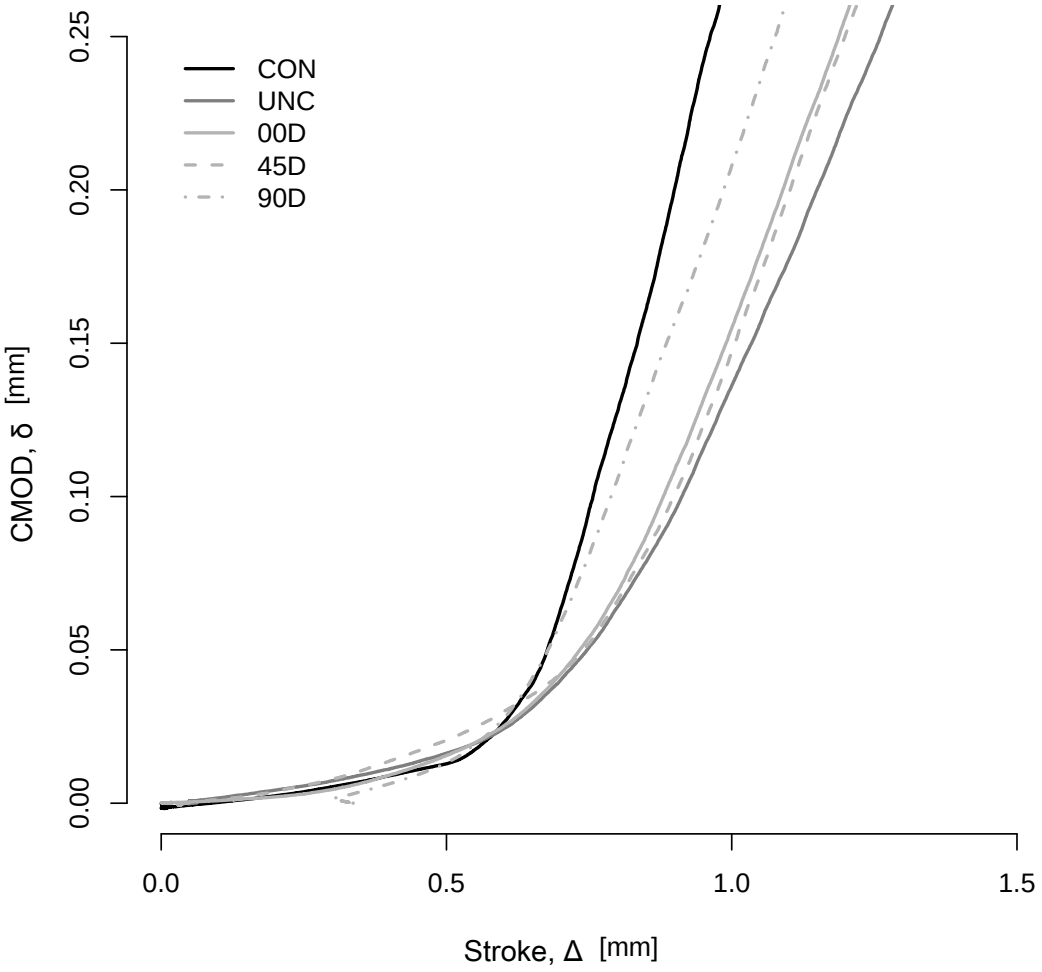

Figure 3.11: Typical CMOD, δ vs. vertical stroke, Δ of the loading frame for the 1.5Y specimens. The 90D curve has been shifted so that the inflection point lies within the same region.

3.4.3 Effect of micro-cracking orientation

The orientation of the ASR-induced micro-cracking seems to play a critical role in the WST crack propagation. Indeed, the 90D specimens (micro-cracking parallel to the notch) show much lower mechanical properties than the other specimens, as the main crack can propagate by connecting to the existing micro-cracks. The strength and fracture energy in particular are consistently lower than in the other ASR-affected specimens, while the properties for the 00D and 45D specimens are within the same range as the unconfined ASR specimen (UNC).

Some 00D specimens (micro-cracking perpendicular to the notch) for a curing time of 1Y showed a much different crack path as what would be expected for this type of experiment, with a main crack propagating perpendicularly to the notch. Interestingly, the 00D specimens for the later curing times did not show the same type of crack propagation. This could be explained by a shift in the ASR-induced cracking:

- During the initial stages of the expansion after the passive confinement has already been initiated, the ASR-induced micro-cracking is primarily oriented in the direction of mechanical restraints.
- In the later stages with more damaged concrete, the micro-cracking becomes denser and starts to branch out in different directions.

Such a shift in the cracking pattern has been observed on the surface of the large blocks tested by Hayes et al. (2018). The surface cracks for the unconfined block are shown in Figure 3.12 after 250 and 694 days of curing, thus approximately corresponding to the 1Y and 2Y curing time. The first visible cracks are mostly horizontal, which corresponds to the reinforcement layout in these blocks. Later, the visible cracks branch out in different directions, creating a map cracking pattern typical of ASR-affected structures. A denser, less oriented micro-cracking pattern would explain why the crack propagates vertically in the 00D specimens for the 1.5Y and 2Y cracking time.

No visible surface cracking was observed on the reactive specimens prior to testing, whether the specimens were cast or cut, which matches with observations from cylinders cast with the same concrete and stored in the same environment (Hayes et al., 2018). This hypothesis could be tested using mesoscale models such as the one developed in previous

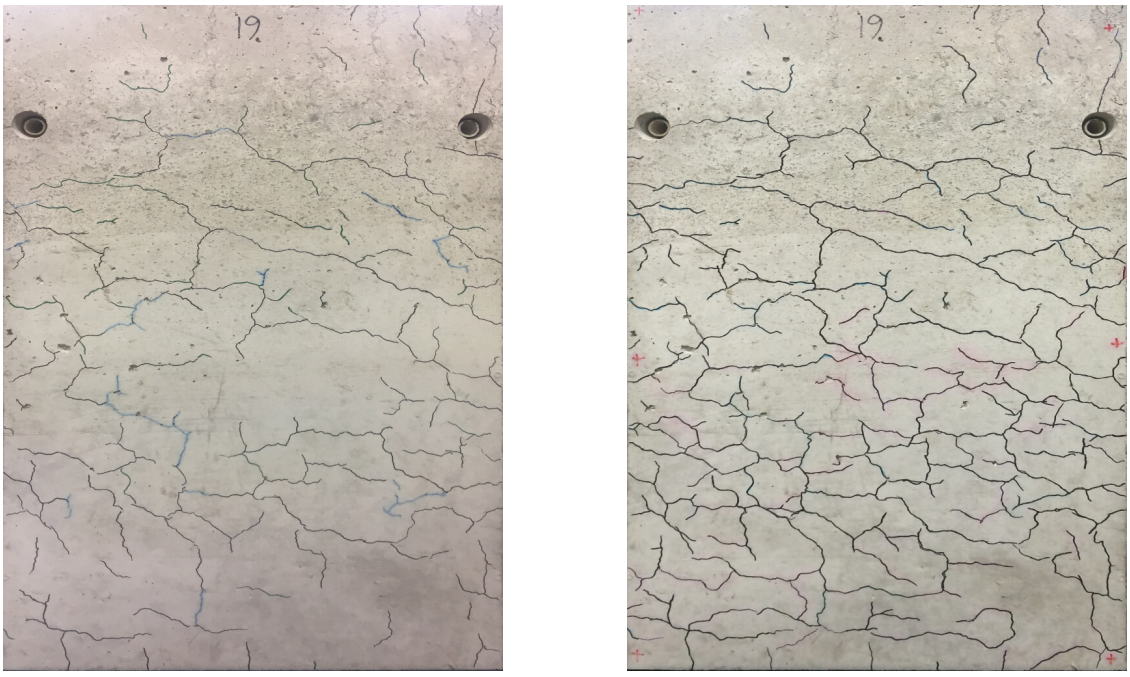

Figure 3.12: Comparison of early crack formations and later stages of cracking on the side of a large companion block.

efforts (Dunant and Scrivener, 2010; Alnaggar et al., 2013; Charpin and Ehrlacher, 2014; Giorla et al., 2015; Esposito and Hendriks, 2016; Ramos et al., 2018) in which the fracture propagation caused by ASR can be obtained in the specimen as a function of the advancement of the reaction and mechanical restraints.

3.4.4 Consequences for numerical models

The experimental results presented here can provide valuable information for the development of structural models for ASR-affected concrete.

The first consequence is that the loss of mechanical properties induced by ASR cannot be represented with a single parameter such as a scalar damage variable or by simply reducing the elastic modulus of the material with the progress of the reaction as in some models Farage et al. (2004); Saouma and Perotti (2006). In this case, the fracture properties of the material would not vary with the orientation of the mechanical load with respect to the ASR-induced micro-cracking which does not conform with the results of this study.

The second consequence is that while the strength of the material decreases with ASR, for a certain preferred ASR-induced crack orientation, the fracture energy seems to increase in the presence of ASR for perpendicular loading direction and ASR micro-cracking orientation. In the orthotropic damage model (Capra and Sellier, 2003; Grimal et al., 2010; Morenon et al., 2017), the damage in each direction is considered as the maximum of the mechanical damage and the ASR-induced micro-mechanical damage, and the shape of the post-peak behavior of the material is not affected by ASR. In this case, the fracture energy of an ASR-affected specimen would always be lower than a pristine specimen, which contradicts the experimental observations from the current study. However, it is likely that these models reproduce the general trend that the tensile strength and fracture energy of ASR-affected concrete in confined conditions are lower when measured in the direction of the mechanical confinement than when measured in a perpendicular direction.

3.5 Conclusion

In this study, the tensile splitting strength and fracture energy of control and ASR-affected specimens were measured using the WST. Some of the ASR-affected specimens were prepared so that the internal micro-cracking was oriented parallel, perpendicular, or at 45 degrees in relation to the notch.

The reactive specimens showed a lower strength but, in some instances, a higher fracture energy than the control specimens. The lowest strength and fracture energy was obtained for the micro-cracking parallel to the notch. For some specimens with the cracks oriented perpendicular to the notch, the main crack propagated alongside that direction instead of in the direction of the applied splitting force. Since this behavior was only observed for the earliest curing time, it could indicate that the micro-cracking induced during the later stages of the ASR expansion was less oriented than during the earlier stages.

These experiments highlight the need of anisotropic damage for structural models for concrete. In addition, mesoscale numerical models could be used to identify the evolution of the internal micro-cracking with the degree of restraint.

Chapter 4

Modeling of Alkali-Silica Reaction in Confined Reinforced Concrete

4.1 Introduction

Alkali-silica reaction (ASR) is a deleterious chemical reaction between alkali hydroxyl ions and types of silica found in some aggregates of concrete. The reaction produces a hygroscopic gel within concrete structures that expands leading to cracking and large deformations. This degradation mechanism is often reported for transportation infrastructures and hydropower-generating stations. However, a few instances of ASR were recently discovered in critical concrete structures in nuclear power plants (NPPs) in Canada, Japan, and the United States (Takatura et al., 2005; Shimizu et al., 2005; Tcherner and Aziz, 2009; U.S. Nuclear Regulatory Commission, 2011; NextEra Energy Seabrook, 2013). NPP concrete structural members were commonly designed as enclosures for the reactor vessel (i.e. containment structures) with thicknesses ranging from 0.6 to 1.5 m. Due to these large thicknesses, the absence of shear reinforcement (in the direction of the wall thickness) was common as permitted by versions of American Concrete Institute (ACI) 318, "Building Code Requirements for Reinforced Concrete", at the time of construction. The reinforcement layout and boundary conditions attributed to a NPP containment structure generate confinement that induces a preferred direction of expansion in the unreinforced, unconfined direction (Multon and Toutlemonde, 2006; Gautam et al., 2017; Hayes et al., 2018). The restraint due to reinforcement and

boundary conditions cause ASR-expansion to develop anisotropically dependent on the stress state.

Owners and regulators of NPPs aim to ensure the safety of the concrete structures with optimal maintenance strategies. A predictive tool capable of realistically estimating the effects of ASR in NPP structures would be invaluable in determining courses of action for continued operation and maintenance of NPPs. Many researchers have developed models to predict the long-term behavior of ASR-affected structures (Baghdadi et al., 2007; Comi et al., 2009; Grimal et al., 2010; Léger et al., 1996; Saouma and Perotti, 2006). However, these models have been used primarily to predict the behavior of dams affected by ASR. Recently, some of these models were used to predict the behavior of NPP reinforced concrete structures (Saouma et al., 2016). However, results from simulations were inconclusive concerning the effect of alkali-silica reaction on the residual material properties of elements taken from a typical NPP structure.

The prediction of the behavior of ASR-affected NPP structures is important for owners and regulators in determining the course of action required for maintaining structural integrity. A model capable of accurately predicting the expansion due to ASR of reinforced concrete structures is necessary for predicting the behavior of such structures.

A new model was developed for predicting the expansion of concrete structures affected by alkali-silica reaction. The model includes a novel combination of existing models as a alkali-silica reaction advancement model, a casting direction anisotropic expansion model, a stress-dependent anisotropic expansion model, and a material property evolution model dependent on the degree of ASR expansion. The model parameters were calibrated based on existing literature data and data generated by previous efforts of this study. The calibrated model was then validated with the experiments described by Hayes et al. (2018) or Chapter 2 of this dissertation.

4.2 Model Descriptions

A new model was developed for predicting the expansion of concrete structures affected by alkali-silica reaction. The new model is summarized by Equation 4.1:

$$\sigma = (1 - D)\ X^{E_c}(\varepsilon^{asr})\ C^0 : \left(\varepsilon - \varepsilon^{asr} - \varepsilon^{th}\right) \tag{4.1}$$

where σ is the total stress, D is the mechanical damage, $X^{E_c}(\varepsilon^{asr})$ is the relative material property coefficient depending on the ASR expansion, C^0 is the initial stiffness matrix of the concrete, ε is the total strain, ε^{asr} is the ASR-induced strain, and ε^{th} is the thermal strain. Concrete creep and shrinkage were not implemented into the current model.

The ASR-induced strain (expansion) is summarized by Equation 4.2:

$$\varepsilon^{asr} = \beta(\sigma)\ \gamma\ \Phi_r\ A(t, T, S_l) \tag{4.2}$$

$\beta(\sigma)$ is the coefficient of stress-dependency. The coefficient of stress-dependency increases or decreases ASR expansion in each direction depending on the state of stress. γ is the coefficient of casting direction anisotropy which accounts for the inherent anisotropic expansion due to casting direction associated with ASR. Φ_r is the maximum expansion of the concrete. $A(t, T, S_l)$ is the reaction advancement model which is a function of the time t, the concrete temperature T, and concrete saturation degree S_l.

4.2.1 Reaction Advancement

Expansion due to ASR was predicted using models supported by previous research. Equation 4.3 gives the base ASR-expansion due to reaction advancement, ε_r:

$$\varepsilon_r(t) = \Phi_r\ A(t) \tag{4.3}$$

where Φ_r is the maximum expansion of a specific concrete due to ASR determined by experimental testing originally introduced by (Larive, 1997). $A(t)$ is the chemical advancement of ASR (increasing from 0 when ASR starts to 1 when ASR is complete). Equation 4.4 gives the rate of chemical advancement, $A(t)$, inspired by works from Larive (1997), Poyet (2003), and Grimal et al. (2010):

$$\frac{\delta A(t)}{\delta t} = \exp\left(-\frac{E_a}{R}\left(\frac{1}{T}-\frac{1}{T_0}\right)\right)\left(\left\langle\frac{S_l - S_{l0}}{1-S_{l0}}\right\rangle_+\right)(S_l - A(t))\left(\frac{1}{\tau_c}\right)\frac{A(t)+\exp\left(-\frac{\tau_l}{\tau_c}\right)}{1+\exp\left(-\frac{\tau_l}{\tau_c}\right)} \tag{4.4}$$

where E_a is the activation energy of ASR, R is the gas constant, T is the temperature in the concrete, T_0 is the absolute temperature of the test in which τ_l, τ_c, and Φ_r are determined. S_l and S_{l0} are the current saturation degree in concrete and required degree of saturation for ASR, respectively. τ_l and τ_c are latency time and characteristic time, respectively, determined by curve fitting of experimental ASR expansion data for a specific concrete mixture originally proposed by Larive (1997). The latency time, τ_l, controls the time delay of the expansion due to ASR. The characteristic time, τ_c, controls the rate of expansion due to ASR. $\langle x\rangle_+$ is the function equivalent to $(x+|x|)/2$ or $\max(0,x)$ in which the result is always zero or positive. The rate of chemical advancement model is a novel combination of several existing models proposed by Larive (1997), Poyet (2003), and Grimal et al. (2010).

4.2.2 Casting Direction Anisotropy

ASR expansion has been shown to be anisotropic dependent on the direction relative to the casting direction (Jones and Clark, 1996; Larive, 1997; Smaoui et al., 2004). For free-expanding concrete specimens, the expansion due to ASR is largest in the axis parallel to the line of action of gravity at the time of concrete placement. Expansion has been shown to be 1 to 2.5 times larger in the axis parallel to the line of action of gravity when compared to axes perpendicular to gravity. Larive (1997) observed a thicker film of water under aggregate particles along the casting plane which could have caused more porous and weaker aggregate/paste interfaces. Smaoui et al. (2004) hypothesized that the casting direction anisotropy can be attributed to this observation as the weaker aggregate/paste interfaces in the casting plane decrease the resistance of concrete to the ASR expansive forces and the collection of water under the aggregates in the casting plane may cause a concentration

of reactive particles. However, this variation of expansion relative to casting direction is dependent on the concrete mixture and not yet fully understood.

A new model was developed to account for the casting direction anisotropy associated with ASR expansion. The casting direction effect was incorporated into the model using a coefficient of casting direction anisotropy, γ, to scale expansion dependent on the direction relative to the line of action of gravity during concrete placement. Equation 4.5 gives the modification of base ASR expansion to take casting direction anisotropy into account:

$$\varepsilon_{ii}^{cdr} = \gamma_i \, \varepsilon_r \tag{4.5}$$

where ε^{cdr} is the adjusted ASR expansion accounting for casting direction anisotropy, and ε_r is the base ASR expansion given by Equation 4.3. γ is the coefficient for casting direction anisotropy, specific for each primary axis. γ must be determined by experimental testing of ASR expansion of plain concrete measured in at least two primary axes (the axis parallel to the line of action of gravity during concrete placement and a perpendicular direction). The coefficient of casting direction anisotropy for the axis parallel to gravity can be determined by dividing expansion data in the axis parallel to gravity at the time of concrete placement by the expansion data in any axis perpendicular. If the coefficient of casting direction anisotropy for the axes perpendicular to gravity at the time of concrete placement is taken as $\gamma_\perp = 1$, the coefficient of casting direction for the axis parallel to gravity may range from $\gamma_\parallel = 1$ to 2.5 depending on the concrete mixture.

4.2.3 Stress-Dependent Anisotropic Expansion

ASR expansion has been shown to be anisotropic dependent on applied stresses or generated stresses due to confinement such as boundary conditions or steel reinforcement (Larive, 1997; Multon and Toutlemonde, 2006; Gautam et al., 2017; Hayes et al., 2018). ASR expansion is largest in the direction with the least stress and smallest in the directions with the most stress.

A new model was developed to account for the stress-dependency of ASR expansion. The stress-dependent anisotropy was incorporated into the model by calculating a coefficient of

stress-dependency, β, for each primary axis. The coefficient of stress-dependency, β, is used to modify the expansion in each primary axis as shown in Equation 4.6:

$$\varepsilon_{ii}^{asr} = \beta_i \, \varepsilon_{ii}^{cdr} \tag{4.6}$$

where ε_{ii}^{asr} is the final ASR expansion accounting for casting direction anisotropy and stress-dependency and ε_{ii}^{cdr} is the adjusted ASR expansion accounting for casting direction anisotropy given by Equation 4.5. The value of the coefficient of stress-dependency, β, must always be zero or positive. As compressive stress increases in a particular direction, subsequent ASR expansion will decrease or become zero. The value of β can be larger than one leading to an increase in ASR expansion particularly for directions under tensile stress or zero stress when other directions are under compression.

The coefficient of stress-dependency, β, is determined for each primary axis as a function of the spherical and deviatoric stresses. It is important to note that compression is indicated by a negative stress and tension is indicated by a positive stress for this model. The spherical stress is determined as one-third of the trace of the stress tensor as shown in Equation 4.7. The deviatoric stress for each primary axis is determined as the stress in that primary axis subtracted by the spherical stress as shown in Equation 4.8.

$$\sigma_{sph} = \frac{1}{3}\mathrm{tr}(\boldsymbol{\sigma}) \tag{4.7}$$

$$\sigma_{ii}^{dev} = \sigma_{ii} - \sigma_{sph} \tag{4.8}$$

The coefficient of stress-dependency is divided into three portions: a spherical portion depending on the spherical stress, a first deviatoric portion depending on the deviatoric stress in the primary axis of interest, and a second deviatoric portion depending on the deviatoric stresses in the other two primary axes. The coefficient of stress-dependency for the direction of each primary axis is determined by the summation of the spherical portion, first deviatoric portion, and second deviatoric portion as shown in Equation 4.9:

$$\beta_i = \beta_{sph} + \beta_i^{dev_i} + \beta_i^{dev_{jk}} \tag{4.9}$$

where β_{sph} is the spherical portion of the coefficient, $\beta_i^{dev_i}$ is the first deviatoric portion of the coefficient, and $\beta_i^{dev_{jk}}$ is the second deviatoric portion of the coefficient.

Each portion of the coefficient of stress-dependency is calculated by an empirical function depending on the spherical or deviatoric stresses. The shape of the function was selected such that, for decreasing stress below zero (increasing compressive stress), the portion of the coefficient of stress-dependency will decrease and eventually plateau at a value of zero, eliminating all expansion. Conversely, for increasing stress above zero (increasing tensile stress), the portion of the coefficient of stress-dependency will increase and eventually plateau at a certain value, increasing expansion up to a degree. The spherical portion of the coefficient of stress-dependency is given by Equation 4.10:

$$\langle \beta_{sph} \rangle_+ = X + \alpha \left(\frac{1 - \exp\left(\frac{-(\sigma_{sph} - \sigma_{03}^{sph})}{\sigma_{01}^{sph}} \right)}{1 + \exp\left(\frac{-(\sigma_{sph} - \sigma_{03}^{sph})}{\sigma_{01}^{sph}} + \frac{\sigma_{02}^{sph}}{\sigma_{01}^{sph}} \right)} \right) \tag{4.10}$$

where σ_{sph} is the spherical stress determined by Equation 4.7. X and α are parameters calibrated for all functions for portions of the coefficient of stress-dependency. σ_{01}^{sph}, σ_{02}^{sph}, and σ_{03}^{sph} are parameters calibrated specifically for the spherical portion of the coefficient of stress-dependency. $\langle x \rangle_+$ is the function equivalent to $(x + |x|)/2$ in which the result is always zero or positive.

The first deviatoric portion of the coefficient of stress-dependency is given by Equation 4.11:

$$\langle \beta_i^{dev_i} \rangle_+ = X + \alpha \left(\frac{1 - \exp\left(\frac{-(\sigma_{ii}^{dev} - \sigma_{03}^{dev_i})}{\sigma_{01}^{dev_i}} \right)}{1 + \exp\left(\frac{-(\sigma_{ii}^{dev} - \sigma_{03}^{dev_i})}{\sigma_{01}^{dev_i}} + \frac{\sigma_{02}^{dev_i}}{\sigma_{01}^{dev_i}} \right)} \right) \tag{4.11}$$

where σ_{ii}^{dev} is the deviatoric stress for the primary axis in which the coefficient of stress-dependency is being determined, calculated by Equation 4.8. X and α are parameters calibrated for all functions for portions of the coefficient of stress-dependency. $\sigma_{01}^{dev_i}$, $\sigma_{02}^{dev_i}$, and

$\sigma_{03}^{dev_i}$ are parameters calibrated specifically for the first deviatoric portion of the coefficient of stress-dependency.

The second deviatoric portion of the coefficient of stress-dependency is given by Equation 4.12:

$$\langle \beta_i^{dev_{jk}} \rangle_+ = X + \alpha \left(\frac{1 - \exp\left(\frac{-(-(\sigma_{jj}^{dev} + \sigma_{kk}^{dev}) - \sigma_{03}^{dev_{jk}})}{\sigma_{01}^{dev_{jk}}} \right)}{1 + \exp\left(\frac{-(-(\sigma_{jj}^{dev} + \sigma_{kk}^{dev}) - \sigma_{03}^{dev_{jk}})}{\sigma_{01}^{dev_{jk}}} + \frac{\sigma_{02}^{dev_{jk}}}{\sigma_{01}^{dev_{jk}}} \right)} \right) \tag{4.12}$$

where σ_{jj}^{dev} and σ_{kk}^{dev} are the deviatoric stresses for the two other primary axes perpendicular to the axis in which the coefficient of stress-dependency is being determined, calculated by Equation 4.8. X and α are parameters calibrated for all functions for portions of the coefficient of stress-dependency. $\sigma_{01}^{dev_{jk}}$, $\sigma_{02}^{dev_{jk}}$, and $\sigma_{03}^{dev_{jk}}$ are parameters calibrated specifically for the second deviatoric portion of the coefficient of stress-dependency.

4.2.4 Material Property Evolution

ASR-induced expansion has been shown to reduce material properties including compressive strength, elastic modulus and (splitting) tensile strength (Swamy and Al-Asali, 1988a; Larive, 1997; Ben Haha, 2006; Esposito et al., 2016). Compressive strength and splitting tensile strength have been shown to increase at the early stage, later decrease due to ASR, and then recover strength attributed to the continuation of the cement hydration (Swamy and Al-Asali, 1988a).

Some ASR models do not consider the change in compressive or tensile strength and consider only the decrease in elastic modulus due to expansion (Léger et al., 1996; Saouma et al., 2016). Accurately predicting the residual material properties after ASR expansion is important in determining the integrity of a concrete structure.

A new model was developed to predict the change in material properties with increasing ASR expansion. The evolution of material properties was incorporated into the model using a relative material property coefficient, X^N, to adjust the 28-day values of material properties

as a function of the ASR expansion. The variable N changes for each material property: f_c' for compressive strength, E_c for elastic modulus, and f_t' for tensile strength. Equation 4.13 gives the model for material property evolution as a function of ASR expansion:

$$X^N = \left[1 + x_\infty^N \left(1 + \exp\left(\frac{-\varepsilon^{asr}}{\lambda_h}\right)\right)\right] \left[1 - D_{max}\left(1 - \exp\left(\frac{-\varepsilon^{asr}}{\lambda_a}\right)\right)\right] \tag{4.13}$$

where x_∞^N and λ_h are calibrated parameters governing the increase of properties due to cement hydration. x_∞^N has a calibrated value for each material property, N. x_∞^N is the maximum relative value of increase in material property due to cement hydration. λ_h is the rate control parameter for the increase of properties due to cement hydration. D_{max} and λ_a are calibrated parameters governing the decrease of material properties due to ASR expansion. D_{max} is the maximum relative value for decrease in material properties due to ASR expansion. λ_a is the rate control parameter for the decrease of properties due to ASR expansion. ε^{asr} is the ASR expansion calculated by Equation 4.6.

The resulting value of material property is determined by multiplying the relative material property coefficient determined as a function ASR expansion expansion and the initial value of the material property (i.e. the value of material property before ASR expansion has occurred) as shown in Equations 4.14 - 4.16.

$$f_c' = X^{f_c'}\ f_c'(0) \tag{4.14}$$

$$E_c = X^{E_c}\ E_c(0) \tag{4.15}$$

$$f_t' = X^{f_t'}\ f_t'(0) \tag{4.16}$$

4.3 Model Validation

4.3.1 Experiment Description

The model was validated by simulating the experiment presented in Hayes et al. (2018) and Chapter 2 of this dissertation. In this experiment, two large specimens (3.0 m by 3.5 m by 1.0 m) were subjected to ASR expansion. The dimensions and reinforcement layout of these specimens are shown in Figure 2.1. A layout of two elevations of intersecting 35.8 mm diameter steel reinforcing bars spaced at 25.4 cm were placed in the 3.0 by 3.5 m planes of the specimens. A concrete cover of 7.62 cm separated the external faces of the specimens parallel to this plane and nearest elevation of reinforcing bars. The 1.0 m thickness was not reinforced.

One of these specimens was confined by a manufactured steel frame, generating stresses due to ASR expansion in the 3.0 by 3.5 m plane of the specimen. This confinement forced the majority of the ASR expansion to the 1.0 m thickness direction of the specimen. The first specimen, confined by the steel frame, was labelled the confined ASR-reactive specimen (CASR). The second specimen, identical in geometry and reinforcement layout with no confinement, was labelled the unconfined ASR-reactive specimen (UASR).

A third specimen was constructed before the construction of the CASR and UASR specimen. This third specimen, labelled small ASR-reactive specimen (SASR), was used to develop the concrete mixture of the CASR and UASR specimens. The SASR specimen was not reinforced and served as a free ASR-expansion specimen that can be used to calibrate parameters for this study. The dimensions of the SASR specimen were 0.6 m by 0.3 m by 0.3 m.

All three specimens were constructed using a nearly identical concrete mix design as shown in Table 2.2. The CASR and UASR specimens used a manufactured sand from the Knoxville, Tennessee area which was determined to be non-reactive by ASTM C1260. The SASR specimen used a manufactured sand from the Calera, Alabama area which was determined to be non-reactive by ASTM C1260. The SASR specimen was conditioned in an environment of 95% relative humidity and 38 °C for 500 days. The CASR and UASR specimens were conditioned in a similar environment of 95% relative humidity and 38 °C for

the first year. For the second year, the conditioning of the CASR and UASR specimens was lowered to 90% relative humidity and 25 °C. For each specimen, expansion due to ASR was measured in each primary axis of the specimen.

4.3.2 Software and Meshing

The ASR model was implemented in a finite element analysis (FEA) software called Cast3M. Cast3M is a FEA software for use in structural and fluid mechanics (Cast3M, 2019). Cast3M uses a command language, GIBIANE, which consists of standard operators allowing for ease of use. A custom damage model with energetic regularization inspired by models of Mazars (1984); Hillerborg et al. (1976); Feenstra (1993) was used as the mechanical damage model. A custom Cast3M program was developed to allow the Material Property Evolution model to be used in conjunction with the custom mechanical damage model within Cast3M.

The experiment was modeled in three dimensions. Concrete was represented as 8-node cubic elements. Steel reinforcement bars were modeled as bar elements fixed rigidly at each connecting concrete element by interpolation. The steel confinement frame was fully modeled as 8-node cubic elements surrounding the CASR specimen. The concrete and steel confinement frame were joined by elements that allowed sliding in the planes of the surfaces in contact. The fully meshed concrete specimen and steel confinement frame are shown in Figure 4.1

4.3.3 Preliminary Simulations

A 2-dimensional drying analysis of the UASR specimen was conducted prior to implementation of the ASR model in Cast3M. For the exposure conditions of 95% relative humidity and 38 °C during the first year and 90% and 25 °C during the second year, the internal saturation degree at the end of two years was approximately 0.98 at 5 cm below the surface due to the large scale of the specimen. All elements further internal than 5 cm from a surface had a saturation degree higher than 0.98. Based on the results of the analysis and for simplicity, the saturation degree was assumed to be $S_l = 1.00$ for the entire duration of the test for all elements of the concrete specimens.

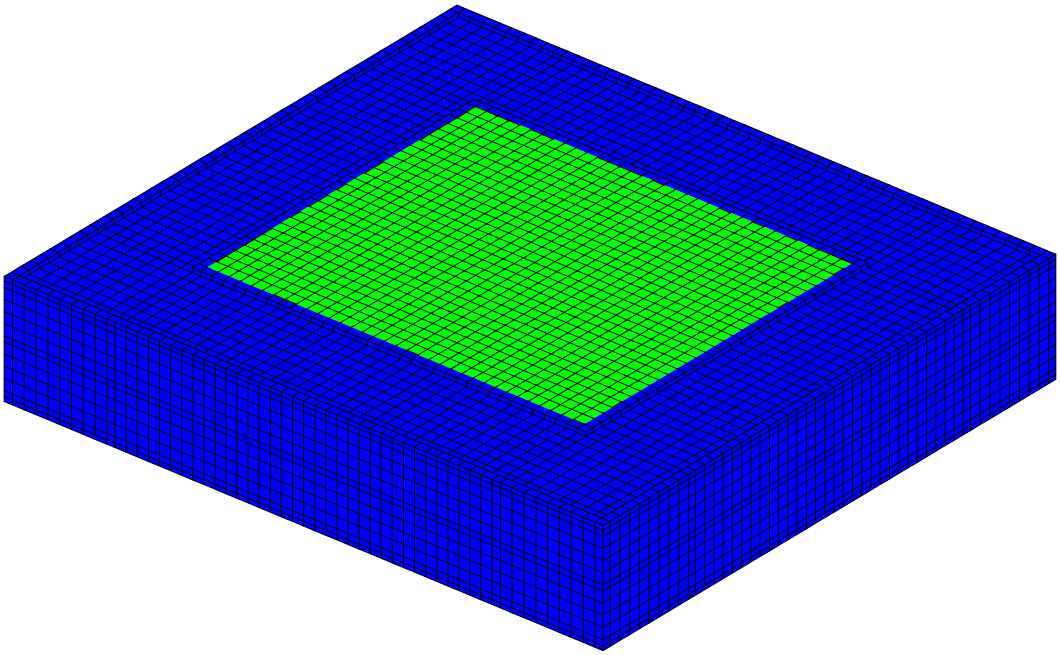

Figure 4.1: Meshed geometry of concrete specimen including reinforcing bars and steel confinement frame

Table 4.1: 28-day values of concrete material properties

Property	Symbol	Value
Compressive Strength	f'_c	21.4 MPa
Elastic Modulus	E_c	34.4 GPa
Tensile Strength	f'_t	2.4 MPa

Table 4.2: Assumed values of steel reinforcing bar material properties

Property	Symbol	Value
Yield Stress	σ_y	483 MPa
Elastic Modulus	E_s	210 GPa
Poisson Ratio	ν_s	0.3

4.3.4 Material Characterization

The concrete material properties were gathered from experimental testing of standard size cylinders (15.2 cm diameter by 30.4 cm height) in accordance with ASTM C39, ASTM C469, and ASTM C496 as described in Hayes et al. (2018) and Chapter 2. The 28-day material properties of concrete cylinders are reported in Table 4.1.

The material properties of the steel reinforcing bars were assumed from typical values for Gr. 60 steel reinforcing bars. The material properties of the steel reinforcing bars are shown in Table 4.2. The steel confinement frame was assumed to remain within the elastic range. Similar values of E_s and ν_s, as reported in Table 4.2, were used as the material properties for the steel confinement frame.

4.3.5 Model Parameter Calibration

Initially, ASR reaction advancement parameters were calibrated to experimental data of the free-swelling smaller ASR-reactive specimen, SASR. τ_c, τ_l, and Φ_r were calibrated to experimental expansion data of the SASR specimen in the direction perpendicular to the line of action of gravity during pouring. Table 4.3 shows the values of calibrated ASR reaction advancement parameters. Figure 4.2 shows the modeled expansion of the SASR specimen with calibrated parameters compared to the experimental data.

The coefficient of casting direction anisotropy, γ (Equation 4.5), was determined by analyzing the experimental data of the free-swelling SASR specimen. Each primary axis of the SASR specimen was labelled similarly to the larger specimens (CASR and UASR) as shown in Figure 2.1. For all specimens, the Z-axis represents the axis parallel to gravity at the time of construction. The X and Y-axes are perpendicular to gravity at the time of construction. The expansion value in the Z-direction for the SASR specimen was divided by the expansion in the X-direction at each value of time for which data was collected. These values were averaged to determine the coefficient of casting direction anisotropy in the Z-direction for the specific concrete mixture. The resulting coefficients of casting direction anisotropy are shown in Table 4.4. Because the ASR reaction advancement parameters were

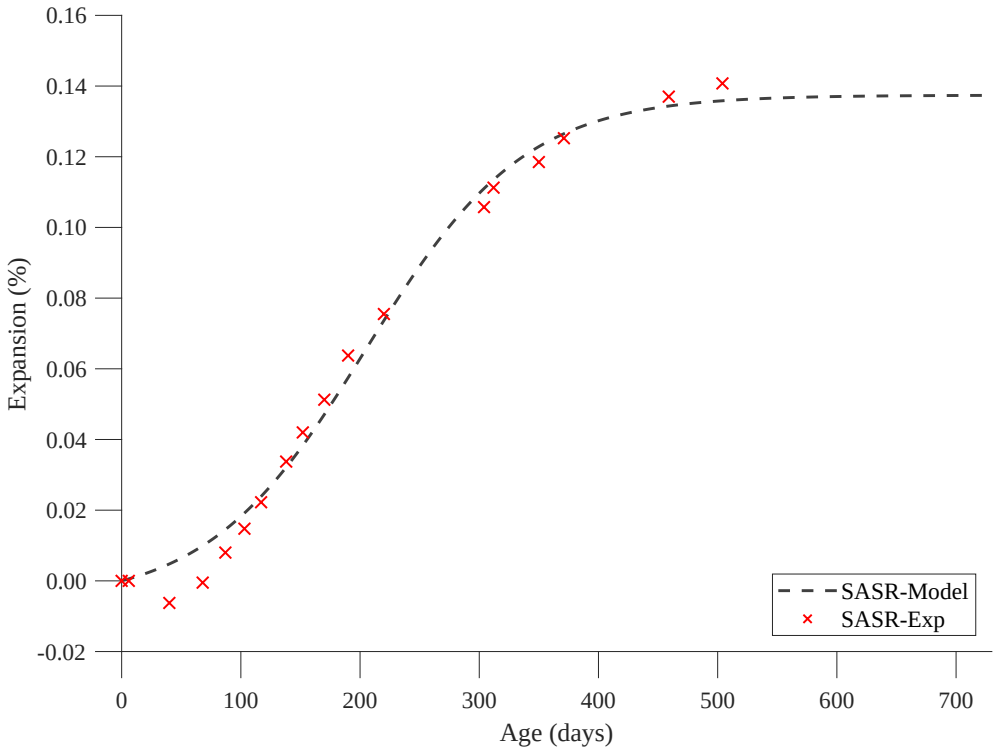

Figure 4.2: Modeled expansion of SASR specimen compared to experimental data

Table 4.3: ASR reaction advancement parameters from curve fitting of SASR specimen

Parameter	Symbol	Value
Characteristic Time	τ_c	66.4 days
Latency Time	τ_l	205.0 days
Maximum Expansion	Φ_r	1374E-6 m/m
ASR Energy Constant	E_a/R	5080 K (Larive, 1997)
Temperature of Test	T_0	311.15 K
Degree of Saturation Threshold	S_{l0}	0.2 (Grimal et al., 2010)

Table 4.4: Coefficients of casting direction anisotropy

Axis	Symbol	Value
X	γ_x	1.0
Y	γ_y	1.0
Z	γ_z	2.1

calibrated to the expansion in the X-axis, the coefficient for casting direction in the X and Y-axes is equal to 1.

The model parameters for the coefficient of stress-dependency, β (Equation 4.9), were calibrated to the experimental data of Gautam (2016). Gautam (2016) tested concrete cubes undergoing ASR-expansion stressed to varying degrees in each axis of the cube. The expansion of the cubes in each direction was measured. The distribution of expansion and corresponding stress state in each direction was used to calibrate the model parameters. The calibrated parameters of the coefficient of stress-dependency model are shown in Table 4.5. The calibrated shapes of the portions of the coefficient of stress-dependency are shown in Figure 4.3.

The parameters for the material property model were calibrated to the experimental data of standard cylinder testing. Compressive strength, elastic modulus, and splitting tensile strengths were calculated as a value relative to the 28-day value and then correlated by testing date to an expansion value gathered from the large specimens. Expansions of cylinders were not directly measured. The parameters of the material property evolution model are shown in Table 4.6. The shapes of relative material property evolution curves with calibrated parameters are shown in Figure 4.4.

4.3.6 Simulated Expansions

The free-expanding SASR specimen expansions were simulated first. The resulting modeled expansions of the free-swelling SASR specimen are shown in Figure 4.5. The error bars represent the experimental minimum and maximum expansion values at each measurement time. The Z-axis of the SASR specimen is the axis parallel to the line of action of gravity at the time of concrete placement. The X-axis is the axis perpendicular to the line of action of gravity at the time of concrete placement. The reaction advancement parameters (Table 4.3) were calibrated to the expansion in the X-axis. Because the SASR specimen was free-swelling, the model governing anisotropy due to stress state is not tested in this comparison. However, this comparison does validate the model governing the anisotropy due to casting direction. The coefficient of casting direction anisotropy increases the Z-direction expansion to values similar to the experimental data.

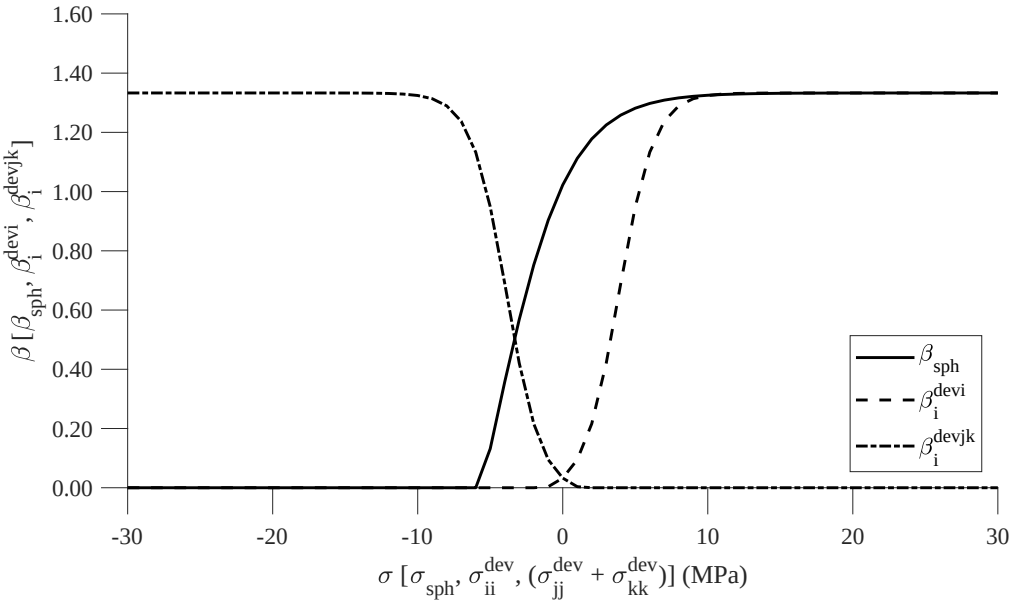

Figure 4.3: Calibrated curves for portions of coefficient of stress dependency, β

Table 4.5: Model parameters for coefficient of stress-dependency, β

Type	**Parameter**				
$N =$	X	α	σ_{01}^N (MPa)	σ_{02}^N (MPa)	σ_{03}^N (MPa)
sph	1/3	1	2.61	-0.84	-4.11
dev_i			1.21	1.26	2.62
dev_{jk}			1.21	1.26	2.62

Table 4.6: Calibrated parameters for material property evolution model

Parameter	Symbol	Value
Scalar for compressive strength	$x_\infty^{f_c'}$	4.001
Scalar for elastic modulus	$x_\infty^{E_c}$	0.657
Scalar for tensile strength	$x_\infty^{f_t'}$	3.194
Hydration constant	λ_h	0.104 %
Scalar for ASR damage	D_{max}	0.707
ASR damage constant	λ_a	0.044 %

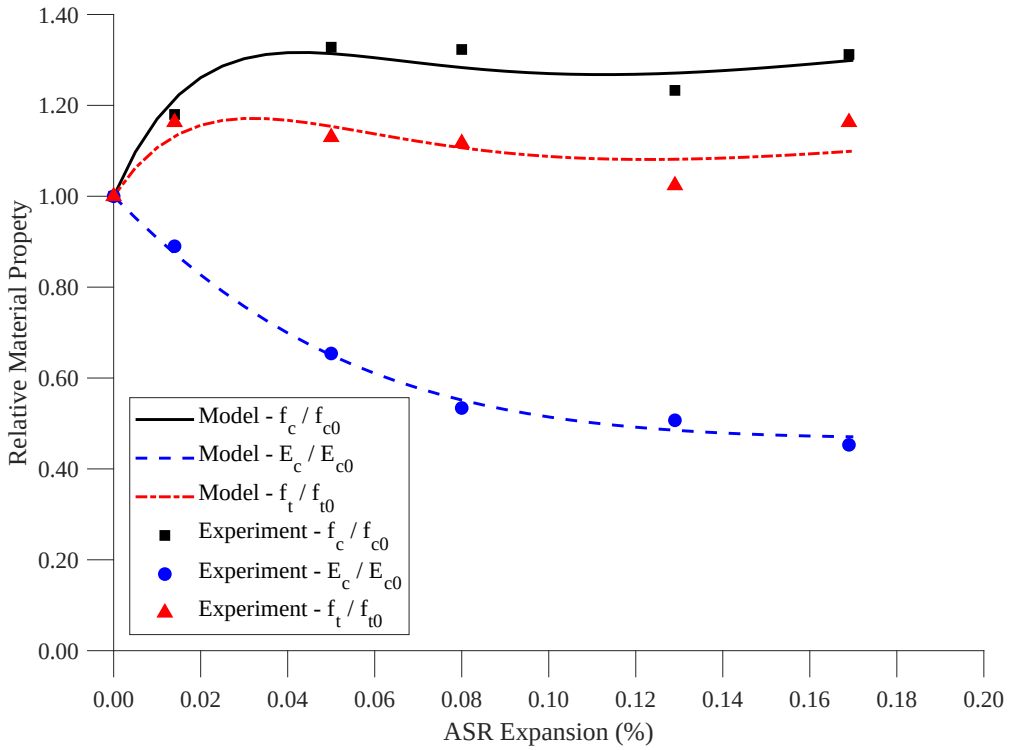

Figure 4.4: Calibrated curves for relative material property evolution

The UASR specimen expansions were simulated using the reaction advancement parameters from the SASR specimen. The resulting modeled expansions of the UASR specimen are shown in Figure 4.6. The error bars represent the experimental minimum and maximum expansion values at each measurement time. The modeled expansion values do not lie within the variation of experimental expansion data.

The differences in the modeled expansions and experimental expansions of the UASR specimen point to a difference in reaction kinetics (reaction advancement). Clearly, the kinetics of the SASR specimen (from which reaction advancement parameters were calibrated) are different than the UASR kinetics despite the two specimens having a similar mix design. The only differences between the UASR and SASR specimens are the specimen sizes and presence of steel reinforcement in the UASR specimen. The presence of steel reinforcement would not alter the total volumetric expansion as the addition of stresses to an ASR-expanding concrete specimen has been shown not to cause a change in volumetric expansion when at least one direction remains unstressed. (Multon and Toutlemonde, 2006;

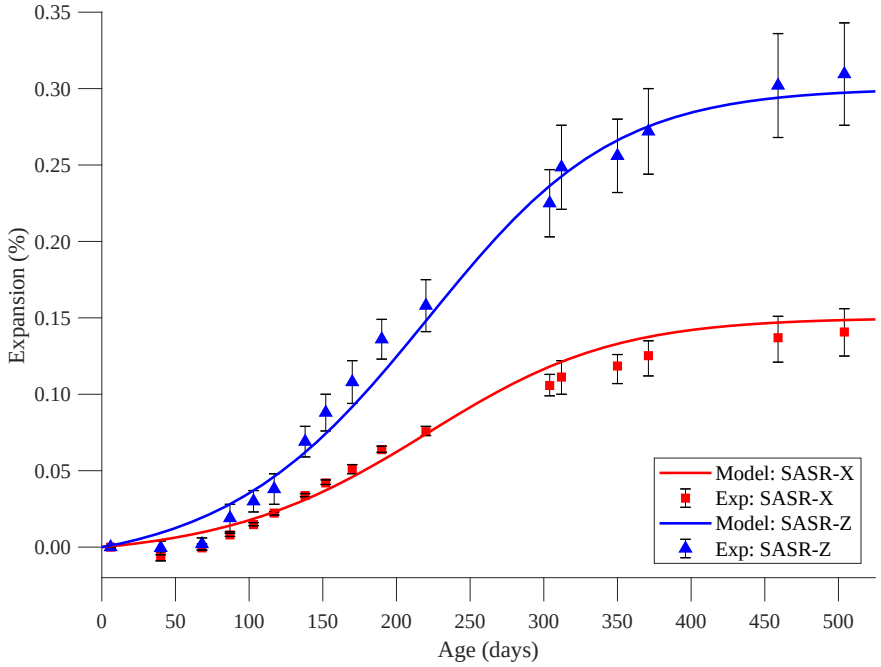

Figure 4.5: Simulated expansions of the SASR specimen

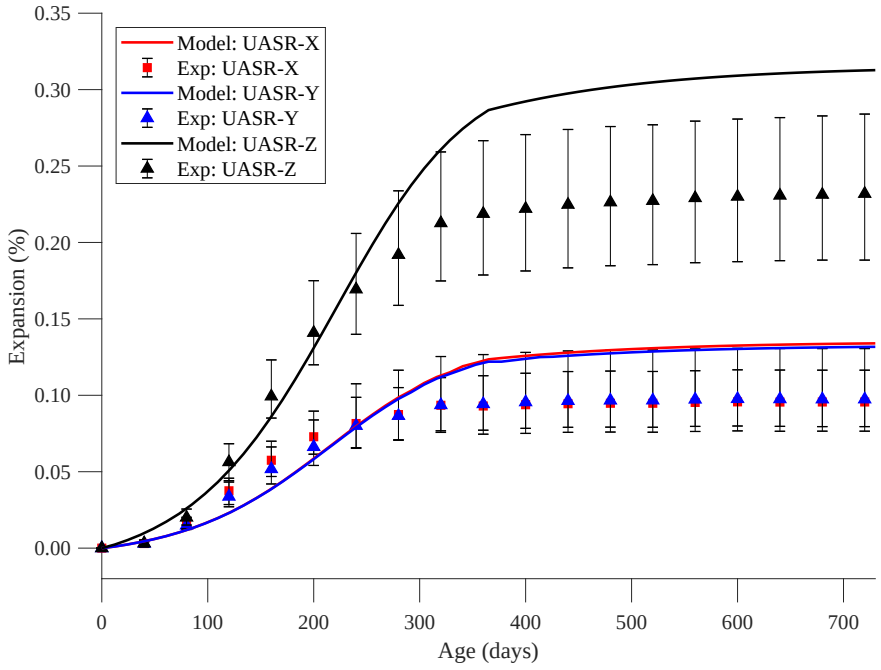

Figure 4.6: Simulated expansions of the UASR specimen using reaction advancement parameters from SASR specimen

Table 4.7: ASR reaction advancement parameters from curve fitting of UASR specimen

Parameter	Symbol	Value
Characteristic Time	τ_c	56.0 days
Latency Time	τ_l	146.3 days
Maximum Expansion	Φ_r	1023E-6 m/m

Gautam, 2016; Hayes et al., 2018). Therefore, difference in kinetics can be attributed to the difference in specimen sizes. The UASR specimen is nearly 200 times the volume of the SASR specimen. Research into the size effect of concrete affected by ASR attributes alkali-leaching as the cause (Lindgård et al., 2013; Multon and Sellier, 2016). A smaller specimen (higher surface-to-volume ratio) is subject to a higher degree of alkali-leaching causing a lower degree of expansion when compared to a larger specimen. Considering the current understanding of size effect due to alkali-leaching, the smaller SASR specimen should have less volumetric expansion when compared to the UASR specimen; however, this is not the case. Expansions of the UASR specimen were over-predicted when the model parameters were calibrated to the kinetics of the SASR specimen. The disagreement between the current understanding of ASR size-effect and the results presented in this study point to the need for more study on this topic, especially for very large concrete specimens.

Because of the difference in ASR kinetics between the SASR and UASR specimens, the reaction advancement parameters were instead calibrated to the experimental results of the UASR specimen. In order to back-calculate the base expansion of the UASR specimen, the experimental volumetric expansion was divided by the sum of coefficients of casting direction anisotropy in all primary directions, $\varepsilon_{vol}^{asr}/(\gamma_x + \gamma_y + \gamma_z)$. The reaction advancement model parameters were calibrated to this resulting expansion curve representing the base ASR expansion perpendicular to gravity. The reaction advancement model parameters calibrated to the UASR experimental expansion are shown in Table 4.7.

The UASR specimen expansions were simulated using the new reaction advancement parameters from the UASR specimen. The resulting modeled expansions of the UASR specimen are shown in Figure 4.7. The error bars represent the experimental minimum and maximum expansion values at each measurement time. The modeled expansion shows better agreement with the experimental data when using the reaction advancement parameters

obtained from curve fitting of the UASR specimen data. The stresses induced by expansion under the restraint of the steel reinforcement reduced the base expansion in the X and Y-directions. The expansion in the Z-direction was correspondingly increased due to the stress-state.

The CASR specimen expansions were simulated using the reaction advancement parameters from the UASR specimen. The full steel confinement frame was modeled in the software surrounding the CASR specimen. The resulting modeled expansions of the CASR specimen are shown in Figure 4.8. The error bars represent the experimental minimum and maximum expansion values at each measurement time. The simulated expansions of the CASR specimen in the X and Z direction lie within the variation of experimental data. The model is capable of generating increased ASR-expansion in the Z-axis (with no restraint) and decreased expansion in the X-axis (with restraint due to reinforcement and steel confinement frame). However, the modeled expansion of the CASR specimen in the Z-direction is consistently lower than the average values of experimental expansion. The simulated results show a similar reduction in the X and Y-direction expansions whereas the experimental data show a larger reduction in expansion for the X-direction when compared to the Y-direction.

The addition of the steel confinement frame reduced modeled expansions in the X and Y-directions by nearly 0.05% and 0.04%, respectively. The Z-direction modeled expansion was correspondingly increased by nearly 0.04% by the addition of the steel confinement frame.

In an actual nuclear containment structure, the casting direction would be parallel to the plane of the wall rather than perpendicular to the plane of the wall as it is in these experiments. To better understand the actual expected expansion of a nuclear containement structure, another simulation was performed in which the casting direction was changed to the X-axis of the specimen with coefficients of casting direction anisotropy of $\gamma_x = 2.1$, $\gamma_y = 1.0$, and $\gamma_z = 1.0$. The denomination, "CASRR", is used to denote the CASR specimen rotated with the casting direction being the X-axis. Figure 4.9 shows the simulated expansions of the CASR specimen rotated such that the casting direction is in the X-axis. As evidenced by the simulation, the casting direction plays a major role in the observed expansions with the CASRR specimen experiencing much less through-thickness Z-direction

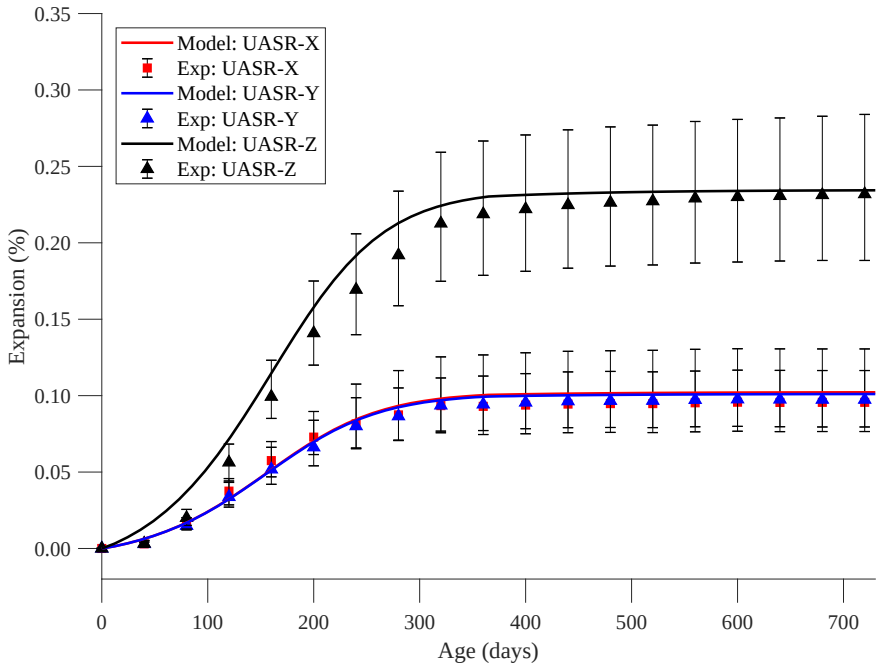

Figure 4.7: Simulated expansions of the UASR specimen using reaction advancement parameters from UASR specimen

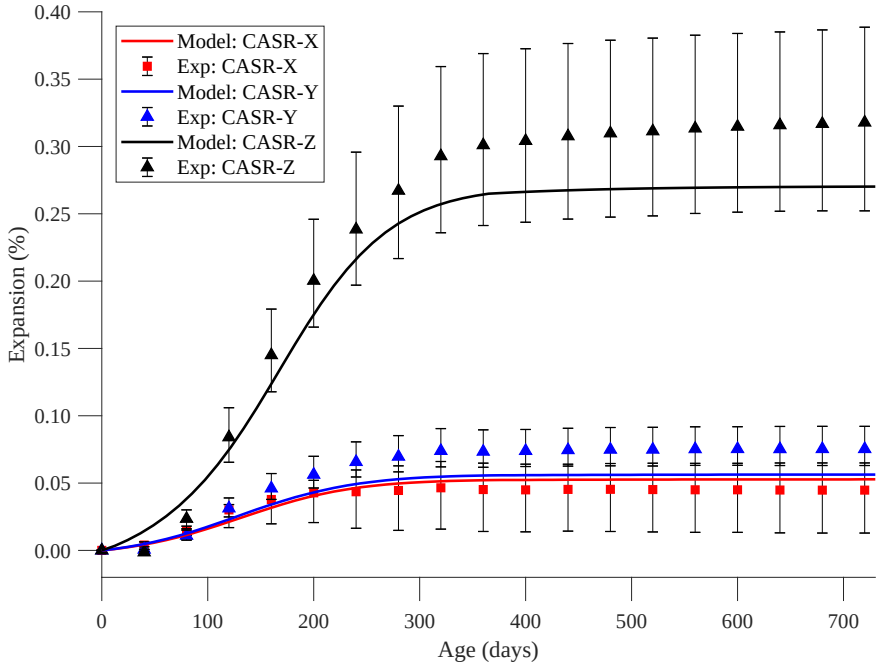

Figure 4.8: Simulated expansions of the CASR specimen using reaction advancement parameters from UASR specimen

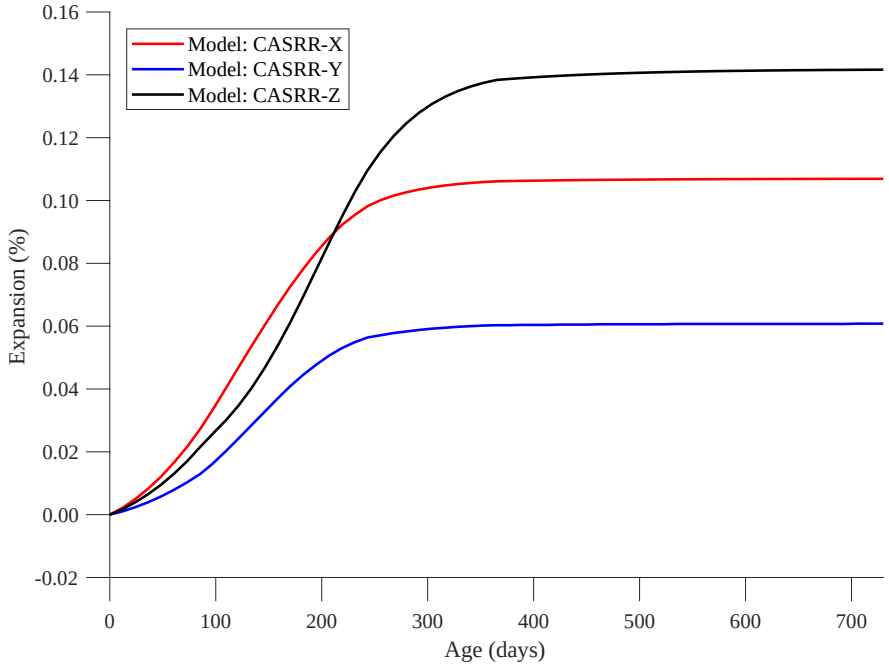

Figure 4.9: Simulated expansions of the rotated CASRR specimen with the casting direction in the X-axis

expansion compared to the CASR specimen. Despite the casting direction anisotropy, the confinement in the X-Y plane still forces the majority of expansion to the Z-direction after stresses have been induced by the passive restraint.

4.4 Discussion

4.4.1 Reaction Advancement

The reaction advancement model presented in this study is a novel combination of other alkali-silica reaction advancement presented in past research. The combination reaction advancement model is dependent upon temperature, internal saturation degree, and reaction kinetics. The inclusion of Larive (1997) parameters, τ_c, τ_l, and Φ_r, allow simple and familiar parameter calibration similar to the process outlined by Larive (1997). As evidenced in Figure 4.2, the model is capable of accurately predicting experimental expansions after calibration of model parameters.

4.4.2 Casting Direction Anisotropy

The casting direction anisotropy of ASR-expansion, observed by Jones and Clark (1996); Larive (1997); Smaoui et al. (2005), was incorporated into the model using a simple scalar value obtained from experimental testing. The scalar value, termed the coefficient of casting direction anisotropy, alters the base expansion as determined by the reaction advancement model depending on the considered direction relative to the line of action of gravity at the time of concrete placement. As evidenced by Smaoui et al. (2004), the coefficient of casting direction anisotropy is specific to each concrete mixture and must be determined experimentally for each mixture.

The value of coefficient of casting direction anisotropy is dependent on which axis the reaction advancement model parameters are calibrated. When reaction advancement model parameters are calibrated to experimental data gathered from a specimen in an axis perpendicular to gravity, the coefficients of casting direction anisotropy for the axes perpendicular to gravity will be equal to one, and the coefficient of casting direction anisotropy for the axis parallel to gravity will typically be greater than one. When reaction advancement model parameters are calibrated to experimental data gathered from a specimen in an axis parallel to gravity, the coefficient of casting direction anisotropy for the axis parallel to gravity will be equal to one, and the coefficients of casting direction anisotropy for the axes perpendicular to gravity will typically be less than one. This formulation allows for flexibility in the model in which, if necessary, expansion in only one axis of a concrete specimen is measured and coefficients of casting direction anisotropy are assumed.

The coefficient of casting direction anisotropy is capable of accurately predicting the expansion of free-swelling concrete as evidenced by Figure 4.5. The free-swelling expansions of the SASR specimen were accurately predicted using the coefficient of casting direction anisotropy to increase Z-direction expansion relative to X-direction expansion.

4.4.3 Size Effect

As evidenced in Figure 4.6, the reaction kinetics differ significantly between the SASR specimen and UASR specimen with the major difference being size. The UASR specimen has

a volume nearly 200 times that of the SASR specimen, and the SASR specimen has a surface-to-volume ratio nearly 5 times that of the UASR specimen. The larger surface-to-volume ratio of the SASR specimen corresponds with a higher susceptibility to alkali-leaching, the leading theory of causing size effect in specimens with ASR (Lindgård et al., 2013). However, smaller specimens typically experience lower expansion due to the increased alkali-leaching, a process which removes a crucial reactant from the chemical reaction. In this research, the reaction advancement kinetic parameters calibrated to the smaller SASR specimen over-predicted the expansion of the UASR specimen, which is opposite of the outcome predicted by literature. Previous research has focused on specimens smaller than 0.2 m (Lindgård et al., 2013; Multon and Sellier, 2016). Research data comparing larger specimens similar in size to the specimens in this research and typical laboratory size specimens are needed.

The reaction kinetics differ between the smaller SASR specimen and larger UASR specimen as evidenced in Figure 4.6. This difference points to the possibility of a size effect relationship between typical laboratory scale specimens and very large concrete specimens. Additional research in this area is necessary to identify a possible size effect relationship between typical laboratory scale specimens and concrete at the structural scale.

4.4.4 Stress-Dependent Anisotropic Expansion

Stress-coupled anisotropic ASR expansion was successfully predicted using a new model depending on the spherical and deviatoric stresses within concrete. The stress-dependent anisotropic expansion model uses a formulation to generate a coefficient of stress-dependency as a function of spherical and deviatoric stresses and calibrated model parameters. The coefficient of stress-dependency is used to alter the ASR expansion in each direction by reducing, eliminating, or increasing expansion as a function of the stress-state.

The model has been shown to accurately predict the reduction of ASR expansion due to restraint as evidenced in Figure 4.8. The X and Y-direction expansions are effectively reduced by the model due to the stresses generated by the steel confinement frame and steel reinforcing bars. Because the coefficient of stress-dependency is a function of the spherical and deviatoric stresses, the expansion is redirected, increasing the expansion in the Z-direction. The simulated expansions in the X and Z-directions fall within the variation

of the experimental results of the large confined specimen. However, the modeled expansion of the CASR specimen in the Z-direction is consistently lower than the average values of experimental expansion. Further calibration of the model parameters with experimental data may improve the correlation between predicted and experimental expansions.

The model was not able to accurately predict the differences in the experimental X and Y-direction expansions of the confined specimen. The model parameters require additional data for accurate calibration. Literature data concerning ASR-expansion of concrete with measured multi-axial applied loads are scarce. The model parameters in this study were calibrated to existing research performed by Gautam et al. (2017) in which a different concrete mixture was used. Additional research data investigating the development of ASR-expansion in concrete with measured multi-axial applied loads are necessary to improve models.

4.4.5 Limitations of Current Model

While the model was validated to predict the results of the experiment, some limitations do exist. The model does not account for creep or shrinkage which can have an influence on the damage developed by ASR expansion. Additionally, the current implementation of the model does not account for anisotropic damage of concrete; however, the Material Property Evolution Model is designed such that it can be used to incorporate damage based on the anisotropic expansion of the concrete.

4.5 Conclusion

A new model was developed for predicting the expansion of concrete structures affected by alkali-silica reaction. The model includes a novel combination of existing models as a alkali-silica reaction advancement model, a casting direction anisotropic expansion model, a stress-dependent anisotropic expansion model, and a material property evolution model depedent on the degree of ASR expansion. The model parameters were calibrated based on existing literature data and data generated by previous efforts of this study. The calibrated model was then validated with the experiments carried out in previous efforts of this study.

The model was shown to accurately predict the ASR-expansion of large-scale reinforced concrete specimens with confinement.

Comparison of numerical analysis and experimental data shows a difference in reaction kinetics between the smaller specimen and large-scale specimen. With ASR advancement parameters calibrated to the small plain specimen, the model significantly over-predicts expansion of the large-scale specimen with reinforcement which is opposite to the current understanding of ASR size effect (Lindgård et al., 2013). The results of this study highlight the need for additional research to be conducted to investigate a possible size effect for very-large concrete specimens affected by ASR.

The work completed in this study highlight the need for research to be conducted further investigating the relationship between measured multi-axial stresses and ASR-expansion. Only one experiment exists with which complex stress-dependent anisotropic ASR expansion models can be calibrated (Gautam, 2016). Additional experimental data are needed to determine the relationship between multi-axial stresses and ASR-expansion.

Chapter 5

Conclusions

5.1 Summary

The behavior of large-scale reinforced concrete undergoing ASR under confinement was investigated. Expansion, cracking, and material property degradation were investigated using destructive testing and tools to measure expansion. Models were developed for use in predicting the expansion of large-scale reinforced concrete specimens undergoing ASR under confinement. The results of this study can be used to assess reinforced concrete structures with ASR.

Three tasks were completed to achieve the objectives of this research:

- Task 1: Expansion Monitoring - Three large-scale reinforced concrete specimens representing a typical nuclear containment structure were constructed. Two of the three specimens were subjected to ASR, causing expansion and cracking. One of the specimens was non-expansive and served as a control specimen. One of the specimens subjected to ASR was surrounded by a steel confinement frame that restrained ASR-expansion in two primary axes of the specimen. The specimens were heavily instrumented to record internal and external expansion.

- Task 2: Material Characterization - Several standard size cylinders were constructed alongside the three large-scale specimens. These cylinders were tested for compressive strength, elastic modulus, and splitting tensile strength as a function of time. Each

time of testing was correlated to a corresponding value of expansion of the large-scale specimens. The change in material properties was related to the estimated level of ASR-expansion. ASR-affected concrete fracture properties were also measured using a wedge-splitting test. Wedge-splitting test specimens were cut from confined concrete so that expected ASR cracks were oriented at 0, 45, and 90 degrees relative to the notch of the specimens. Specimens were fractured by wedge-splitting test, and the crack mouth opening displacement was recorded. Fracture strength, stiffness, and fracture energy of ASR-affected concrete depending on the expected ASR micro-crack orientation were derived from these experiments.

- Task 3: Numerical Modeling - An anisotropic expansion model was developed to predict the expansion of confined concrete undergoing ASR. A novel combination of existing reaction advancement models was proposed. A coefficient of casting direction anisotropy was introduced to account for the inherent increase of expansion in the direction parallel to casting direction. A stress-dependent anisotropic expansion model was developed to account for the stress-dependency of ASR expansion. The stress-dependent anisotropic expansion model accounts for the stress-state of the concrete by considering the spherical and deviatoric stresses. A material property evolution model was developed to account for the initial increase of material properties due to cement hydration and the later reduction of material properties due to ASR damage. The model was capable of predicting the expansions of the experimental large-scale specimen testing.

5.2 Conclusions

Conclusions from each chapter of this dissertation are summarized:

5.2.1 Monitoring of ASR in Confined Reinforced Concrete

- ASR expansion of confined concrete is anisotropic. The reinforcement layout and steel confinement frame reduced expansions in the directions of restraint. The expansion in the unrestrained direction was increased.

- Volumetric expansions of the confined specimen and unconfined specimen were similar. The volumetric ASR-expansion of concrete is unaffected by confinement when at least one direction is unconfined. This observation suggests that ASR expansion is a volumetric phenomenon in which volumetric expansion is distributed to directions with the least restraint.

- Casting direction anisotropy, reinforcement layout, and boundary conditions cause highly anisotropic expansion pointing to the need for advanced structural models capable of capturing expansion anisotropy for analysis of in-the-field behavior.

- Surface cracking is not indicative of internal ASR-induced damage or expansion for concrete structures with reinforcement layout or confinement that drives expansion primarily in an unobservable direction. Significant distress of a structure is possible without any visible evidence of ASR.

- Visible surface cracking was not evident on the confined specimen even with Z-direction expansion exceeding 0.3%. Given that acoustic NDE methods are most influenced by the onset of ASR damage (Giannini and Folliard, 2012; Giannini et al., 2016; Kim et al., 2017), the observations of the confined specimen highlight the need to monitor critical reinforced concrete structures before visible evidence of damage appears at the surface.

- The different types of deformation instrumentation (long-gauge fiber optics and embedded transducers) yielded comparable and dependable expansion measurements despite the severity of the operating conditions (moderate temperature, high humidity, and high alkalinity)

5.2.2 Effect of ASR on the Fracture Properties of Confined Concrete

- The fracture strength, stiffness, and fracture energy of specimens with ASR was generally lower than control specimens. The lowest strength and fracture energy was measured from the specimens with expected ASR micro-cracking parallel to the notch.

- The expected direction of ASR micro-cracking relative to the notch effects fracture properties of the concrete. Specimens with expected micro-cracking perpendicular to the notch had the highest fracture properties among reactive specimens. Specimens with expected micro-cracking parallel to the notch had the lowest fracture properties among all specimens. Specimens with expected micro-cracking at a 45° angle to the notch had intermediate fracture properties.

- For the specimens with expected ASR micro-cracking perpendicular to the notch, the fracture energy was higher on average than the control specimens.

- The force-displacement curves for the ASR-affected specimens showed a much lower rate of post-peak force degradation than the control specimens, indicating a difference in failure mechanism, particularly during the crack initiation period. This is probably due to the existence of a pre-existing network of microcracks in the ASR-affected specimens.

- For some specimens with the cracks oriented perpendicular to the notch, the main crack propagated alongside that direction instead of in the direction of the applied splitting force. Since this behavior was only observed for the earliest curing time, it could indicate that the micro-cracking induced during the later stages of the ASR expansion was less oriented than during the earlier stages.

- The observations of this study highlight the need for anisotropic damage for structural models for concrete. In addition, mesoscale numerical models could be used to identify the evolution of the internal micro-cracking with the degree of restraint.

5.2.3 Modeling of ASR in Confined Reinforced Concrete

- A new model was developed for predicting the expansion of concrete structures affected by alkali-silica reaction. The model includes a novel combination of existing models alkali-silica reaction advancement model, a casting direction anisotropic expansion model, a stress-dependent anisotropic expansion model, and a material property evolution model depedent on the degree of ASR expansion.

- The model parameters were calibrated based on existing literature data and data generated by previous efforts of this study. The calibrated model was then validated with the experiments carried out in previous efforts of this study. The model was shown to accurately predict the ASR-expansion of large-scale reinforced concrete specimens with confinement.

- Comparison of numerical analysis and experimental data show a difference in reaction kinetics between the smaller specimen and large-scale specimen. With ASR advancement parameters calibrated to the small plain specimen, the model significantly over-predicts expansion of the large-scale specimen with reinforced which is opposite to the current understanding of ASR size effect (Lindgård et al., 2013). The results of this study highlight the need for additional research to be conducted to investigate a possible size effect for very-large concrete specimens affected by ASR.

- The work completed in this study highlights the need for research to be conducted further investigating the relationship between measured multi-axial stresses and ASR-expansion. Only one experiment exists with which complex stress-dependent anisotropic ASR expansion models can be calibrated (Gautam, 2016). Additional experimental data is needed to determine the relationship between multi-axial stresses and ASR-expansion.

5.3 Recommendations for Future Work

This study monitored the ASR-expansion of large-scale reinforced concrete specimens under confinement. The following recommendations are provided for future work regarding the monitoring of ASR-expansions:

- For restrained or loaded concrete, ASR-expansion should be measured in all three primary axis of a concrete specimen. Even for free-swelling plain concrete, casting direction anisotropy may cause the expansion to be considerably larger in the direction parallel to gravity at the time of concrete placement. ASR-expansion measurement is necessary in each direction to determine the coefficient of casting direction anisotropy and distribution of expansion due to restraint.

- Local internal strain transducers and long-length deformation sensors yielded similar measured expansions. One type of sensor may be sufficient to gather credible information. The resilience of the types of sensors used in this study proved to be sufficient to survive the harsh environment of ASR-expansion testing.

- A smaller size specimen was used to decide the concrete mix design. The reaction kinetics differed significantly between the small specimen and large-scale specimens. For future experimental programs investigating ASR expansions of large specimens, small specimens should also be prepared to investigate the effect of specimen size and geometry.

- Expansive pressures exerted on the steel confinement frame by the swelling concrete were not measured in this experiment. Future experiments should attempt to measure the stress applied to the concrete specimen by restraint so that the relationship between ASR-expansion and multi-axial stresses can be further investigated.

This study investigated the effect of oriented ASR micro-cracking on the fracture properties of concrete. The following recommendations are provided for future work regarding the investigation of fracture properties of ASR-affected concrete:

- The wedge-splitting test used in this study, originally proposed by Brühwiler (1988), was relatively simple to implement and perform. This study recommends this test for the standardized testing of ASR-affected concrete fracture properties.

- A clip-on strain gauge was used to measure the crack mouth opening displacement during the wedge-splitting test. Knife-edges were adhered to the concrete specimens to serve as connection points for the clip on strain gauge. This study recommends a clip-on strain gauge to measure concrete strains/displacements in future work.

- The specimens in this study were not taken to complete failure. As a result, the measured fracture energy may be significantly lower than similar concretes. Specimens should be tested to complete failure in future work to obtain comparable fracture energy values.

- Additional experimental data is needed to develop a relationship between fracture properties and ASR-expansion for confined concrete. Future studies should investigate effect of the degree of ASR-expansion on confined concrete fracture properties.

This study formed conclusions regarding the numerical analysis of ASR-affect concrete. The following recommendations are provided for future work regarding the numerical analysis of ASR-affected concrete:

- ASR-expansion is inherently anisotropic due to casting direction. Further anisotropy can be generated due to the stress-state. Models capable of considering anisotropic ASR-expansion are necessary to predict behavior of reinforced concrete structures.

- The results from this study highlight the need of anisotropic damage for structural models for concrete. In addition, mesoscale numerical models could be used to identify the evolution of the internal micro-cracking with the degree of restraint.

Bibliography

ACI Committee 318 (2014). *Building Code Requirements for Structural Concrete and Commentary, ACI318-14*. 8

ACI Committee 349 (2013). *Code Requirements for Nuclear Safety-Related Concrete Structures and Commentary, ACI349-13*. 8

Ahmed, T., Burley, E., Rigden, S., and Abu-Tair, A. I. (2003). The effect of alkali reactivity on the mechanical properties of concrete. *Construction and Building Materials*, 17(2):123–144. xiii, 5, 31

Alnaggar, M., Cusatis, G., and Di Luzio, G. (2013). Lattice discrete particle modeling (LDPM) of alkali silica reaction (ASR) deterioration of concrete structures. *Cement and Concrete Composites*, 41:45–59. 55

Bach, F., Thorsen, T., and Nielsen, M. (1993). Load-carrying capacity of structural members subjected to alkali-silica reactions. *Construction and Building Materials*, 7(2):109–115. 9

Baghdadi, N., Toutlemonde, F., and Seignol, J.-F. (2007). Modélisation de leffet des contraintes sur lanisotropie de lexpansion dans les bétons atteints de réactions de gonflement interne. In *Conférence AUGC, Bordeaux*. 58

Batic, O., Giaccio, G., and Zerbino, R. (2004). On the effect of asr cracking on the mechanical behaviour of concrete in tension and compression. In *Proceedings of the 12th International Conference on Alkali-Aggregate Reaction in Concrete*, pages 1136–1141. xiii, 30, 31

Ben Haha, M. (2006). *Mechanical Effects of Alkali-Silica Reaction in Concrete Studied by SEM-Image Analysis*. PhD thesis, Ecole Polytechnique Fédérale de Lausanne. xiii, 30, 31, 64

Blight, G. E. and Alexander, M. G. (2011). *Alkali-aggregate reaction and structural damage to concrete: engineering assessment, repair and management*. CRC Press. 3

Bracci, J., Gardoni, P., Eck, M., and Trejo, D. (2012). Performance of lap splices in large-scale column specimens affected by ASR and/or DEF. Technical Report 0-5722-1, Texas A&M University, Texas Transportation Institute The Texas A&M University System College Station, Texas 77843-3135. 17

Brühwiler, E. (1988). *Bruchmechanik von Staumauerbeton unter Quasi-Statischer und Erdbebendynamischer Belastung*. PhD thesis, Swiss Federal Institute of Technology, Lausanne, n739. 37, 89

Brühwiler, E. and Wittmann, F. (1990). The wedge splitting test, a new method of performing stable fracture mechanics tests. *Engineering fracture mechanics*, 35(1-3):117–125. 37

Capra, B. and Sellier, A. (2003). Orthotropic modelling of alkali-aggregate reaction in concrete structures: numerical simulations. *Mechanics of materials*, 35(8):817–830. 5, 56

Cast3M (2019). Cast3m 2019. http://www-cast3m.cea.fr/. [Online; accessed 31-October-2019]. 67

Charpin, L. and Ehrlacher, A. (2014). Microporomechanics study of anisotropy of asr under loading. *Cement and Concrete Research*, 63:143–157. 55

Comi, C., Fedele, R., and Perego, U. (2009). A chemo-thermo-damage model for the analysis of concrete dams affected by alkali-silica reaction. *Mechanics of Materials*, 41(3):210–230. 58

den Uijl, J. and Kaptijn, N. (2003). Shear tests on beams cut from ASR-affected bridge decks. *ACI Special Publication*, 211(SP211-06):115–133. 9

Denarié, E. (2000). *Etude expérimentale des couplages viscoélasticité-croissance des fissures dans les bétons de ciment*. PhD thesis, Ecole Polytechnique Fédérale de Lausanne, n2195. 37, 43, 52

Denarié, E., Cécot, C., and Huet, C. (2006). Characterization of creep and crack growth interactions in the fracture behavior of concrete. *Cement and concrete research*, 36(3):571–575. 37

Denarié, E., Saouma, V., Iocco, A., and Varelas, D. (2001). Concrete fracture process zone characterization with fiber optics. *Journal of engineering mechanics*, 127(5):494–502. 37, 52

Dunant, C. F. and Scrivener, K. L. (2010). Micro-mechanical modelling of alkali–silica-reaction-induced degradation using the AMIE framework. *Cement and Concrete research*, 40(4):517–525. 55

Dunant, C. F. and Scrivener, K. L. (2012). Effects of uniaxial stress on alkali–silica reaction induced expansion of concrete. *Cement and concrete research*, 42(3):567–576. 34, 35

Esposito, R., Anaç, C., Hendriks, M. A., and Çopuroğlu, O. (2016). Influence of the alkali-silica reaction on the mechanical degradation of concrete. *Journal of Materials in Civil Engineering*, 28(6):04016007. xiii, 4, 30, 31, 34, 64

Esposito, R. and Hendriks, M. A. (2016). A multiscale micromechanical approach to model the deteriorating impact of alkali-silica reaction on concrete. *Cement and Concrete Composites*, 70:139–152. 55

Fan, S. and Hanson, J. (1998). Effect of alkali silica reaction expansion and cracking on structural behavior of reinforced concrete beams. *ACI Structural Journal*, 95(5):488–495. xiii, 31

Farage, M., Alves, J., and Fairbairn, E. (2004). Macroscopic model of concrete subjected to alkali–aggregate reaction. *Cement and Concrete Research*, 34(3):495–505. 55

Feenstra, P. H. (1993). Computational aspects of biaxial stress in plain and reinforced concrete. *PhD thesis, Delft University of Technology*. 67

Folliard, K., Barborak, R., Ideker, J., Fournier, B., and Thomas, M. (2006). Laboratory Test Methods for Determining the Dosage of Lithium Nitrate Required to Control ASR-Induced Expansion. In *Marc-Andre Brub Symposium on Alkali-Aggregate Reactivity in Concrete*, pages 153–169, Montreal, Canada. 14

Fournier, B. and Bérubé, M.-A. (2000). Alkali-aggregate reaction in concrete: a review of basic concepts and engineering implications. *Canadian Journal of Civil Engineering*, 27(2):167–191. 3

Gautam, B., Panesar, D., Sheikh, S., and Vecchio, F. (2017). Effect of multiaxial stresses on alkali-silica reaction damage of concrete. *ACI Materials Journal*, 114-M52:595–604. 5, 22, 30, 57, 61, 81

Gautam, B. P. (2016). *Multiaxially Loaded Concrete Undergoing Alkali-Silica Reaction (ASR)*. PhD thesis, University of Toronto (Canada). xiii, 5, 30, 31, 32, 71, 75, 82, 87

Giaccio, G., Zerbino, R., Ponce, J., and Batic, O. (2008). Mechanical behavior of concretes damaged by alkali-silica reaction. *Cement and Concrete Research*, 38(7):993–1004. xiii, 31, 34, 51, 52

Giannini, E. and Folliard, K. (2012). Stiffness damage and mechanical testing of core specimens for the evaluation of structures affected by asr. In *Proceedings of the 14th International Conference on Alkali–Aggregate Reaction in Concrete, May*. xiii, 4, 30, 31, 32, 85

Giannini, E., Rivard, P., Kodjo, S., Wood, S., and Guimaraes, M. (2016). Development and Testing of NDE Mockup Specimens with ASR. In *Proceeding of the 15th International Conference on Alkali-Aggregate Reactions in Concrete*, Sao Paulo, Brazil. 32, 85

Giorla, A. B., Scrivener, K. L., and Dunant, C. F. (2015). Influence of visco-elasticity on the stress development induced by alkali–silica reaction. *Cement and Concrete Research*, 70:1–8. 55

Glišić, B., Hubbell, D., Sigurdardottir, D. H., and Yao, Y. (2013). Damage detection and characterization using long-gauge and distributed fiber optic sensors. *Optical Engineering*, 52(8):087101–087101. 18

Grimal, E., Sellier, A., Multon, S., Le Pape, Y., and Bourdarot, E. (2010). Concrete modelling for expertise of structures affected by alkali aggregate reaction. *Cement and Concrete Research*, 40(4):502–507. 5, 56, 58, 59, 60, 70

Hafçi, I. (2013). Effect of alkali-silica reaction expansion on mechanical properties of concrete. Master's thesis, Middle East Technical University. xiii, 30, 31

Hayes, N. W., Gui, Q., Abd-Elssamd, A., Le Pape, Y., Giorla, A. B., Le Pape, S., Giannini, E. R., and Ma, Z. J. (2018). Monitoring alkali-silica reaction significance in nuclear concrete structural members. *Journal of Advanced Concrete Technology*, 16(4):179–190. xi, xii, xiii, 11, 12, 13, 14, 17, 18, 19, 20, 21, 26, 28, 29, 30, 31, 33, 34, 35, 36, 38, 40, 41, 54, 57, 58, 61, 66, 69, 75

Herrmann, N., Niklasch, C., Kiefer, D., Gerlach, L., Le Pape, Y., and Fortier, S. (2008). PACE-1450-an experimental test setup for the investigation of the crack behaviour of prestrseed concrete containment walls. In *ICONE 16: Proceedings of the 16 th International Conference on Nuclear Engineering*, volume 4, pages 1–8, Three Park Avenue, New York, NY 10016-5990 USA. ASME, Nucl. Engn. Div; JSME, Japan Soc Mech Engineers, American Society of Mechanical Engineers. Orlando, FL. 17

Hillerborg, A., Modéer, M., and Petersson, P.-E. (1976). Analysis of crack formation and crack growth in concrete by means of fracture mechanics and finite elements. *Cement and concrete research*, 6(6):773–781. 67

Inaudi, D. (1997). *Fiber optic sensor network for the monitoring of civil structures*. PhD thesis, Ecole Polytechnique Fédérale de Lausanne. 18

Inoue, S., Fujii, M., Kobayashi, K., and Nakano, K. (1989). Structural behaviors of reinforced concrete beams affected by alkali–silica reaction. In *Proceedings of the 8th International Conference on Alkali–Aggregate Reaction in Concrete, Kyoto, Japan*, pages 17–20. 4

Jones, A. and Clark, L. (1996). The effects of restraint on ASR expansion of reinforced concrete. *Magazine of Concrete Research*, 48(174):1–13. xiii, 4, 30, 31, 60, 79

Kim, G., Giannini, E., Klenke, N., Kim, J.-Y., Kurtis, K., and Jacobs, L. (2017). Measuring Alkali-Silica Reaction (ASR) Microscale Damage in Large-Scale Concrete Slabs Using Nonlinear Rayleigh Surface Waves. *Journal of Nondestructive Evaluation*, 36(2). 32, 85

Kim, T. and Olek, J. (2012). Influence of Lithium Ions on the Chemistry of Pore Solution in Pastes and Mortars with Inert Aggregates. In *Proceedings of the 14th International Conference on Alkali-Aggregate Reaction*, Austion, Texas, USA. 14

Koyangi, W., Rokugo, K., and Uchida, Y. (1992). Mechanical properties of concrete deteriorated by alkali-aggregate reaction under various reinforcement ratios. In *Proceedings of the 9th International Conference on Alkali-Aggregate Reaction*, pages 556–563. 4

Larive, C. (1997). *Apports combinés de l'expérimentation et de modélisation à compréhension de l'alcali-réaction et de ses effets mécaniques*. PhD thesis, Laboratoire Central des Ponts et Chaussées. in French. 3, 4, 9, 34, 59, 60, 61, 64, 70, 78, 79

Léger, P., Côté, P., and Tinawi, R. (1996). Finite element analysis of concrete swelling due to alkali-aggregate reactions in dams. *Computers & structures*, 60(4):601–611. 5, 58, 64

Lindgård, J., Sellevold, E. J., Thomas, M. D., Pedersen, B., Justnes, H., and Rønning, T. F. (2013). Alkali–silica reaction (asr)performance testing: influence of specimen pre-treatment, exposure conditions and prism size on concrete porosity, moisture state and transport properties. *Cement and Concrete Research*, 53:145–167. 4, 75, 80, 82, 87

Mazars, J. (1984). Application de la mécanique de l'endommagement au comportement non linéaire et à la rupture du béton de structure. *THESE DE DOCTEUR ES SCIENCES PRESENTEE A L'UNIVERSITE PIERRE ET MARIE CURIE-PARIS 6*. 67

McCoy, W. and Caldwell, A. (1951). Influence of Lithium Ions on the Chemistry of Pore Solutions in Pastes and Mortars with Inert Aggregates. *Journal of the American Concrete Institute*, 47:693–706. 14

Miki, T., Matsutani, K., and Miyagawa, Y. (2013). Evaluation of crack propagation in ASR damaged concrete based on image analysis. In van Mier, J., Ruiz, G., Andrade, C., Yu, R., and Zhang, X., editors, *8th International Conference on Fracture Mechanics of Concrete and Concrete Structures – FraMCoS-8*, pages 1–7. 34

Miki, T. and Tsukahara, H. (2016). Crack propagation in ASR damaged concrete detected by image analysis. In Saouma, V., Bolander, J., and Landis, E., editors, *9th International Conference on Fracture Mechanics of Concrete and Concrete Structures – FraMCoS-9*, pages 1–7. 34, 51, 52

Morenon, P., Multon, S., Sellier, A., Grimal, S., Hamon, F., and Bourdarot, E. (2017). Impact of stresses and restraints on ASR expansion. *Construction and Building Materials*, 140:58–74. 34, 35, 56

Multon, S., Seignol, J.-F., and Toutlemonde, F. (2005). Structural behavior of concrete beams affected by alkali-silica reaction. *Materials Journal*, 102(2):67–76. xiii, 5, 9, 30, 31

Multon, S. and Sellier, A. (2016). Multi-scale analysis of alkali–silica reaction (asr): impact of alkali leaching on scale effects affecting expansion tests. *Cement and Concrete Research*, 81:122–133. 75, 80

Multon, S. and Toutlemonde, F. (2006). Effect of applied stresses on alkali-silica reaction-induced expansions. *Cement and Concrete Research*, 36:912–920. 3, 9, 22, 34, 38, 57, 61, 73

Na, O., Xi, Y., Ou, E., and Saouma, V. E. (2016). The effects of alkali-silica reaction on the mechanical properties of concretes with three different types of reactive aggregate. *Structural Concrete*, 17(1):74–83. xiii, 5, 30, 31

Nakamura, E., Watanabe, H., and Koga, H. (2008). Shear resisting mechanism in rc beams with stirrups fracture due to asr expansion. In *Proceedings of the 13th International Conference on Alkali-Aggregate Reaction in Concrete*. 9

NextEra Energy Seabrook (2013). Seabrook Station Response to NRC letter to NextEra Energy Seabrook CAL No. 1-2012-002, Confirmation Action Letter (CAL), Information related to Concrete Degradation Issues, dated May 16, 2012 (ML121254172). 8, 33, 57

Nixon, P. and Bollinghaus, R. (1985). The effect of alkali aggregate reaction on tensile and compressive strength of concrete. *Durability of Building Materials*, 2:243–248. 34

Poyet, S. (2003). *Etude de la dégradation des ouvrages en béton atteints par la réaction alcali-silice: Approche expérimentale et modélisation numérique multi-échelles des dégradations dans un environnement hydro-chemo-mécanique variable*. PhD thesis, Université de Marne-la-Vallée. 59, 60

Ramos, A. I. C., Roux-Langlois, C., Dunant, C. F., Corrado, M., and Molinari, J.-F. (2018). HPC simulations of alkali-silica reaction-induced damage: Influence of alkali-silica gel properties. *Cement and Concrete Research*, 109:90–102. 55

Rotter, H., Tschegg, E., Nadu, M., and Schieber, M. (1998). Determination of the specific fracture energy of AAR-affected concrete using the wedge-splitting method. *Magazine of Concrete Research*, 3:257–262. 34

Sanchez, L. (2014). *Contribution to the assessment of damage in aging concrete infrastructures affected by alkali-aggregate reaction*. PhD thesis, Université Laval. xiii, 30, 31

Sanchez, L., Fournier, B., Jolin, M., Bastien, J., Mitchell, D., and Noel, M. (2016). Thorough characterization of concrete damage caused by aar through the use of a multi-level approach. In *Proceedings of the 15th International Conference on Alkali-Aggregate Reaction in Concrete*. xiii, 30, 31

Saouma, V., Hariri-Ardebili, M., Le Pape, Y., and Balaji, R. (2016). Effect of alkali-silica reaction on the shear strength of reinforced concrete structural members. a numerical and statistical study. *Nuclear Engineering and Design*, 310:295–310. Accepted for publication. 9, 58, 64

Saouma, V. and Perotti, L. (2006). Constitutive model for alkali-aggregate reactions. *ACI materials journal*, 103(3):194. 5, 34, 55, 58

Shimizu, H., Watanabe, Y., Sekimoto, H., Oshima, R., Takiguchi, K., Masuda, Y., and Nishiguchi, I. (2005). Study on material properties in order to apply for structural analysis of turbine generator foundation affected by alkali-silica reaction. In *18th International Conference on Structural Mechanics in Reactor Technology (SMIRT 18)*, SMIRT18-H03-5, pages 2055–2060, Beijing, China. 2, 8, 33, 57

Siemes, T. and Visser, J. (2000). Low tensile strength older concrete structures with alkali-silica reaction. In *Proceedings of the 11th International Conference on Alkali-Aggregate Reaction*, pages 1029–1038. 34

Smaoui, N., Bérubé, M., Fournier, B., and Bissonette, B. (2004). Influence of specimen geometry, orientation of casting plane, and mode of concrete consolidation on expansion due to asr. *Cement, Concrete and Aggregates*, 26(2):1–13. 4, 27, 60, 79

Smaoui, N., Bérubé, M., Fournier, B., Bissonette, B., and Durand, B. (2005). Effects of alkali addition on the mechanical properties and durability of concrete. *Cement and Concrete Research*, 35:203–212. 23, 43, 79

Stanton, T. E. (1940). Expansion of concrete through reaction between cement and aggregate. *Proceedings of the American Society of Civil Engineers*, 66(10):1781–1812. 1

Swamy, R. and Al-Asali, M. (1988a). Engineering properties of concrete affected by alkali-silica reaction. *ACI Materials Journal*, 85(5):367–374. 4, 34, 64

Swamy, R. and Al-Asali, M. (1988b). Expansion of concrete due to alkali-silica reaction. *ACI Materials Journal*, 85:33–40. xiii, 5, 31, 32

Takatura, T., Ishikawa, T., Matsumoto, N., Mitsuki, S., Takiguchi, K., and Masuda, Y. (2005). Investigation of the expanded value of turbine generator foundation affected by alkali-silica reaction. In *Proceedings of the 18th International Conference on Structural Mechanics in Reactor Technology (SMIRT18)*, SMIRT18-H03-7, pages 2061–2068, Beijing, China. 2, 8, 33, 57

Tcherner, J. and Aziz, T. (2009). Effects of AAR on seismic assessment of nuclear power plants for life extensions. In *Proceedings of the 20th International Conference on Structural Mechanics in Reactor Technology (SMIRT 20)*, SMIRT20-Division 7 Paper 1789., Espoo, Finland. 2, 8, 33, 57

The Institution of Structural Engineers (1992). *Structural effects of alkali-silica reaction*. London, U.K. 3

Thomas, M., Fournier, B., Folliard, K., Ideker, J., and Resendez, Y. (2007). The Use of Lithium to Prevent or Mitigate Alkali-Silica Reaction in Concrete Pavements and

Structures, Final Report. Technical Report Publication No. FHWA-HRT-06-133, Federal Highway Administration, U.S. Department of Transportation, Washington, DC. 14

Thomas, M., Fournier, B., Folliard, K., and Resendez, Y. (2011). Alkali-silica reactivity field identification handbook. Technical report, US Federal Highway Administration. 1, 3

Ulm, F.-J., Coussy, O., Kefei, L., and Larive, C. (2000). Thermo-chemo-mechanics of asr expansion in concrete structures. *Journal of engineering mechanics*, 126(3):233–242. 3

United States Nuclear Regulatory Commission (2011). NRC Information Notice 2011-20: Concrete Degradation by Alkali-Silica Reaction. 1

United States Nuclear Regulatory Commission (2018). Commercial nuclear power reactors - operating reactors. https://www.nrc.gov/reading-rm/doc-collections/datasets/. xii, 2

U.S. Nuclear Regulatory Commission (2011). NRC Information Notice 2011-20: Concrete degradation by alkali-silica reaction. ML112241029. 8, 33, 57

Appendices

A Descriptions of Monitoring Experiment Setup

A.1 Construction of Reinforcing Bar Cages

In order to accurately represent a typical nuclear power plant structural systems, the concrete specimens would require #11 rebar spaced at 10 inches on center. Older typical nuclear power plant wall structures do not have shear reinforcement. A spacer was designed to separate the two elevations of rebar. These spacers must not be capable of developing tensile resistance. To accomplish this, the pipe sleeve connection was designed to eliminate the development of tension within the bar. With this connection, the rebar is able to slide freely in the sleeves as the rebar layers separate due to expansion. The rebar was also de-bonded to ensure that the concrete was unreinforced through the depth.

Three rebar cages were constructed. Each cage consisted of two layers of perpendicular intersecting #11 steel rebar. Each layer consisted of 10 long headed rebar and 12 short headed rebar. A fully assembled cage is shown in Figure A.1. In order to separate the two layers, #11 rebar spacers were placed inside of a pipe sleeve connection. To ensure a rigid cage structure, the pipe sleeve connections were designed long enough to prevent any rotation and differential movement of the two layers of reinforcing bars.

The top and bottom layers of rebar were laid out on the laboratory floor according to the dimensioned drawings shown in Figure A.2. The bars were welded together at corner intersections and selected intersections within the grid to ensure rigidity of the cage frame. After welding, the rebar was connected at each intersection with tie wire to ensure additional rigidity of the frame. Rebar was elevated 3" above the bottom formwork by rebar chairs. Steel tubing sleeves were welded to the top and bottom layers of reinforcement. The tubing was coped in order to achieve the maximum amount of weld-able area. #11 rebar spacers were placed in these sleeve connection in preparation for the placement of the top layer. The top layer of rebar was crane lifted on top of the spacers. Pipe sleeves were also welded to the top layer of rebar to finalize the connection. This process was completed an additional two times to manufacture the remaining cages for the specimens.

Figure A.1: Fully assembled reinforcing bar cage

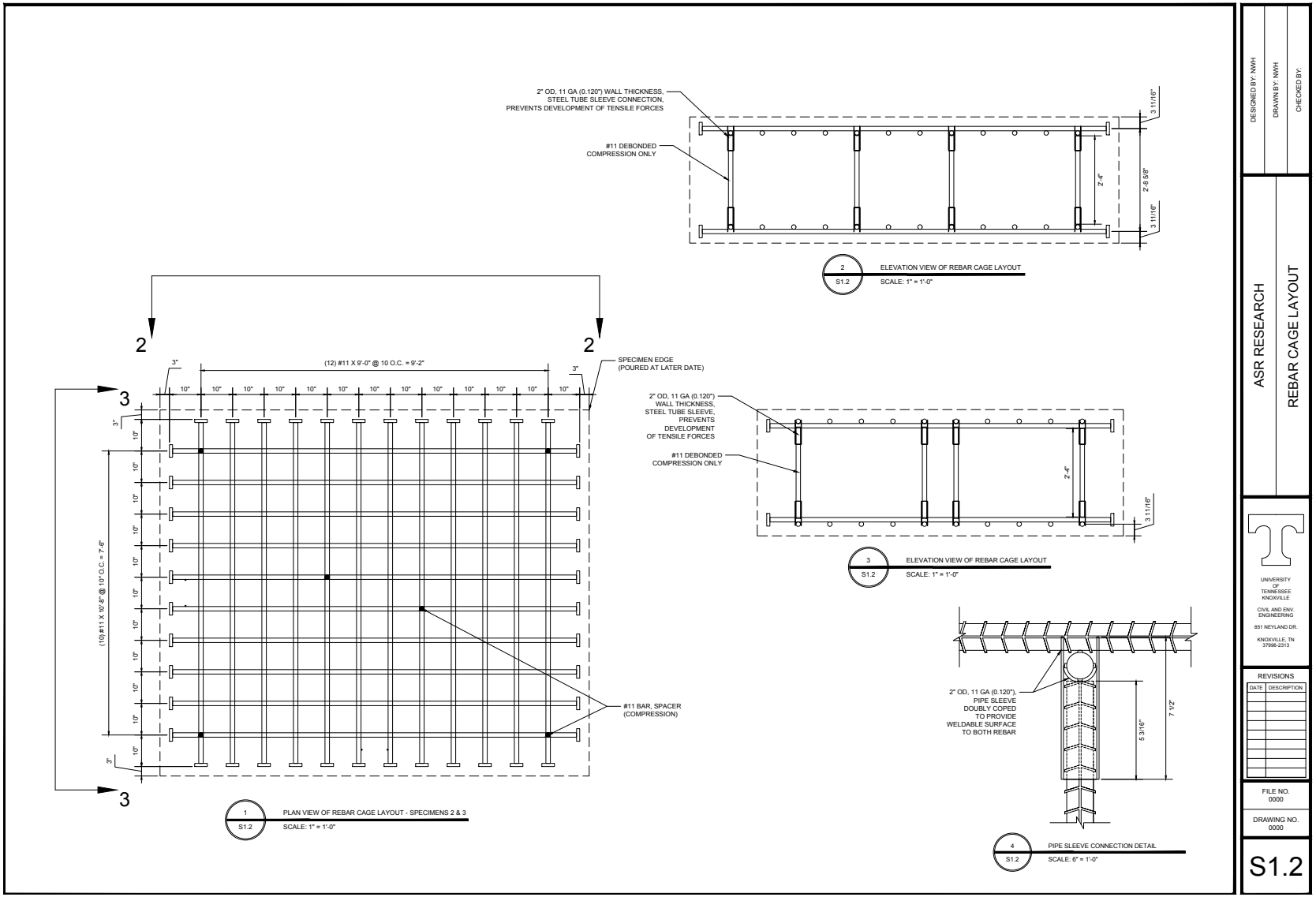

Figure A.2: Design drawings of reinforcing bar cages.

Figure A.3: Unpainted assembled steel support

A.2 Construction of Steel Supports

The bottom surface of each concrete specimen needed to be accessible to install surface sensors. Steel supports, as shown in Figure A.3, were designed and constructed to support the steel confinement frame and concrete specimens. The steel supports elevate the specimens 30 inches from the floor and hold the weight of the steel frame and concrete specimens while allowing for any movement due to expansion. Because of the harsh environment (high temperature and relative humidity) in the environmental chamber for a significant period of time (around three years), the supports were painted to resist corrosion.

Each support consists of a 1/2 inch thick plate on top and bottom and wide flange beam, W16x89. The wide flange beam was welded to each plate by four 3/16 inch fillet welds 6 inches long each. The design drawings and support layout for the steel confinement frame and concrete specimen are shown in Figure A.4.

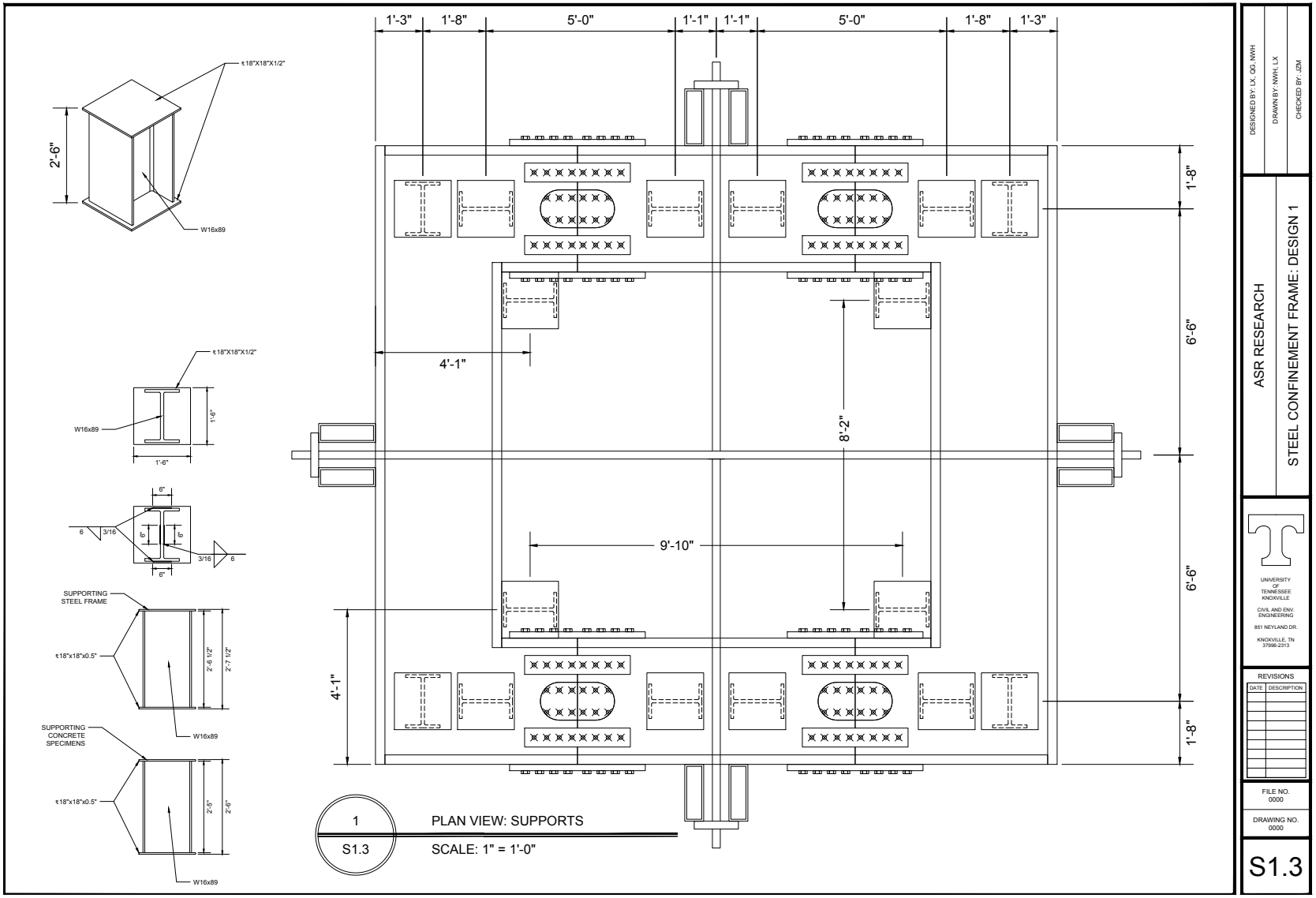

Figure A.4: Design drawings of steel supports elevating concrete specimens and confinement frame.

A.3 Installation of Concrete Formwork

The bottom formwork design consisted of three separate pieces. Each piece was made of a 1/4 inch thick steel plate with several steel beams, S5x10, welded to the underside. The formwork was constructed in three separate pieces in order to be easily removed after concrete setting.

The primary design goal was to effectively eliminate any deflection due to the weight of the liquid concrete. For this reason, a stiff system of plate and beams supported by girders was designed. The steel plate would provide a smooth, water-tight surface to contain the fresh concrete. However, due to the significant weight of the liquid concrete, a system of supports was required to effectively eliminate major deflection under the weight. The plate was supported by steel junior I-beams spaced at 12 inches or less on center. These beams were stitch welded directly to the supporting steel plate in order to provide single solid pieces for ease of construction. After installation of the three bottom formwork pieces for a single concrete specimen, five steel girders were placed underneath the steel beams at a spacing of 3 feet and held in place by utility jacks, as shown in Figure A.5. This design was used for each of the three specimens.

The formwork used to contain the fresh concrete against lateral movement was rented from MEVA formworks. The MEVA design experts recommended the use of their MevaLite product for the side formwork, after assessment of the projects needs.

Mevalite is a modular and lightweight hand-set clamp formwork system allowing for fast, easy assembly and providing high quality concrete finishes as is necessary for this project. The panels are aluminum frame construction with all-plastic facing alkus on the finishing side. Unlike traditional wooden formwork, the alkus surface does not absorb moisture from the concrete, which was an important consideration for research goals of this study. Moreover, the panels were set up side-by-side and connected with multiple clamps at each joint. These clamps were then hammered tight, and steel threaded rods were placed under the bottom formwork to pull the sides together and resist lateral forces of concrete pouring. Threaded bars were also placed through PVC through the specimen to hold the panels together at the higher elevation. Figure A.6 shows the partially completed side formwork.

Figure A.5: Completed construction of the bottom formwork with cage in place

Figure A.6: Partially assembled side formwork system

Thermal cracking of concrete is a significant issue that occurs when a large temperature differential exists between the internal core and the external sides of the concrete. The goal in this study was to slow the cooling process to minimize the temperature differential. In an attempt to eliminate all crack sources other than ASR, the formworks were insulated by placing rigid foam sheathing insulation with an R-value of three around the side and on top of the specimens, shortly after pouring. The insulation was placed with edges overlapping and secured in place with tape and plastic wrap.

A.4 Design of Steel Confinement Frame

A steel frame was designed to confine one of the concrete specimens. Due to the crane limitations in the laboratory, the frame was designed as four separate pieces. To reduce the impact of the stress concentration in the corners of the frame, the connections was designed at approximately the quarter spans of the shorter sides. The pieces were connected by a splice plate connection. The frame was designed to maximize rigidity in order to effectively minimize deflection of the frame due to the pressure of concrete ASR expansion.

In order to accomplish this goal, a steel plate girder frame was designed. As opposed to standard hot rolled shapes, a steel plate girder could be fully customized in order to meet the needs of the research testing program. A design pressure of 1200 psi was selected as the maximum ASR expansion pressure. The design drawings are shown in Figure A.7.

The steel plate girder frame was designed with the primary goal of maximizing stiffness in bending. In order to achieve this goal, 3 thick plates were chosen as flanges to the plate girder. The interior flange served as the side formwork for the confined concrete specimen. These flanges were connected by three 2 thick web plates. All steel components were manufactured from A572 Grade 50 steel plate. The welds between the components were designed to fully transfer all member forces between the components. As a result, to maintain the constructability of the cross-section, the welds were designed continuous on both sides of the inner-most web and continuous on the outside of the two outer webs. The three webs provided stiffness to the inside flange receiving the full development of internal pressure, effectively minimizing any local deflections of the flange.

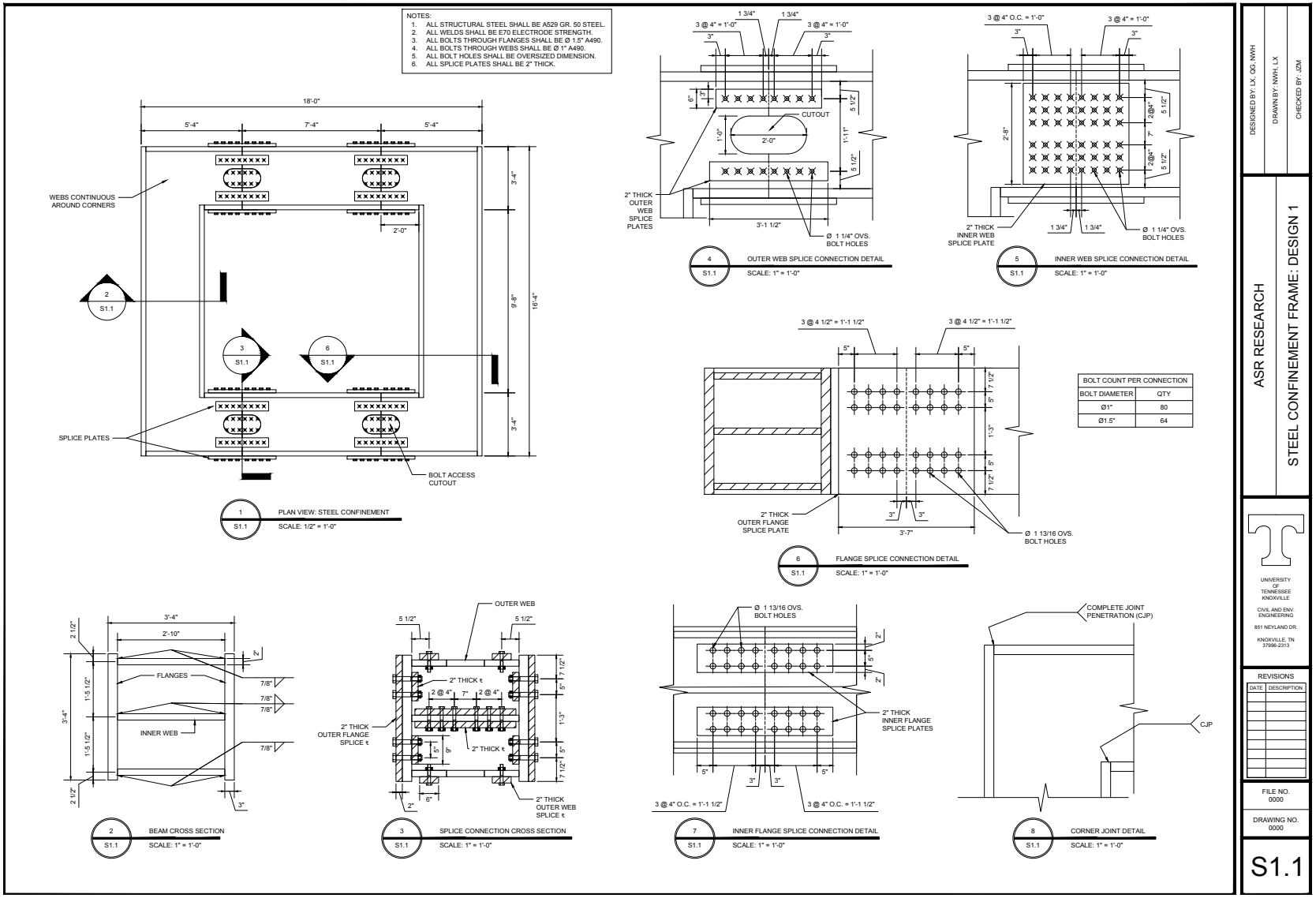

Figure A.7: Design drawings of steel confinement frame.

The use of 3 thick flanges provided the greatest moment of inertia for the cross section by pushing the cross-sectional area away from the neutral axis while also staying within the project budget. Because the primary goal was to minimize deflection, the section was significantly over-designed to the resist the bending forces induced by the concrete expansion. Because of the expected expansion pressures, 2 thick webs were required to resist the relatively large shear forces.

In order to adequately transfer forces between the flanges and webs, relatively large fillet welds were required, but due to the accessibility of the interior of the cross-section during construction, only the center web could be welded on both sides. The remaining two webs were welded only on the outside planes of the webs. Fillet welds of this size are generally only seen in large-scale steel plate girders for bridge construction; however, because of the deflection limitation requirements, these large fillet welds were necessary to adequately involve all components of the cross-section in resisting applied forces.

A bolted splice plate connection across each component of the cross-section was designed to connect the section of the steel frame. To eliminate movement of the connection and minimize local deformation as a result of the connection, a slip-critical bolted connection was designed to transfer the forces between the segments of the frame. A slip-critical connection idealizes the failure condition as the relative movement between the two connected elements. The bolts were torqued to a tension required to provide enough frictional resistance to prevent any relative movement between the connected elements and connector plates. The splice plates were designed to provide stiffness in excess of the typical cross-section at the connection. Maximizing the stiffness at the connection effectively minimized the local deformations of the structural components at the connection.

A total of 144 bolts were required for each splice plate connection. Sixty-four A490 bolts with 1.5 diameter were used to splice the flanges. Eighty A490 bolts with 1 diameter were used to splice the webs. The flange bolts were spaced at 4.5 to provide ample room for torquing. The web bolts were spaced at 4 spacing due to their smaller size.

A small cutout was incorporated into the design of the frame at the connection in order to allow for easy access for bolting of the connection. The cut-out portion allowed for the

disassembly of the steel frame, after the experiment had ended, even with the structural hex nuts being inaccessible on the inside of the frame.

A.5 Assembly of Steel Confinement Frame

The steel confinement frame was manufactured by a structural steel construction company. The frame was delivered to the laboratory as four primary pieces and with many splice plates. The first large U-shaped section was crane lifted onto the steel supports. The splice plates were crane lifted in place and secured with bolts to the first U-shaped section. The short sections were then slipped into the connection and secured with bolts. Splice plates were crane lifted in place and secured with bolts to the two short sections. The final U-shaped section was carefully crane-lifted and slid into the splice plate connection. The steel supports were then placed underneath the section to support the weight. All bolts were set in place and hand tightened. The bolts were then torqued to design specifications. Spacers were welded in place in order to create a flat bearing surface over the exposed bolts for the concrete expansion on the inside of the frame. A plate was placed and welded in place against these spacers to ensures a solid surface for the concrete expansion. The assembled steel confinement frame is shown in Figure A.8.

A.6 Installation of Instrumentation and Data Acquisition Systems

Due to the lack of shear reinforcement to serve as attachment points for internal sensors, a network of positioning bars was created on which internal sensors could be attached. 1/8 inch diameter smooth rods coated to prevent concrete bond were placed between the two elevations of reinforcing bars to serve as connection points for internal sensors.

KM-100B strain transducers from Tokyo Sokki Kenkyujo Co., Ltd represented in the US by Texas Measurements, Inc. were used in the testing program. A total of 76 KM-100B and KM-100BT transducers were placed in the rebar cages of the three specimens. The KM-100BT models included thermo-couples to measure internal concrete temperature. 32 KM transducers were installed in each of the two reactive specimens. 12 KM transducers were installed in the control specimen. These transducers were oriented in each primary axis

of the specimens to measure the full three-dimensional expansion history. A KM transducer attached to position bar is shown in Figure A.9.

SOFO standard deformation sensors developed by Smartec were embedded within each specimen and attached to the bottom surface of each specimen. Five SOFO sensors were embedded within the concrete specimens to measure through-thickness expansion. Two SOFO sensors were embedded within each reactive specimen. One SOFO sensor was embedded within the control specimen. 7 SOFO sensors were attached to the bottom surfaces of concrete specimens Two SOFO sensors were attached to each of the confined reactive specimen and control specimen. Three SOFO sensors were attached to the unconfined reactive specimen. Sensors were attached to the concrete surfaces angle anchors with anchor bolts approximately 3 inches deep. A SOFO attached to the bottom surface of a specimen is shown in Figure A.10.

Two separate data acquisition systems were used to collect data from the sensor networks. The KM transducer sensor network was connected to a National Instruments data acquisition unit. The SOFO sensor network was connected to a SOFO lite data acquisition unit. The data acquisition units were housed in a protective casing outside of the environmental chamber in which the specimen were contained as shown in Figure A.11. The sensor cables exited the environmental chamber at a singular location and were connected to the data acquisition units.

A.7 Concrete Placement

The total pour volume of all specimens including the large-scale specimens and companion material testing specimens was 48.5 cubic yards. The concrete was prepared by a local ready mix plant. A total of 6 ready mix trucks delivered the concrete directly to the laboratory. Sodium hydroxide and lithium nitrate were added to the trucks at the laboratory and allowed to thoroughly mix before concrete placement. Concrete trucks were backed directly into the lab to load a crane-mounted concrete hopper. The concrete hopper dispensed directly into a smaller hopper which guided the concrete through an elephant truck directly to the intended location for placement. This method of placement allowed the concrete to be placed slowly as to avoid any movement of the sensors. The concrete was vibrated using a rod vibrator

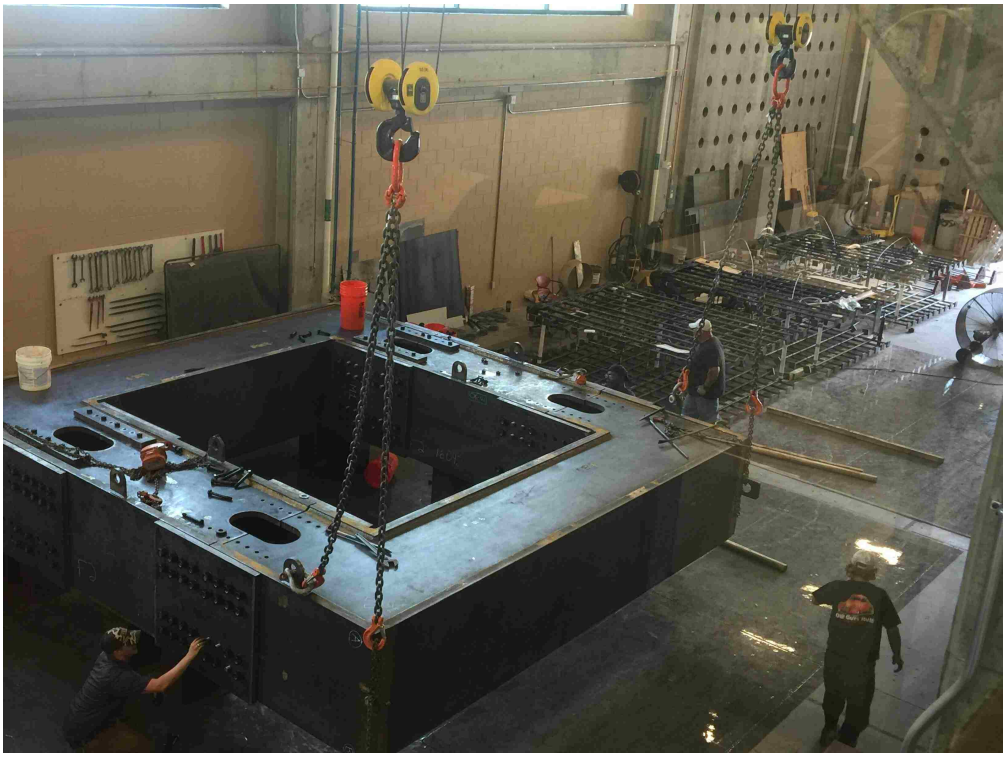

Figure A.8: Assembled steel confinement frame

Figure A.9: KM-100B strain transducer attached to positioning bar within rebar cage

Figure A.10: SOFO deformation sensor attached to bottom surface of concrete specimen

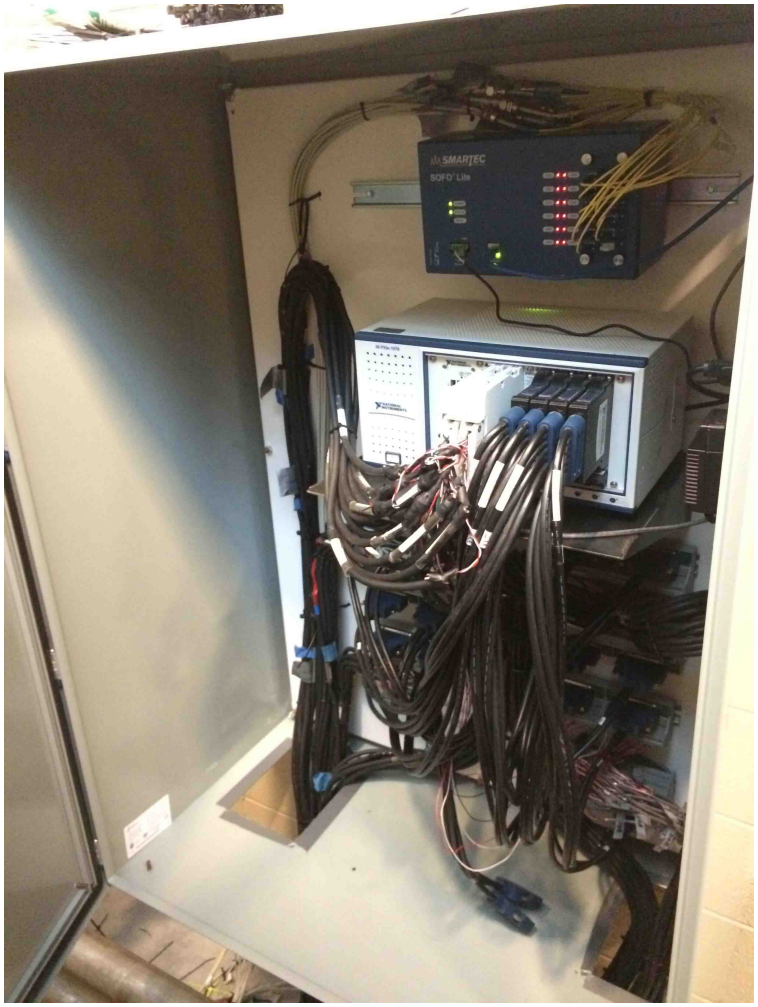

Figure A.11: Data acquisition systems in protective casing

carefully avoiding all sensors. A team of professional concrete workers prepared the finish for the large specimens. The specimens were troweled to a flat surface and curing compound was sprayed onto the top surface. Shortly after, wet burlap and plastic sheeting was placed covering the concrete.

A.8 Construction of Environmental Chamber

The environmental chamber was designed by Norlake Scientific with the primary goals for temperature and humidity control being 100F (+/- 2F) and 95% RH (+/- 2%). In order to maintain the temperature and relative humidity, a heating system consisting of both heating evaporators and heating units accommodated by air circulators was designed. The chamber was later upgraded to provide environmental conditions of 77F (+/- 2F) and 90% RH (+/- 2%) for the second year of accelerated testing.

The environmental chamber was delivered as panels on multiple pallets. The panels consisted of embossed steel filled with foam insulation. Each panel had a set of locks to secure adjacent panels to each other. The floor connection was sealed by a vinyl floor sealer placed underneath the wall panels.

The construction crew initially laid out the walls and verified the building dimension. Vinyl floor sealers were then placed in the locations of the walls. The construction crew began by assembling a corner section first. The remaining walls were built off of this corner until all wall panels had been erected and secured in place. Doors were installed according to the chamber design. Silicone caulk was used to seal the vinyl floor sealers to the concrete floor of the laboratory.

After all wall panels were secured in place, a steel post and beam system was installed to support the ceiling panels. Ceiling panels were installed and locked in place to adjacent wall panels and other ceiling panels. Each ceiling panel was attached to a steel beam supporting its span. Once completed, the chamber measured approximately 53 feet long and 24 feet wide. This area allowed for all three samples and all concrete cylinders and other smaller specimens to be contained within the same environment as shown in Figure A.12.

After installation of all panels, a second construction crew began the mechanical and electrical work. All misters and heating units were installed and connected to the electrical

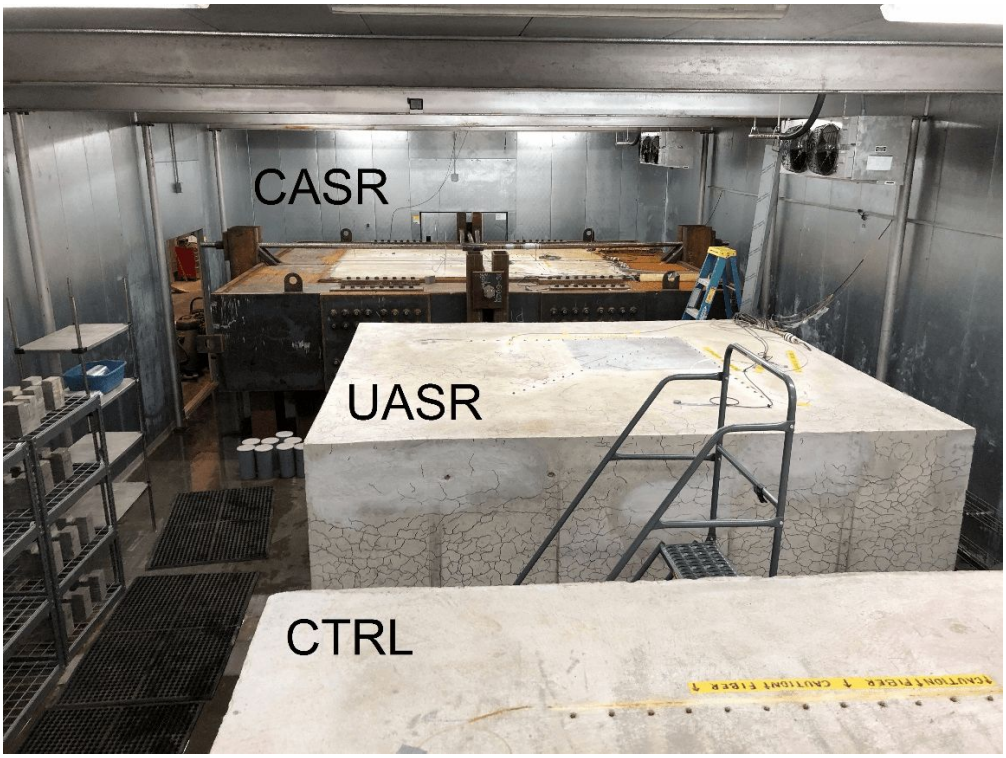

Figure A.12: Specimens located inside environmental chamber

system. Afterwards, all lights were attached to the ceiling and connected to the electrical system. The system was initiated at a concrete age of 26 days at which time all specimens were uncovered.

B Descriptions of Wedge-Splitting Test Setup

B.1 Cutting Process of Confined Concrete

The concrete cutting was performed by professional concrete cutters. Concrete was confined in rolled steel plate forming a cylinder. Prior to testing, the concrete was removed from the steel confinement by cutting through the steel plate. The large concrete cylinders were then cut into the wedge-splitting test specimens using a custom designed table with wall-mounted concrete saw as shown in Figure B.1a. For 00D and 90D specimens, each cylinder was cut 9 times to produce six 4 x 8 x 8 inch rectangular prisms. For 45D specimens, each cylinder was cut 13 times to produce six 4 x 8 x 8 inch rectangular prisms.

The lowered portion and notch of each specimen was created using a masonry saw as shown in Figure B.1b. The blade was locked at height, and the specimen was repeatedly moved across the blade at small increments from side to side to generate the lowered portion for each specimen. The blade was then lowered and locked at a new height to generated the a consistent notch between specimens.

(a) Confined cylinder cutting

(b) Notch cutting

Figure B.1: Cutting of wedge-splitting test specimens

C Descriptions of Numerical Analysis Processes

C.1 Sample Cast3M Input

Note: This input uses a developer version of Cast3M 2019 with a custom concrete model (MODE). As a result, this input will not function correctly for the standard version of Cast3M 2019.

```
* Anisotropic ASR, 3D
* Elastic Damage calculation

OPTI 'LANG' 'ANGLAIS';
OPTI 'DIME' 3 'MODE' TRID 'ELEM' CUB8;

* * Load one time for each working directory
* UTIL PROC 'ASR.procedur'; fin;

************************************************************
* PROCEDURES
************************************************************

*=============================================================

* BORNE

*=============================================================
DEBP @BORNE val1*'CHPOINT'
 vmin1*'FLOTTANT' vmax1*'FLOTTANT';
* Lower and Upper Bound -
*   vmin1 is lower bound & vmax1 is upper bound
t1 = (0.5 * ( (val1 - vmin1) + (ABS (val1 - vmin1) ) ) )
 + vmin1;
vborne = vmax1 -
 (0.5 * ( (vmax1 - t1 ) + (ABS (vmax1 - t1) ) ) ) ;
FINP vborne;
```

```
*=================================================================

* Increase of material properties
*   due to hydration and decreased poro

*=================================================================
DEBP @RM_PORO
x1*'FLOTTANT'
lambdah1*'FLOTTANT'
* epsasr*'MCHAML' ;
epsasr*'CHPOINT' ;

temp1 = (-1. / lambdah1 ) * epsasr ;
temp2 = (-1. * (EXP temp1)) ;
temp3 = (x1 * (1. + temp2)) + 1. ;

FINP temp3;

*=================================================================

* Degradation of material properties due to ASR

*=================================================================
DEBP @RM_ASR
Dmax1*'FLOTTANT'
lambdaa1*'FLOTTANT'
* epsasr*'MCHAML' ;
epsasr*'CHPOINT' ;

temp1 = (-1. / lambdaa1 ) * epsasr ;
temp2 = (-1. * (EXP temp1)) ;
temp3 = (-1. * Dmax1 * (1. + temp2)) + 1. ;

FINP temp3;

*=================================================================
```

```
* ASR expansion calculation based on kinetics

*=============================================================
DEBP @ASRSTR0 taul1*'FLOTTANT' tauc1*'FLOTTANT'
 sl0*'FLOTTANT' EaRasr1*'FLOTTANT' tempcon1*'FLOTTANT'
 tempref1*'FLOTTANT' dt*'FLOTTANT'
 aff1*'CHPOINT' sli1*'CHPOINT' slf1*'CHPOINT' mod1*'MMODEL';

surf1 = EXTR mod1 MAILLAGE;

valexp1 = EXP (-1.*taul1/tauc1) ;
coef2 = (1./tauc1) / ( (1 - sl0) * (1 + valexp1) );
slm1 = 0.5 * (sli1 + slf1) ;
* Positive part
sma1 = slm1 - (MANU 'CHPO' surf1 'T' sl0); absma1 = ABS sma1;
coeff3 = 0.5 * (sma1 + absma1 ) ;
* term at the right
temp4 = MANU 'CHPO' surf1 'T' valexp1 ;
* produit
lmot1 = 'MOTS' 'T' ;
temp2 = coeff3 '*' (slm1 - aff1) lmot1 lmot1 lmot1;
temp3 = temp2 '*' (aff1 + temp4) lmot1 lmot1 lmot1;
coeftem1 = EXP(-1. * EaRasr1 * ((1./tempcon1) - (1./tempref1))) ;

aff2 = aff1 + ( dt * ( coef2 * temp3) * coeftem1 ) ;
aff2 = @BORNE aff2 0. 1. ;
FINP aff2;

*=============================================================

* ASR expansion with casting direction anisotropy

*=============================================================
DEBP @ASRDEF3 phir1*'FLOTTANT' anisx1*'FLOTTANT'
 anisy1*'FLOTTANT' anisz1*'FLOTTANT'
```

```
 aff1*'CHPOINT' aff2*'CHPOINT' mod1*'MMODEL' ;

* INITIALISATION
surf1 = EXTR mod1 MAILLAGE;
test1 = MANU CHPO surf1 3 'UX' 1. 'UY' 1. 'UZ' 1. ;
test2 = EPSI test1 mod1;
defi0 = ( EXP (0.*test2) );

temp1 =  phir1 *  (aff2 - aff1) ;
temp2 = CHAN CHAM temp1 mod1;
temp3 = CHAN 'TYPE' temp2 'DEFORMATIONS';
temp4 = CHAN 'STRESSES' temp3 mod1;
tempx1 = CHAN 'COMP' temp4 'EPXX';
tempy1 = CHAN 'COMP' temp4 'EPYY';
tempz1 = CHAN 'COMP' temp4 'EPZZ';
* Definition of the loading
lmotx1='MOTS' 'EPXX'; lmoty1='MOTS' 'EPYY'; lmotz1='MOTS' 'EPZZ';
epsxx1 = anisx1 * (EXCO defi0 'EPXX');
epsyy1 = anisy1 * (EXCO defi0 'EPYY');
epszz1 = anisz1 * (EXCO defi0 'EPZZ');
epsx1 = tempx1 '*' epsxx1 lmotx1 lmotx1 lmotx1;
epsy1 = tempy1 '*' epsyy1 lmoty1 lmoty1 lmoty1;
epsz1 = tempz1 '*' epszz1 lmotz1 lmotz1 lmotz1;
epsxy1 = 0.*(EXCO defi0 'GAXY');
epsxz1 = 0.*(EXCO defi0 'GAXZ');
epsyz1 = 0.*(EXCO defi0 'GAYZ');
defi1 = epsx1 + epsy1 + epsz1  + epsxy1  + epsxz1  + epsyz1;

FINP defi1;

*=============================================================

* New ASR Anisotropic Stress-Coupled-Expansion Model

*=============================================================

DEBP @ASRANI3 phir1*'FLOTTANT' anisx1*'FLOTTANT'
```

```
 anisy1*'FLOTTANT' anisz1*'FLOTTANT'
 aff1*'CHPOINT' aff2*'CHPOINT' mod1*'MMODEL'
 stress1*'MCHAML' coefstr1*'LISTREEL'
 coefstr2*'LISTREEL' coefstr3*'LISTREEL';

* INITIALISATION
surf1 = EXTR mod1 MAILLAGE;
test1 = MANU CHPO surf1 3 'UX' 1. 'UY' 1. 'UZ' 1. ;
test2 = EPSI test1 mod1;
defi0 = ( EXP (0.*test2) );

* Calculation of free anisotropic ASR
temp1 =  phir1 *  (aff2 - aff1);
temp2 = CHAN CHAM temp1 mod1;
temp3 = CHAN 'TYPE' temp2 'DEFORMATIONS';
temp4 = CHAN 'STRESSES' temp3 mod1;
tempx1 = CHAN 'COMP' temp4 'EPXX';
tempy1 = CHAN 'COMP' temp4 'EPYY';
tempz1 = CHAN 'COMP' temp4 'EPZZ';
* Definition of the loading
lmotx1 = 'MOTS' 'EPXX';
lmoty1 = 'MOTS' 'EPYY'; lmotz1 = 'MOTS' 'EPZZ';
epsxx1 = anisx1 * (EXCO defi0 'EPXX');
epsyy1 = anisy1 * (EXCO defi0 'EPYY');
epszz1 = anisz1 * (EXCO defi0 'EPZZ');
epsxx1 = tempx1 '*' epsxx1 lmotx1 lmotx1 lmotx1;
epsyy1 = tempy1 '*' epsyy1 lmoty1 lmoty1 lmoty1;
epszz1 = tempz1 '*' epszz1 lmotz1 lmotz1 lmotz1;

* EXTRACT PARAMETER VALUES
A1 = EXTR coefstr1 1; A2 = EXTR coefstr1 2;
A3 = EXTR coefstr1 3; A4 = EXTR coefstr1 4;
A5 = EXTR coefstr1 5;
B1 = EXTR coefstr2 1; B2 = EXTR coefstr2 2;
B3 = EXTR coefstr2 3; B4 = EXTR coefstr2 4;
B5 = EXTR coefstr2 5;
```

```
C1 = EXTR coefstr3 1; C2 = EXTR coefstr3 2;
C3 = EXTR coefstr3 3; C4 = EXTR coefstr3 4;
C5 = EXTR coefstr3 5;

* Stress Calculation

strxx1 = CHAN 'TYPE'
 (REDU (EXCO 'SMXX' stress1 'SCAL') mod1) 'SCALAIRE';
stryy1 = CHAN 'TYPE'
 (REDU (EXCO 'SMYY' stress1 'SCAL') mod1) 'SCALAIRE';
strzz1 = CHAN 'TYPE'
 (REDU (EXCO 'SMZZ' stress1 'SCAL') mod1) 'SCALAIRE';
strsph1 garb1 garb2 = INVA mod1 stress1;
strsph1 = (1./3.) * strsph1;
strdev1 = strxx1 - strsph1;
strdev2 = stryy1 - strsph1;
strdev3 = strzz1 - strsph1;

* Beta Adjustment Calculations
temp1 = strsph1 - A3;
temp2 = -1.*temp1 / A1;
temp3 = 1 - (EXP (temp2));
temp4 = temp2 + (A2 / A1);
temp5 = 1 + (EXP (temp4));
betsph1 = A5 + (A4 * (temp3 / temp5));
betsph1 = (betsph1 + (ABS (betsph1))) / 2.;

temp1 = strdev1 - B3;
temp2 = -1.*temp1 / B1;
temp3 = 1 - (EXP (temp2));
temp4 = temp2 + (B2 / B1);
temp5 = 1 + (EXP (temp4));
betdev11 = B5 + (B4 * (temp3 / temp5));
betdev11 = (betdev11 + (ABS (betdev11))) / 2.;

temp1 = strdev2 - B3;
```

```
temp2 = -1.*temp1 / B1;
temp3 = 1 - (EXP (temp2));
temp4 = temp2 + (B2 / B1);
temp5 = 1 + (EXP (temp4));
betdev12 = B5 + (B4 * (temp3 / temp5));
betdev12 = (betdev12 + (ABS (betdev12))) / 2.;

temp1 = strdev3 - B3;
temp2 = -1.*temp1 / B1;
temp3 = 1 - (EXP (temp2));
temp4 = temp2 + (B2 / B1);
temp5 = 1 + (EXP (temp4));
betdev13 = B5 + (B4 * (temp3 / temp5));
betdev13 = (betdev13 + (ABS (betdev13))) / 2.;

temp1 = -1. * (strdev2 + strdev3) - C3;
temp2 = -1.*(temp1 / C1);
temp3 = 1 - (EXP (temp2));
temp4 = temp2 + (C2 / C1);
temp5 = 1 + (EXP (temp4));
betdev21 = C5 + (C4 * (temp3 / temp5));
betdev21 = (betdev21 + (ABS (betdev21))) / 2.;

temp1 = -1. * (strdev3 + strdev1) - C3;
temp2 = -1.*temp1 / C1;
temp3 = 1 - (EXP (temp2));
temp4 = temp2 + (C2 / C1);
temp5 = 1 + (EXP (temp4));
betdev22 = C5 + (C4 * (temp3 / temp5));
betdev22 = (betdev22 + (ABS (betdev22))) / 2.;

temp1 = -1. * (strdev1 + strdev2) - C3;
temp2 = -1.*(temp1 / C1);
temp3 = 1 - (EXP (temp2));
temp4 = temp2 + (C2 / C1);
temp5 = 1 + (EXP (temp4));
```

```
betdev23 = C5 + (C4 * (temp3 / temp5));
betdev23 = (betdev23 + (ABS (betdev23))) / 2.;

beta1 = betsph1 + betdev11 + betdev21;
beta2 = betsph1 + betdev12 + betdev22;
beta3 = betsph1 + betdev13 + betdev23;

* Adjust ASR expansion
beta1 = CHAN 'TYPE' beta1 'DEFORMATIONS';
beta1 = CHAN 'COMP' beta1 'EPXX';
epsxx1 = beta1 '*' epsxx1 lmotx1 lmotx1 lmotx1;

beta2 = CHAN 'TYPE' beta2 'DEFORMATIONS';
beta2 = CHAN 'COMP' beta2 'EPYY';
epsyy1 = beta2 '*' epsyy1 lmoty1 lmoty1 lmoty1;

beta3 = CHAN 'TYPE' beta3 'DEFORMATIONS';
beta3 = CHAN 'COMP' beta3 'EPZZ';
epszz1 = beta3 '*' epszz1 lmotz1 lmotz1 lmotz1;

epsxy1 = 0.*(EXCO defi0 'GAXY');
epsxz1 = 0.*(EXCO defi0 'GAXZ');
epsyz1 = 0.*(EXCO defi0 'GAYZ');

defi1 = epsxx1 + epsyy1 + epszz1 + epsxy1 + epsxz1 + epsyz1;

FINP defi1;

*=============================================================

* Isoler une face dans un plan defini par 3 points
* Isolate a face in a plane defined by 3 points

*=============================================================

DEBPROC FAPLAN VOLU1*MAILLAGE P0*POINT P1*POINT P2*POINT
```

```
                    TOL1*FLOTTANT NOR/ENTIER X1/FLOTTANT X2/FLOTTANT;
SUSU='ENVE' VOLU1;
SUPO='CHAN' 'POI1' SUSU;
FAPO=SUPO 'POIN' 'PLAN' P0 P1 P2 TOL1;
FACE1=SUSU 'ELEM' 'APPUYE' 'STRICTEMENT' FAPO;
SI (EXISTE NOR);
    VAL2MIN=X1 + TOL1;
    VAL2MAX=X2 - TOL1;
    CODIR='COOR' NOR FACE1;
    SUDIRP=CODIR 'POIN' 'COMPRIS' VAL2MIN VAL2MAX;
    FACE1=FACE1 'ELEM' 'APPUYE' 'STRICTEMENT' SUDIRP;
FINSI;
FINPROC FACE1;

*=============================================================================

* GEOMETRY

*=============================================================================

*****************************************************************
* Global Geometry Parameters
CL = 3.4544 ;
CW = 2.9464 ;
CH = 1.0160 ;

N = 0.1016;

*****************************************************************
* Steel Confinement Frame
* Create cross sections
* Define basic locations
a1 = 0.0762;
b1 = 0.0381;
b2 = 0.0508;
b3 = 0.3937;
```

```
leng1 = 1.0160;
leng2 = 0.8636;
leng3 = (leng2 + (a1));

dist1 = CL;
dist2 = (CW);

* Define line densities
nelema1 = ENTI 'SUPERIEUR' (a1/N);
nelemb1 = ENTI 'SUPERIEUR' (b1/N);
nelemb2 = ENTI 'SUPERIEUR' (b2/N);
nelemb3 = ENTI 'SUPERIEUR' (b3/N);
nelemw1 = ENTI (leng2/N);

nelemd1 = ENTI (dist1/N);
nelemd2 = ENTI (dist2/N);

* Define points
p0 = (0.) (0.) (0.);
p1 = (a1) (0.) (0.);
p2 = (a1) (0.) (b1);
p3 = (a1) (0.) (b1 + b2);
p4 = (a1) (0.) (b1 + b2 + b3);
p5 = (a1) (0.) (b1 + (2.*b2) + b3);
p6 = (a1) (0.) (b1 + (2.*b2) + (2.*b3));
p7 = (a1) (0.) (b1 + (3.*b2) + (2.*b3));
p8 = (a1) (0.) ((2.*b1) + (3.*b2) + (2.*b3));

* Draw construction lines
l12 = DROI nelemb1 p1 p2;
l23 = DROI nelemb2 p2 p3;
l34 = DROI nelemb3 p3 p4;
l45 = DROI nelemb2 p4 p5;
l56 = DROI nelemb3 p5 p6;
l67 = DROI nelemb2 p6 p7;
```

```
l78 = DROI nelemb1 p7 p8;
lfl1 = (l12 ET l23 ET l34 ET l45 ET l56 ET l67 ET l78);

* Create construction surfaces
xflang1 = lfl1 TRAN nelema1 ((-1.*a1) 0. 0.);
xweb1 = (l23 ET l45 ET l67) TRAN nelemw1 ((leng2) 0. 0.);
xflang2 = xflang1 PLUS (leng3 0. 0.);

xsect1 = (xflang1 ET xweb1 ET xflang2) COUL 'BLEU';
ELIM xsect1 0.0001;

* Generate cross-sections for corner sections
xweb3 = (xweb1 'TOUR' -90 (0. 0. 0.) (0. 0. 1.)) COUL 'BLEU';
xflang3 = (xflang2 'TOUR' -90 (0. 0. 0.) (0. 0. 1.)) COUL 'BLEU';
xflang4 = (xflang2 SYME 'PLAN' p0 (0. 1. 0.) (0. 0. 1.))
 COUL 'BLEU';
DEPL xflang4 'MOINS' (0. a1 0.);

* Generate cross-sections for main sections
xsect2 = xsect1 SYME 'PLAN' p0 (0. 1. 0.) (0. 0. 1.);
DEPL xsect1 'TOUR' -90 (0. 0. 0.) (0. 0. 1.);
DEPL xsect2 'MOINS' (0. a1 0.);

* Create volumes
* Points of center concrete mesh
pcx = CL/2.;
pcy = CW/2.;
pcz = CH/2.;

* Lines to generate extended section mesh
* Line for generation of main section vsect2
gen1 = DROI nelema1 (0. 0. 0.) (0. a1 0.);
gen2 = DROI nelemd2 (0. a1 0.) (0. (a1 + dist2) 0.);
gen3 = DROI nelema1 (0. (a1 + dist2) 0.)
 (0. ((2.*a1) + dist2) 0.);
lig1 = gen1 ET gen2 ET gen3;
```

```
* Line for generation of corner web+flange
gen1 = DROI nelema1 (0. 0. 0.) ((-1.*a1) 0. 0.);
gen2 = DROI nelemw1 ((-1.*a1) 0. 0.) (((-1.*a1) - leng2) 0. 0.);
lig2 = gen1 ET gen2;

* Line for generation of corner flange
gen1 = DROI nelemw1 (0. 0. 0.) (0. (-1. * leng2) 0.);
gen2 = DROI nelema1 (0. (-1. * leng2) 0.)
 (0. ((-1. * a1) - leng2) 0.);
lig3 = gen1 ET gen2;

* Creation of mesh volumes
* Main sections
vsect1 = xsect1 VOLU nelemd1 'TRAN' (dist1 0. 0.);
vsect2 = xsect2 VOLU 'GENE' lig1;
vsect3 = vsect1 SYME 'PLAN' (pcx pcy pcz)
 (pcx pcy 0.) (0. pcy pcz);
vsect4 = vsect2 SYME 'PLAN' (pcx pcy pcz)
 (pcx pcy 0.) (pcx 0. pcz);

* Corner sections
vcornp1 = (xflang3 ET xweb3) VOLU 'GENE' lig2;
vcornp2 = xflang4 VOLU 'GENE' lig3;
vcorn1 = vcornp1 ET vcornp2;
vcorn2 = vcorn1 SYME 'PLAN' (pcx pcy pcz)
 (pcx pcy 0.) (0. pcy pcz);
vcorn3 = vcorn2 SYME 'PLAN' (pcx pcy pcz)
 (pcx pcy 0.) (pcx 0. pcz);
vcorn4 = vcorn1 SYME 'PLAN' (pcx pcy pcz)
 (pcx pcy 0.) (pcx 0. pcz);

* Join volumes and eliminate
frtotal = vsect1 ET vcorn1 ET vsect2 ET vcorn2 ET
          vsect3 ET vcorn3 ET vsect4 ET vcorn4;
* frtotal = vsect1;
```

```
ELIM frtotal 0.0001;

*****************************************************************
* Concrete

NCL = ENTI (CL / N) ;
NCW = ENTI (CW / N) ;

C1 = 0 0 0 ;
C2 = CL 0 0 ;
C3 = CL CW 0 ;
C4 = 0 CW 0 ;
C5 = 0 0 CH;
C6 = CL 0 CH ;
C7 = CL CW CH ;
C8 = 0 CW CH ;
*
C1C2 = C1 D NCL C2 ;
C2C3 = C2 D NCW C3 ;
C3C4 = C3 D NCL C4 ;
C4C1 = C4 D NCW C1 ;

cobase = DALL C1C2 C2C3 C3C4 C4C1;
*
cototal = cobase VOLU 'GENE' lfl1;

cototal = cototal COUL 'VERT';
ELIM cototal 0.0001;

* Join frame and concrete
cftotal = cototal ET frtotal;

*****************************************************************
* Steel Reinforcement
* Locations
SELE1 = 0.0937;
```

```
SELE2 = 0.1295;
SELE3 = 0.8865;
SELE4 = 0.9223;
space1 = 0.2540;
offs1 = 0.3302;


* steel bars in X-direction at lower elevation
steels1 = 0.1016 offs1 SELE1 ;
steele1 = 3.3528 offs1 SELE1 ;

st1101 = steels1 D 1 steele1 ;
st1102 = st1101 PLUS (0.0000 (1. * space1) 0.0000) ;
st1103 = st1101 PLUS (0.0000 (2. * space1) 0.0000) ;
st1104 = st1101 PLUS (0.0000 (3. * space1) 0.0000) ;
st1105 = st1101 PLUS (0.0000 (4. * space1) 0.0000) ;
st1106 = st1101 PLUS (0.0000 (5. * space1) 0.0000) ;
st1107 = st1101 PLUS (0.0000 (6. * space1) 0.0000) ;
st1108 = st1101 PLUS (0.0000 (7. * space1) 0.0000) ;
st1109 = st1101 PLUS (0.0000 (8. * space1) 0.0000) ;
st1110 = st1101 PLUS (0.0000 (9. * space1) 0.0000) ;

st11 = st1101 ET st1102 ET st1103 ET st1104
    ET st1105 ET st1106 ET st1107 ET st1108
    ET st1109 ET st1110;

* steel bars in X-direction at higher elevation
steels1 = 0.1016 offs1 SELE4 ;
steele1 = 3.3528 offs1 SELE4 ;

st1201 = steels1 D 1 steele1 ;
st1202 = st1201 PLUS (0.0000 (1. * space1) 0.0000) ;
st1203 = st1201 PLUS (0.0000 (2. * space1) 0.0000) ;
st1204 = st1201 PLUS (0.0000 (3. * space1) 0.0000) ;
st1205 = st1201 PLUS (0.0000 (4. * space1) 0.0000) ;
st1206 = st1201 PLUS (0.0000 (5. * space1) 0.0000) ;
```

```
st1207 = st1201 PLUS (0.0000 (6. * space1) 0.0000) ;
st1208 = st1201 PLUS (0.0000 (7. * space1) 0.0000) ;
st1209 = st1201 PLUS (0.0000 (8. * space1) 0.0000) ;
st1210 = st1201 PLUS (0.0000 (9. * space1) 0.0000) ;

st12 = st1201 ET st1202 ET st1203 ET st1204
    ET st1205 ET st1206 ET st1207 ET st1208
    ET st1209 ET st1210;

* steel bars in Y-direction at lower elevation
steels1 = offs1 0.1016 SELE2 ;
steele1 = offs1 2.8448 SELE2 ;

st2101 = steels1 D 1 steele1 ;
st2102 = st2101 PLUS ((1. * space1) 0.0000 0.0000) ;
st2103 = st2101 PLUS ((2. * space1) 0.0000 0.0000) ;
st2104 = st2101 PLUS ((3. * space1) 0.0000 0.0000) ;
st2105 = st2101 PLUS ((4. * space1) 0.0000 0.0000) ;
st2106 = st2101 PLUS ((5. * space1) 0.0000 0.0000) ;
st2107 = st2101 PLUS ((6. * space1) 0.0000 0.0000) ;
st2108 = st2101 PLUS ((7. * space1) 0.0000 0.0000) ;
st2109 = st2101 PLUS ((8. * space1) 0.0000 0.0000) ;
st2110 = st2101 PLUS ((9. * space1) 0.0000 0.0000) ;
st2111 = st2101 PLUS ((10. * space1) 0.0000 0.0000) ;
st2112 = st2101 PLUS ((11. * space1) 0.0000 0.0000) ;

st21 = st2101 ET st2102 ET st2103 ET st2104
    ET st2105 ET st2106 ET st2107 ET st2108
    ET st2109 ET st2110 ET st2111 ET st2112;

* steel bars in Y-direction at higher elevation
steels1 = offs1 0.1016 SELE3 ;
steele1 = offs1 2.8448 SELE3 ;

st2201 = steels1 D 1 steele1 ;
st2202 = st2201 PLUS ((1. * space1) 0.0000 0.0000) ;
```

```
st2203 = st2201 PLUS ((2. * space1) 0.0000 0.0000) ;
st2204 = st2201 PLUS ((3. * space1) 0.0000 0.0000) ;
st2205 = st2201 PLUS ((4. * space1) 0.0000 0.0000) ;
st2206 = st2201 PLUS ((5. * space1) 0.0000 0.0000) ;
st2207 = st2201 PLUS ((6. * space1) 0.0000 0.0000) ;
st2208 = st2201 PLUS ((7. * space1) 0.0000 0.0000) ;
st2209 = st2201 PLUS ((8. * space1) 0.0000 0.0000) ;
st2210 = st2201 PLUS ((9. * space1) 0.0000 0.0000) ;
st2211 = st2201 PLUS ((10. * space1) 0.0000 0.0000) ;
st2212 = st2201 PLUS ((11. * space1) 0.0000 0.0000) ;

st22 = st2201 ET st2202 ET st2203 ET st2204
    ET st2205 ET st2206 ET st2207 ET st2208
    ET st2209 ET st2210 ET st2211 ET st2212;

* Lower elevation steel
stlowe = st11 ET st21;
* Higher elevation steel
sthigh = st12 ET st22;

* All steel
sttotal = st11 ET st12 ET st21 ET st22;

sttotal = sttotal COUL 'ROUG';

************************************************************
* Define points for viewpoint
s1 = frtotal POIN 'PROC' ((-1.*leng1) (-1.*leng1) (0.));
s2 = frtotal POIN 'PROC' ((CL + leng1) (-1.*leng1) (0.));
s3 = frtotal POIN 'PROC' ((CL + leng1) (CW + leng1) (0.));
s4 = frtotal POIN 'PROC' ((-1.*leng1) (CW + leng1) (0.));

* Define points on frame for rigid body motion
F1 = frtotal POIN 'PROC' C1;
F2 = frtotal POIN 'PROC' C2;
F3 = frtotal POIN 'PROC' C3;
```

```
F4 = frtotal POIN 'PROC' C4;

* Define surfaces for sliding
cosyz1 = FAPLAN cototal C1 C4 C5 0.0001;
cosyz2 = FAPLAN cototal C2 C3 C6 0.0001;
cosxz1 = FAPLAN cototal C1 C2 C5 0.0001;
cosxz2 = FAPLAN cototal C3 C4 C7 0.0001;

frsyz1 = FAPLAN frtotal C1 C4 C5 0.0001;
frsyz2 = FAPLAN frtotal C2 C3 C6 0.0001;
frsxz1 = FAPLAN frtotal C1 C2 C5 0.0001;
frsxz2 = FAPLAN frtotal C3 C4 C7 0.0001;

*=============================================================

* Properties and Models

*=============================================================

* (Mechanical) model for concrete
mod1 = MODE (cototal) 'MECANIQUE'
 'ELASTIQUE' 'VISCOPLASTIQUE' 'DEFDIF';

* Mechanical properties for concrete
Ey1 = 34.0e9 ; COMM 'Young modulus' ;
nu1 = 0.14 ; COMM 'Poisson ratio' ;
ft1 = 2.4e6; COMM 'Tensile strength' ;
kt01 = ft1/Ey1;
acom1 = 1.4;
bcom1 = 1500.;
Gf1 = 50.;
cisa1 = 1.;

* Regularisation
cham1='MANU' 'CHML' mod1 'SCAL' 1. 'STRESSES';
cham2='INTG' cham1 mod1 'ELEM' 'SCAL';
```

```
longelm1 = cham2**(1./(VALE DIME)) ;

chamgf1 = cham2 MASQUE SUPERIEUR 0; chamgf2 = Gf1 * chamgf1;
numer1 = (longelm1*ft1 * chamgf1);
denomin1 = (chamgf2 - (longelm1*ft1*ft1/Ey1/2 * chamgf1));
denomin2 = denomin1**(-1);
*** Cas B(Gf)
chmbtra1 = numer1 * denomin2;

* coefficient of thermal expansion
alfa1 = 1.e-5;

* ASR parameters
sl0 = 0.2 ; taul1 = 146.3*24.*3600.; tauc1 = 56.0*24*3600.;
phir1 = 1023.e-6;
EaRasr1 = 5080. ;
tempcon1 = 273.15 + 38. ;
tempref1 = 273.15 + 38. ;
xE1 = 0.657; lambdah1 = 0.104E-2;
Dmaxi1 = 0.707; lambdaa1 = 0.044E-2;
anisx1 = 1.; anisy1 = 1.; anisz1 = 2.1;

* Anisotropy Model Parameters
coefstr1 = PROG (02.60652e6) (-0.84147e6) (-4.11249e6)
 (001.00000) (0.333333);
coefstr2 = PROG (01.20703e6) (01.26326e6) (02.62379e6)
 (001.00000) (0.333333);
coefstr3 = PROG (01.20703e6) (01.26326e6) (02.62379e6)
 (001.00000) (0.333333);

* (Mechanical) model for reinforcement
mod2 = MODE (sttotal) 'MECANIQUE' 'ELASTIQUE' 'PLASTIQUE'
'PARFAIT' 'BARRE';

* Mechanical properties for reinforcement
racier = 0.017905 ;
```

```
sect1 = (3.14159 * racier * racier) ;
mat2 = MATE mod2 'YOUN' 210.e9 'NU' 0.3 'SECT' sect1
'SIGY' 483.e6 'ALPHA' alfa1 'RHO' 7000.0;

* (Mechanical) model for frame
mod3 = MODE (frtotal) 'MECANIQUE' 'ELASTIQUE';

* Mechanical properties for frame
mat3 = MATE mod3 'YOUN' 210.e9 'NU' 0.3
  'ALPHA' alfa1 'RHO' 7000.0;

*=============================================================

* TIME AND LOADING

*=============================================================

* Time discretization
time1 = 1. * 365. * 24. * 3600. ;
time2 = 2. * 365. * 24. * 3600. ;
nb1 = 60 ;
lis1 = PROG 0. PAS (time1/(nb1/2.)) time1
  PAS ((time2-time1)/(nb1/2.)) time2 ;

* Boundary conditions
* Rigid body motion of frame
rig1 = BLOQ 'UX' 'UY' 'UZ' (F1);
rig2 = BLOQ 'UY' 'UZ' (F2);
rig3 = BLOQ 'UZ' (F3);
rig4 = BLOQ 'UX' 'UZ' (F4);
rigf1 = rig1 ET rig2 ET rig3 ET rig4;

* Rigid body motion of concrete
rig5 = BLOQ 'UX' 'UY' 'UZ' (C1);
rig6 = BLOQ 'UY' 'UZ' (C2);
rig7 = BLOQ 'UZ' (C3);
```

```
rig8 = BLOQ 'UX' 'UZ' (C4);
rig9 = RELA (sttotal) 'ACCRO' cototal;
rigc1 = rig5 ET rig6 ET rig7 ET rig8 ET rig9;

* Allow sliding of concrete on frame
rig10 = RELA 1. 'UX' cosyz1 - 'UX' frsyz1 ;
rig11 = RELA 1. 'UX' cosyz2 - 'UX' frsyz2 ;
rig12 = RELA 1. 'UY' cosxz1 - 'UY' frsxz1 ;
rig13 = RELA 1. 'UY' cosxz2 - 'UY' frsxz2 ;
rigs1 = rig10 ET rig11 ET rig12 ET rig13;

rigt1 = rigf1 ET rigc1 ET rigs1;

* Loading by imposing thermal strain - ASR strain
* Initialisation
tab_tps = TABLE; tab_temp = TABLE; tab_aff = TABLE ;
tab_tps.0 = 0. ; tab_temp.0 = MANU 'CHPO' cototal 'T' 0. ;
tab_aff.0 = MANU 'CHPO' cototal 'T' 0.;
sl1 = MANU 'CHPO' cototal 'T' 1. ;
SLmod = TABLE;

*=============================================================

* CALCULATION

*=============================================================

* INITIALISATION
* test1 = MANU CHPO cototal 3 'UX' 1. 'UY' 1. 'UZ' 1.;
* test2 = EPSI test1 mod1;
* defi0 = ( EXP (0.*test2) );
* epsxy1 = 0.*(EXCO defi0 'GAXY');
* epszz1 = 0.*(EXCO defi0 'EPZZ');

test3 = MANU CHPO (sttotal) 3 'UX' 1. 'UY' 1. 'UZ' 1.;
defia1 = EPSI test3 mod2 mat2;
```

```
test4 = MANU CHPO (frtotal) 3 'UX' 1. 'UY' 1. 'UZ' 1.;
defif1 = EPSI test4 mod3 mat3;

tab1 = TABLE;
tab1.MODELE = mod1 ET mod2 ET mod3;
tab1.BLOCAGES_MECANIQUES = rigt1;
tab1.MOVA='DMEC';
*tab1.PRECISION = 1.e4;

n1 = 1 ;
REPETER BOUCLE nb1;

* Definition of the calculation time
temps1 = EXTR lis1 n1; temps2 = EXTR lis1 (n1 + 1) ;
tempc1 = PROG temps2; dt = temps2 - temps1;

* Alteration of concrete temperature based on time
bool1 = temps2 > (time1);
SI bool1;
tempcon1 = 273.15 + 23. ;
FINSI;

* Loading by imposing thermal strain - ASR strain
SLmod.(n1 - 1) = sl1 ; SLmod.n1 = sl1;
tab_tps.n1 = temps2;
aff2 = @ASRSTR0 taul1 tauc1 sl0 EaRasr1 tempcon1 tempref1
 dt tab_aff.(n1 - 1) Slmod.(n1 - 1) Slmod.n1 mod1;
tab_aff.n1 = aff2;

SI (n1 EGA 1) ;

defi1 = @ASRDEF3 phir1 anisx1 anisy1 anisz1
 tab_aff.(n1-1) aff2 mod1;

SINON;
```

```
stress1 = tab1.CONTRAINTES.(n1 - 1) ;
defi1 = @ASRANI3 phir1 anisx1 anisy1 anisz1
 tab_aff.(n1-1) aff2 mod1
 stress1 coefstr1 coefstr2 coefstr3;

FINSI;

tempc2 = PROG temps1 temps2; prog2 = PROG 0. 1.;
evth1 = EVOL 'MANU' 'Temps' tempc2 'DEFI' prog2;
charth1 = CHAR 'DEFI' defi1 evth1;
charth2 = CHAR 'DEFI' defia1 evth1;
charth3 = CHAR 'DEFI' defif1 evth1;



* Modification of mechanical properties
epsasr1 = (1./3.)*(anisx1 + anisy1 + anisz1) * phir1 *
 (tab_aff.(n1 - 1) + tab_aff.n1 );
xrE1 = @RM_PORO xE1 lambdah1 epsasr1 ;
xrE2 = @RM_ASR Dmaxi1 lambdaa1 epsasr1 ;
Ey2 = Ey1 * (CHAN 'COMP' xrE1 'YOUN');
Ey3 = CHAN 'CHAM' Ey2 mod1;
mat1 = MATE mod1 'YOUN' Ey3 'NU ' nu1 'ALPHA' alfa1
 'KTR0' kt01 'BTRA' chmbtra1 'CISA ' cisa1
 'ACOM' acom1 'BCOM' bcom1 'BETA' 0. 'DEXT' 0.;

*
* Step by step calculation
*
tab1.CHARGEMENT = charth1 ET charth2 ET charth3;
tab1.TEMPS_CALCULES = tempc1;
tab1.CARACTERISTIQUES = mat1 ET mat2 ET mat3;

PASAPAS tab1;

n1 = n1 + 1 ;
```

```
FIN BOUCLE;

* Save results
OPTI SAUV 'Result_CASR.sortdgibi';
SAUV;

FIN;
```

Vita

Nolan Wesley Hayes was born in Morristown, Tennessee. He graduated from Jefferson County High School in Dandridge, Tennessee in 2011. He then went on to receive his Bachelor of Science in Civil Engineering from The University of Tennessee, Knoxville in May 2015. He served as a Graduate Research Assistant in the Department of Civil and Environmental Engineering at The University of Tennessee, Knoxville, completing his PhD in December 2019.